STEAM-WATER RELATIVE PERMEABILITY

A DISSERTATION

SUBMITTED TO THE DEPARTMENT OF PETROLEUM ENGINEERING

AND THE COMMITTEE ON GRADUATE STUDIES

OF STANFORD UNIVERSITY

IN PARTIAL FULFILLMENT OF THE REQUIREMENTS

FOR THE DEGREE OF

DOCTOR OF PHILOSOPHY

By

John Raymond Counsil

May 1979

ACKNOWLEDGEMENT

I sincerely appreciate and want to recognize the contributions of many friends, too numerous to be listed below.

Kathy, my wife, provided unceasing support both at home and in the lab. Professor H. J. Ramey, Jr., served as my advisor and, with Professors W. E. Brigham and M. B. Standing, provided many helpful suggestions. The Reading Committee included Emeritus Professor F. G. Miller and Professor H. Cinco-Ley. The Oral Examination Committee included Professor S. S. Marsden, Jr. Dr. Paul Atkinson and Dr. Roland Horne served as Geothermal Project Managers. Jon Grim, machinist, and Paul Pettit, technician, helped develop the experimental apparatus. Dr. H. K. Chen, C. H. Hsieh, Kai Lanz, and Joe Counsil provided the support necessary to make the capacitance probe useful. Elizabeth Luntzel typed the manuscript and the figures were drafted by Terri Ramey. Photographs were taken by Abdurrahman Satman.

This research was carried out under Research Grants GI-34925 and AER-03490-A03, provided by the National Science Foundation, and Research Grant DOE-LBL-167-3500, provided by the Department of Energy (Energy Research and Development Administration) through a subcontract with the Lawrence Berkeley Laboratory.

ABSTRACT

Steam-water relative permeability curves are required for mathematical models of two-phase geothermal reservoirs. In this study, drainage steam-water relative permeabilities were obtained from steady, two-phase, non-isothermal bench scale flow experiments. Liquid water saturations were measured along the length of the synthetic sandstone cores using a capacitance probe.

In addition, nitrogen-water relative permeabilities were obtained for a synthetic sandstone core. These isothermal, unsteady gas-drive experiments were used to determine drainage relative permeabilities and calculated water saturations. Experiments were conducted at several temperatures and pressures. It was established that nitrogen-water relative permeability was not strongly temperature dependent below 300°F at confining pressures less than 300-500 psig.

A comparison of the steam-water and nitrogen-water relative permeability curves indicated that at high water saturations, the external gas drive (nitrogen-water) gas relative permeabilities were larger than the internal gas drive (steam-water) steam relative permeabilities.

TABLE OF CONTENTS

LIST OF FIGURES

LIST OF TABLES

ERRATA (11/81)
Steam-Water Relative Permeability
John R. Counsil
Petroleum Engineering PhD Dissertation
Stanford University (May 1979)

Page	Change
1	1ine 11 from "Toyoni" to "Toronyi"
1	1ine 16 from "curves have" to "has"
77	line 17 from "extrapolation from" to "interpolation between"
77	1ine 18 from "to" to "and"
103	Equation 6-19 Rewrite $\bar{S}_g = 1 - \bar{S}_w = \frac{W_p \bar{v}_{w,\,core}}{V_p \bar{v}_{w,\,room}}$
107	Figure 6-19 title: from "law" to "law)"
113	1ast 1ine rewrite: $X_2(L)$ is: $\bar{S}_g = \frac{\int_1^2 S_g\,dx}{\int_1^2 dx} = \frac{\int_1^2 S_g\,dx}{L - X_{dry}}$
115	Equ. 6-36 Rewrite $\bar{S}_g = \frac{\int_1^2 S_g\,df'_g}{fg'_2 - fg'_1}$
115	Equ. 6-37 rewrite denominator from "fg'_2 " to "$fg'_2 - fg'_1$"
115	Equ. 6-39 from "$S_{g_2} - [$" to "$S_{g_2} + [$"
115	Equ. 6-41 from "$\left[S_{g_2} - [\right.$" to "$\left[S_{g_2} + [\right.$"
119	Equ. 6-50 from "q" to "q_t"
120	1ast 1ine from "fw" to "fw_2"

121 Equ. 6-60 from "(6-60)" to "(6-60a)"
below Equ. 6-60 write

$$\text{"krg} = \frac{(1-fw_2)\mu_g}{\text{intercept}} \left[\frac{L - X_{dry}}{L}\right] \qquad (6\text{-}60b)$$

125 Fig. 6-22 from "Drainage," to "Drainage"

136 line 13 from "lower" to "higher"

140 1ine 4 from "methods" to "method"

142 line 12 from "k = effective permeability to liquid" to "k_s = effective permeability to steam" and "k_w = effective permeability to 1iquid water"

142 below "k_{rl}" write

"k_{rs} = steam relative permeabi 1ity"

1. INTRODUCTION

Relative permeability curves are important because they are used to obtain effective permeabilities, which are used in rate equations, such as Darcy's law. Rate equations are used in mathematical models to calculate the rate of mass and energy recovery from geothermal reservoirs. Thus relative permeability curves are a key part of forecasting project energy recovery and project economics.

The need for and use of relative permeability curves in petroleum reservoir simulation computer models have been described by Crichlow (1977), Staggs et al. (1971), and many others.

Steam-water relative permeability curves were used in reservoir simulation or characterization by Donaldson (1967), Toyoni (1974), Atkinson (1975), Faust and Mercer (1975), Garg et al. (1975), Martin (1975), Mercer and Faust (1975), Moench (1976), Brownell et al. (1977), Herkelrath (1977), and Thomas and Pierson (1978).

The important point is that although steam-water relative permeability curves have never been studied in the laboratory in detail, estimated relative permeabilities have been used a great deal in reservoir simulation.

The purpose of this research is to establish a set of valid steam-water relative permeability curves for a drainage process. Distinctive characteristics of these curves should then be incorporated into the relative permeability curves used for matching or forecasting geothermal reservoir performance.

2. LITERATURE SURVEY

In order to characterize the nature of the problem and the state-of-the-art, a brief discussion of the following subjects is required: **(1)** definition of relative permeability, (2) relative permeability curves currently used for drainage steam-water flow, **(3)** experimental techniques traditionally used to obtain gas-liquid relative permeability, *(4)* heat transfer considerations in nonisothermal bench scale experiments, and (5) the effect of frequency on the capacitance of water-saturated porous media,

2.1 Definition of Steam-Liquid Water Relative Permeability

Amyx, Bass and Whiting (1960), Frick (1962), Craig (1971), Standing (1975), and others have described relative permeability in the traditional petroleum engineering sense for immiscible multiphase fluid flow. Relative permeability is the effective permeability normalized to a specific base permeability, such as the absolute permeability, Effective permeability is a measure of the conductivity of a rock to a fluid in the presence of at least one other fluid, and depends on:

a. pore size

b. pore size distribution

c. wettability

d. fluid saturation

e. fluid saturation history (drainage-decreasing wetting phase saturation, imbibition-increasing wetting phase saturation)

Effective permeabilities are used in flow rate equations, such as Darcy's law for linear horizontal flow:

$$w_g = - \frac{k_g A}{(\mu \bar{v})_g} \frac{dp}{dx} \qquad (2\text{-}1)$$

$$w_\ell = - \frac{k_\ell A}{(\mu \bar{v})_\ell} \frac{dp}{dx} \qquad (2\text{-}2)$$

where:

w = weight rate of flow

A = cross-sectional area perpendicular to flow

$\bar{v}$ = fluid specific volume

μ = fluid viscosity

dp/dx = pressure gradient in flowing fluid

k = effective permeability

g = gas

ℓ = liquid

The gas effective permeability is equal to k_{rg}, the gas relative permeability, multiplied by the appropriate base permeability, which may be the absolute permeability K. Likewise, $k_\ell = k_{r\ell} \cdot K$. The fluid used to measure absolute permeability must be stated. Relative permeabilities are often presented in graphical form as functions of fluid saturation.

To understand steam-liquid water flow through porous media, the important physical processes must be understood. Kruger and Ramey (1973) and Trimble and Menzie (1975) have discussed some of the important points. Other facets of two-phase flow, such as liquid holdup, are brought out in principle by Gould's (1974) discussion of steam-water flow in geothermal

wellbores, Miller's (1951) discussion of nonisothermal, two-phase boiling propane flow through a sandpack, and in the Culham et al. (1969) study of two-phase hydrocarbon flow.

Steam-liquid water flow may differ from oil-gas or oil-water flow due to the thermodynamic and interfacial characteristics of water-rock systems. Furthermore, interphase mass transfer occurs between steam and liquid water resulting in both changing quality and saturation along the flow path.

For immiscible fluids, it has been observed that only one fluid flows through a given pore at a time. For steam-water flow, it is not clear whether dry steam flows through some pores and liquid water through others, or whether a locally homogeneous wet steam flows at differing liquid and vapor velocities. It is not clear that fluid interference is similar for steam-water flow and for immiscible gas-oil, or water-oil flow. The next section presents the steam-water relative permeability curves currently available.

2.2 Steam-Liquid Water Relative Permeability Curves Currently Available

In the following sections we will consider available experimental relative permeability data, data extracted from field performance, and some miscellaneous sources of information.

2.2.1 Experimental Relative Permeability Curves

Arihara (1974) developed the steam-water relative permeability curve shown in Fig. 2-1 using equations developed by Miller (1951) for steady, single-component, two-phase, nonisothermal adiabatic flow:

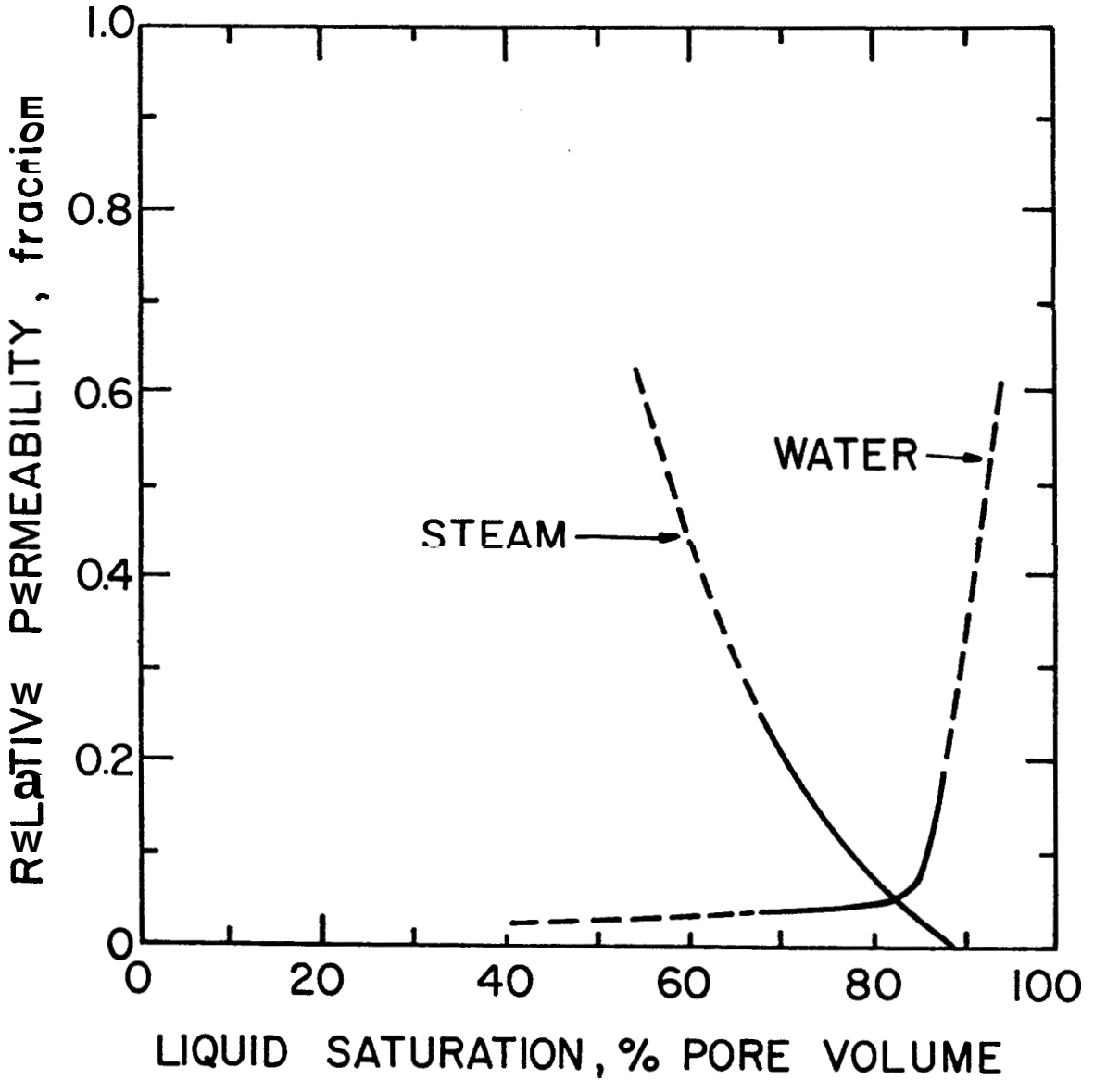

FIG. 2-1: WATER-STEAM RELATIVE PERMEABILITY FOR RUN NO. 4, SYNTHETIC SANDSTONE (ARIHARA, 1974)

$$\frac{k_\ell}{k_g} = \frac{(\mu\bar{v})_\ell}{(\mu\bar{v})_g} \frac{1-f}{f} \tag{2-3}$$

$$k_{rg} = \frac{k_g}{K} = \frac{fw(\mu\bar{v})_g}{A\left(-\frac{dp}{dx}\right)} \tag{2-4}$$

$$k_{r\ell} = \frac{k_\ell}{K} = \frac{(1-f)w\ (\mu\bar{v})_\ell}{A\left(-\frac{dp}{dx}\right)} \tag{2-5}$$

where:

$$f = \frac{h-h_\ell}{h_g-h_\ell} = \frac{w_g}{w} \tag{2-6}$$

h = enthalpy of inlet fluid
w = total mass flow rate $(w_\ell+w_g)$

Arihara measured the temperature profile through the boiling region in his synthetic sandstone core to obtain the fluid properties, enthalpy, and pressure at each point in the two-phase region. Thermal equilibrium and no vapor pressure lowering effects were assumed. Although vapor pressure lowering has been studied by Calhoun, Lewis, and Neuman (1949) and Chicoine, Strobel, and Ramey (1977), no quantitative understanding exists yet. It does appear that vapor pressure lowering may be significant in consolidated sandstones at low water saturation. Work in this area is continuing by Hsieh and Ramey (1978) and Moench and Herkelrath (1978).

With regard to local thermal equilibrium, Atkinson (1977) has discussed the assumption of uniform, local rock-fluid temperature, and Miller (1951) and Culham et al. (1969) have discussed local phase equilibrium.

The relative permeabilities and their ratio areeasily calculated using the above equations. Since Arihara was not able to measure saturation,

he used his calculated relative permeability ratio and Weinbrandt's (1972) water-oil permeability ratio vs water saturation curve to obtain a water saturation for each steam or water relative permeability. The obvious drawback here is that the oil-water permeability ratio curve may not be appropriate for the steam-water system.

Trimble and Menzies (1975) developed the curves shown in Fig. 2-2 for Boise and Berea sandstone cores. It was not stated, but Trimble and Menzies assumed the liquid water and steam velocities were equal when they determined their water saturations from calculated steam quality. It is generally expected that gas flows at a higher velocity than liquid in two-phase flow. Miller (1951) discussed this point in detail. To summarize, the quality, or gas mass fraction, $\bar{f}$, in an element Δx at an instant in time is:

$$\bar{f} = \frac{1}{1 + \left(\frac{S_w}{1-S_w}\right)\frac{\bar{v}_g}{\bar{v}_\ell}} \qquad (2\text{-}7)$$

where S_w = liquid water saturation, fraction pore volume.

In contrast, the quality $f = w_g/w$ of the two-phase fluid passing a point x in unit time is:

$$f = \frac{1}{1 + \left(\frac{S_w}{1-S_w}\right)\left(\frac{\bar{v}_g}{\bar{v}_\ell}\right)\left(\frac{u_\ell}{u_g}\right)} \qquad (2\text{-}8)$$

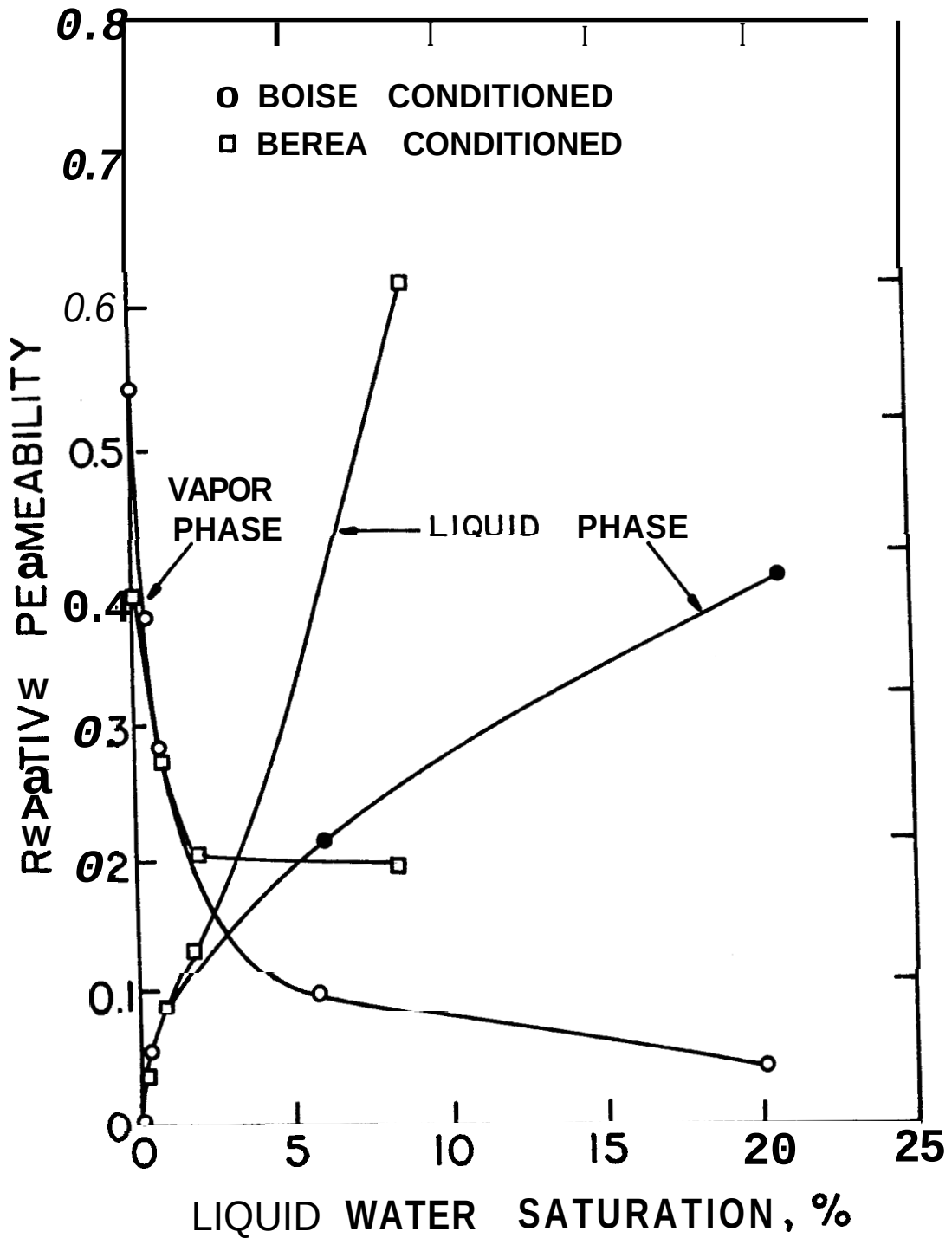

FIG. 2-2: COMPARISON OF STEAM VAPOR AND LIQUID RELATIVE PERMEABILITIES FOR BOISE AND BEREA SANDSTONE (TRIMBLE AND MENZIES, 1975)

Equations 2-7 and 2-8 indicate that $f = \overline{f}$ only when the gas microscopic velocity u_g is equal to the liquid velocity u_ℓ. Trimble and Menzies incorrectly used f in place of $\overline{f}$ in Eqs. 2-4 and 2-5.

Chen (1976) presented the drainage relative permeability curves shown in Fig. 2-3 for a synthetic sandstone. Chen used the same equations as Miller and Arihara, except that he obtained water saturation directly using a capacitance probe. Chen extrapolated limited relative permeability data using Corey-type equations (X_c=2):

$$k_{r\ell} = (S_W^*)^4 \tag{2-9}$$

$$k_{rg} = (1-S_w^*)^2\,[1-(S_w^*)^2] \tag{2-10}$$

where:

$$S_w^* = \frac{S_w - S_{wi}}{1-S_{wi}} \tag{2-11}$$

S_w = volumetric liquid water saturation

S_{wi} = irreducible water saturation

The critical gas saturation S_{gc} was assumed to be zero.

Chen calculated the irreducible water saturation, S_{wi}, for several $k_{r\ell}(S_w)$ values and noted that S_{wi} increased with increasing water saturation and temperature. This led Chen to extrapolate his data as a function of temperature.

Poston et al. (1970), Weinbrandt et al. (1975), Casse and Ramey (1976), and Aruna (1976) have demonstrated either increased irreducible water saturation or decreased permeability to water in sandstones with increasing temperature. Sinnokrot et al. (1971) also concluded that sandstones

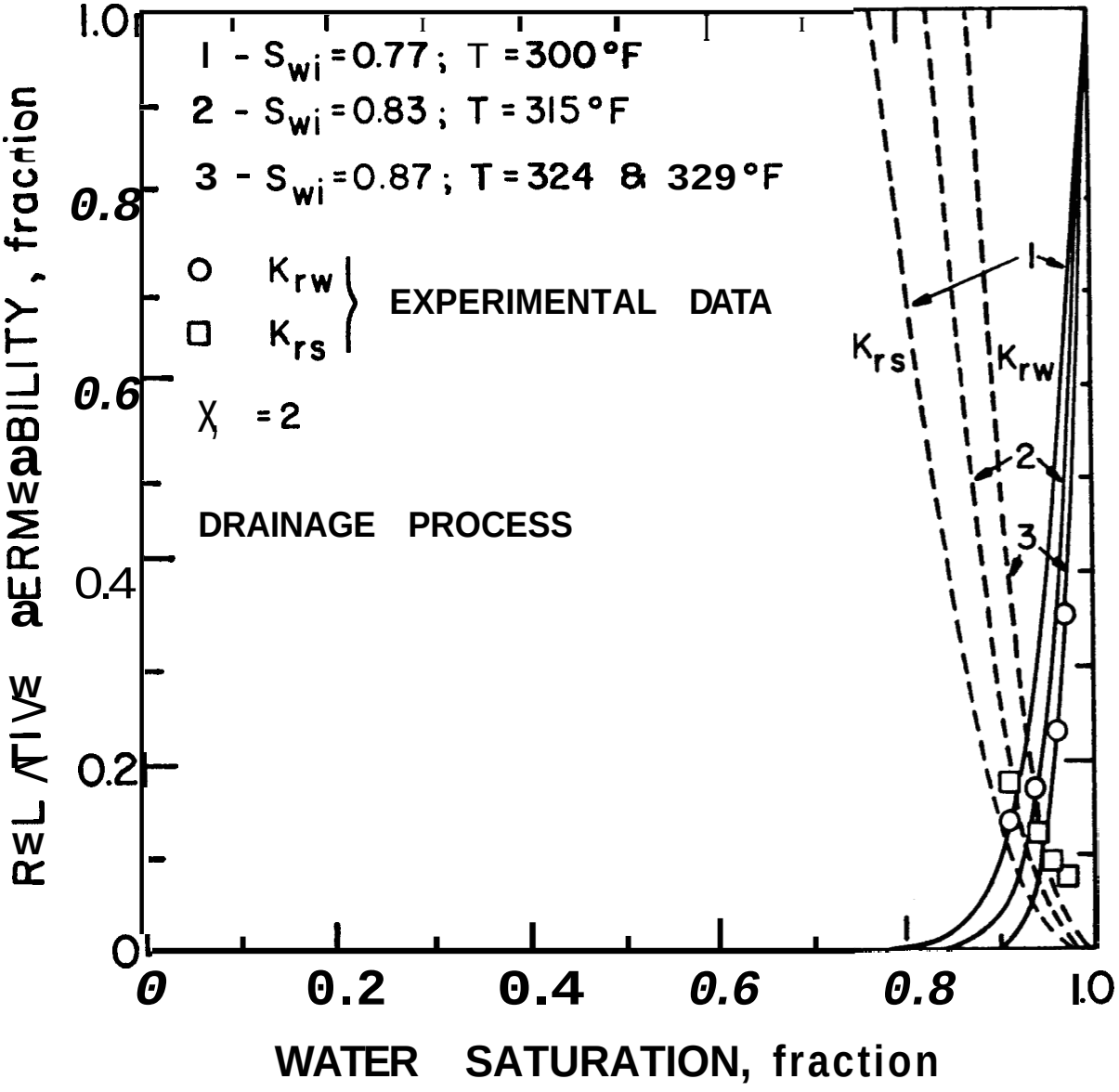

FIG. **2-3: RELATIVE PERMEABILITY TO STEAM AND WATER VS WATER SATURATION FOR A SYNTHETIC CONSOLIDATED SANDSTONE CORE (CHEN, 1976)**

become more water wet at high temperatures. Arihara *(1974)* and Casse and Ramey *(1976)* concluded that significant (more than 5%) temperature effects were observed at confining pressures greater than *450* psi. Chen did not report his confining pressure, although it is known to be less than *400* psi,

The effect of slippage on steam-water relative permeability curves has not been discussed before, to the author's knowledge. The effect of gas slippage on gas-liquid relative permeability measurements has been studied by Estes and Fulton (1956), Fulton *(1951)*, and Rose *(1948).* It was demonstrated experimentally that the effect of gas slippage on the measured effective gas permeability decreased with an increase in liquid saturation. Rose also showed that no slip correction is required for the gas relative permeability if the same mean pressure is used to determine the gas effective permeability and the gas absolute permeability. Estes and Fulton showed that the slip correction:

$$C = \frac{k_g - k_\ell}{k_g} \times 100 \qquad (2\text{-}12)$$

where:

k_g = gas permeability at mean pressure, p_m

k_ℓ = liquid or slip corrected permeability

was roughly constant at all oil saturations studied ($0 < s_o < 0.70$). Fulton also observed that k_ℓ and bk_ℓ (where b is the Klinkenberg constant) decreased with increasing oil saturation.

For the case of steam-water relative permeabilities, slip could be reduced by running experiments at very high pressures, and therefore very high temperatures. The use of high temperatures poses a severe materials selection problem for the experimental apparatus.

The next section presents relative permeability curves obtained from geothermal field data.

2.2.2 Field Data Relative Permeability Curves

Grant (1977) presented "permeability reduction factors" obtained using production data from the fissured Wairakei Field, New Zealand. Grant was not able to obtain liquid saturations, and presented his results as steam relative permeability versus water relative permeability, as shown in the cross-hatched region in Fig. 2-4.

Grant assumed that the driving pressure gradient and temperature did not change with producing enthalpy change. He developed the following two equations with two unknowns:

$$\frac{w'}{w_o} = k_{r\ell} + k_{rg} \frac{(\mu\bar{v})_\ell}{(\mu\bar{v})_g} \qquad (2-13)$$

$$h\left[\frac{k_{r\ell}}{(\mu\bar{v})_\ell} + \frac{k_{rg}}{(\mu\bar{v})_g}\right] = \frac{k_{r\ell}h_\ell}{(\mu\bar{v})_\ell} + \frac{k_{rg}h_g}{(\mu\bar{v})_g} \qquad (2-14)$$

where w_o is the 100% liquid water flow rate taken from a graph of log wellbore discharge rate versus discharge enthalpy. Individual wellbore graphs were shifted to obtain the best common match. Grant describes his method as being crude and having a large uncertainty. However, he did feel that steam-water flow in a fissured medium differed from that in a sandstone porous medium. It appears that the two phases do not interfere with each other in a fissured rock as they do in a sandstone-type porous rock. Grant used the Wyckoff and Botset (Scheidegger, 1957) water-gas curves to draw his comparison.

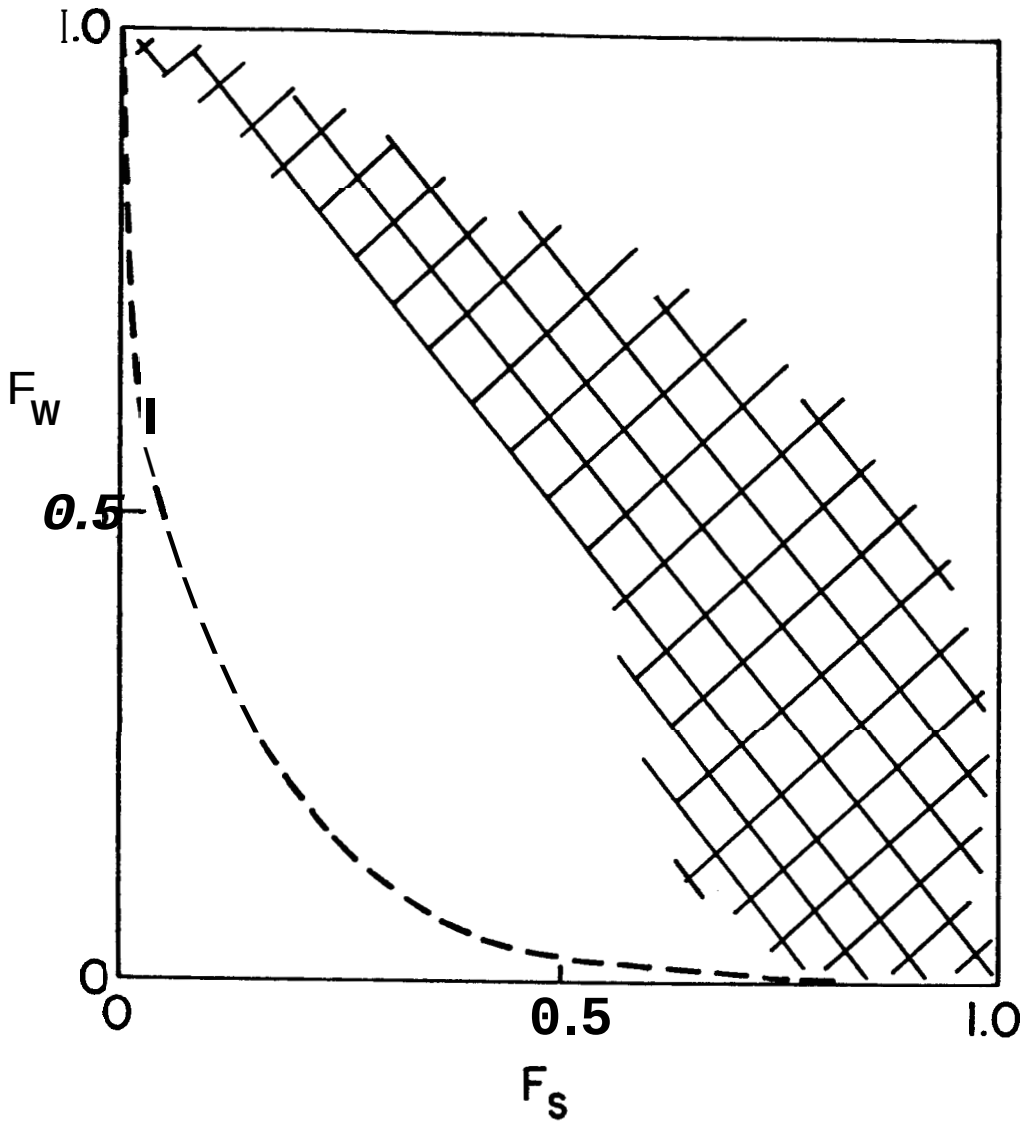

FIG, 2-4: F_w AGAINST F_s FROM WYCKOFF AND BOTSET, AND FROM GRANT (1977)

Horne (1978) extended the work of Grant by **(1)** considering wellhead pressure change with time for each well, and (2) using downhole temperatures and fluid properties. Horne graphed his relative permeabilities versus a "flowing" water saturation that did not consider the immobile fluid in the reservoir. Horne expected a low immobile liquid saturation in the Wairakei data because flow was through fissures. The resulting curves are shown in Fig. 2-5.

Horne's curves are not relative permeability curves in the traditional sense. The flowing water saturations are actually flowing liquid mass fractions, and not resident volumetric "water saturations." As discussed in Section 2.2.1 in regard to Trimble and Menzies' (1975) experimental data, flowing mass fractions or flowing volumetric fractions are usually not equal to water saturation because the gas and liquid microscopic velocities are unequal and unknown.

Shinohara (1978) further refined the methods of Grant (1977) and Horne (1978), and an example of his results is shown in Fig. 2-6. It is felt that the work of Grant, Horne, and Shinohara is not yet directly useful in the traditional sense because the relative permeabilities are not graphed as a function of conventional water saturation, S_w. However, these results do constitute an interesting method of comparison of relative permeability data. This work is continuing.

The next section presents other forms of relative permeability curves, including the Corey-type equations.

2.2.3 Other Relative Permeability Curves

This section presents the Wyckoff-Botset curve and Corey-type equations.

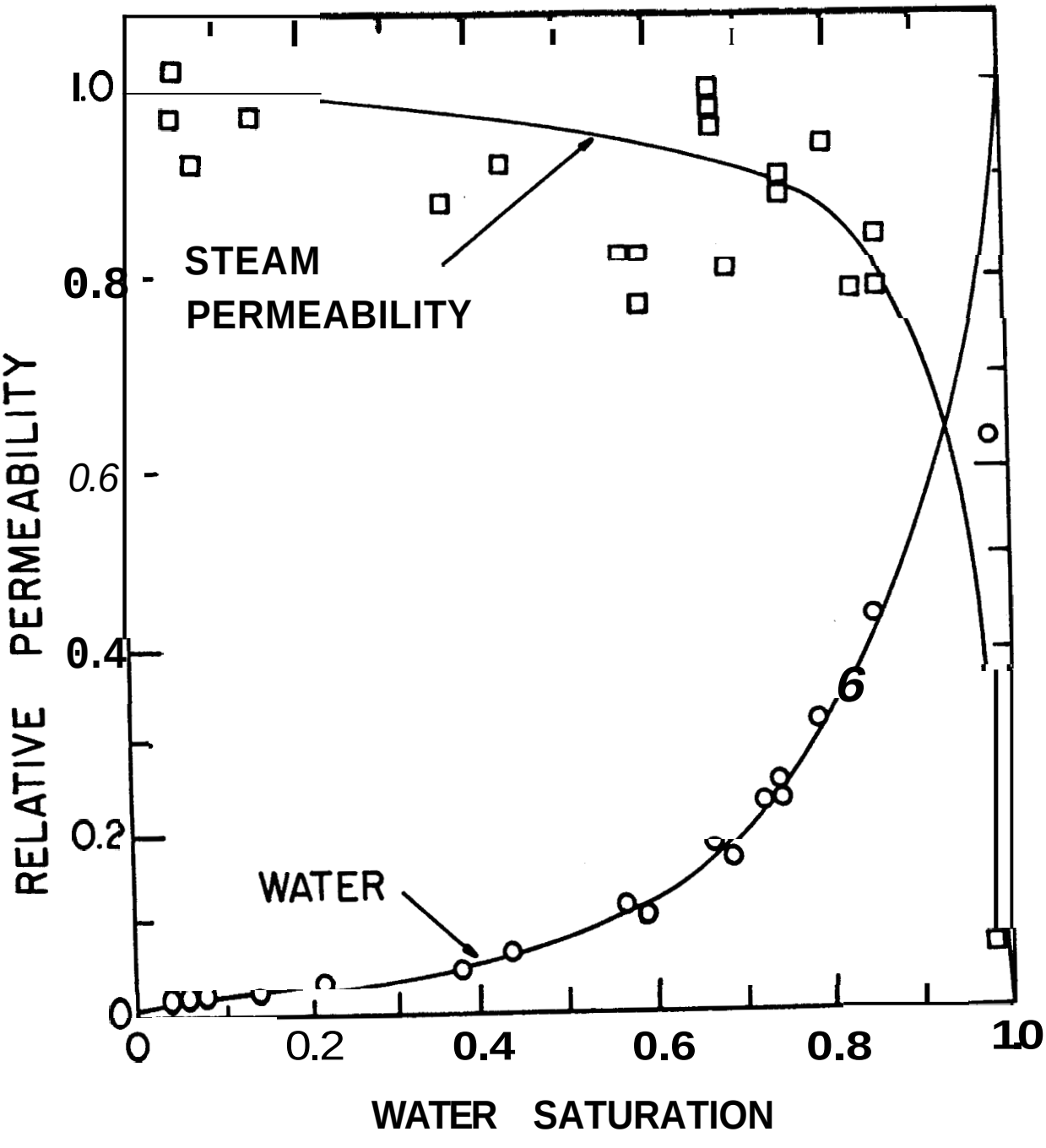

FIG. 2-5: STEAM-WATER RELATIVE PERMEABILITIES FROM WAIRAKEI WELL DATA (HORNE, 1978)

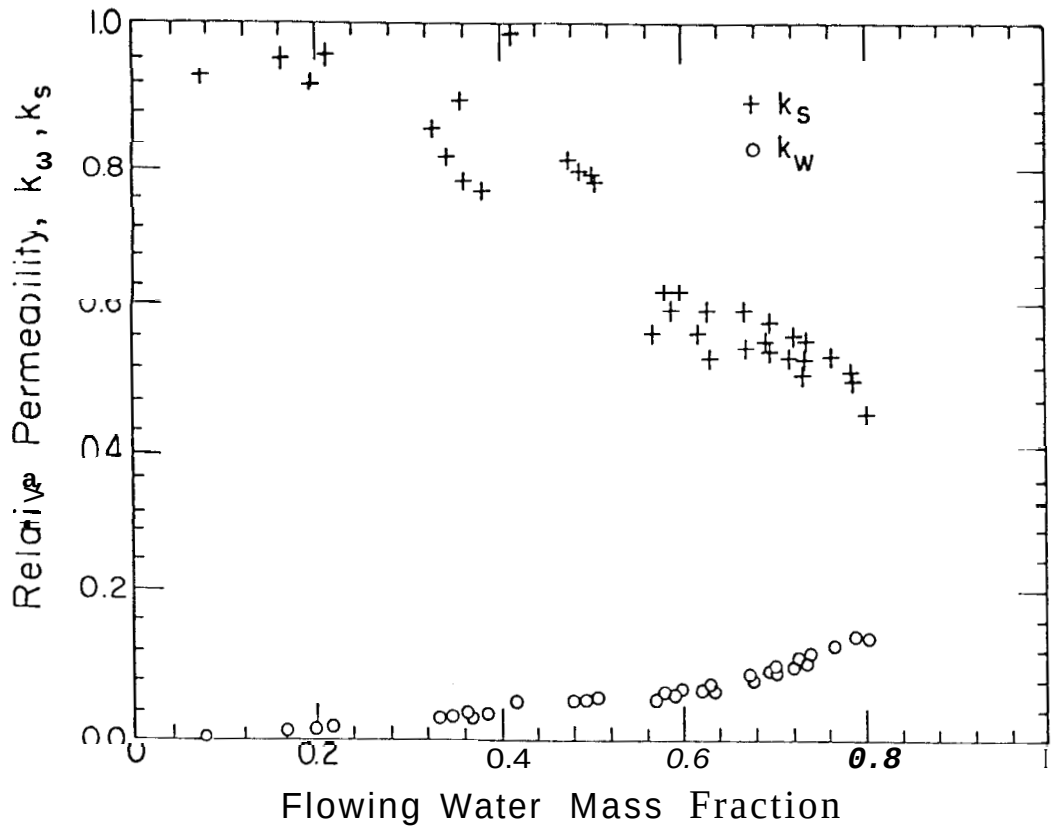

FIG. 2-6: RELATIVE PERMEABILITY VS FLOWING MASS FRACTION FROM WAIRAKEI WELL DATA (SHINOHARA, 1978)

Donaldson (1967) and, it appears, Martin (1975) used the Wyckoff and Botset (Scheidegger, 1974) CO_2 gas-water curve shown in Fig. 2-7 to represent two-phase flow in geothermal reservoirs.

Toyone (1974), Atkinson (1975), Faust and Mercer (1975), Garg et al. (1975), Mercer and Faust (1975), Moench (1976), Brownell et al. (1977), Herkelrath (1977), and Thomas and Pierson (1978) used variations of Corey's (1954, 1977) equations to characterize steam-water relative permeability. Corey used a pore size distribution index of $\lambda_c = 2$ in his two-phase drainage relative permeability equations. A value of $\lambda_c = 2$ represents a wide range of pore sizes.

Atkinson (1975) adapted the Corey equations for a drainage process from Corey, Rathjens, Henderson, and Wyllie (1956) as:

$$k_g = K[1-(S_\ell^*)2]\ [1-S_\ell^*]^2 \tag{2-15}$$

$$k_\ell = K[S_\ell^*]4 \tag{2-16}$$

where:

$$S_\ell^* = \frac{S_\ell - S_{Rr}}{1-S_{gc}-S_{\ell r}} \tag{2-17}$$

$S_{\ell r}$ = residual liquid saturation, a linear function of temperature

S_{gc} = critical gas saturation, a linear function of temperature

K = absolute permeability, a linear function of temperature

Actually, the temperature-independent equations reduce to the Corey equations only for the case of $S_{\ell r} = 0$ and $S_{gc} = 0$. The proper expressions for the Corey equations are presented clearly by Corey (1954) and less clearly by Corey et al. (1956):

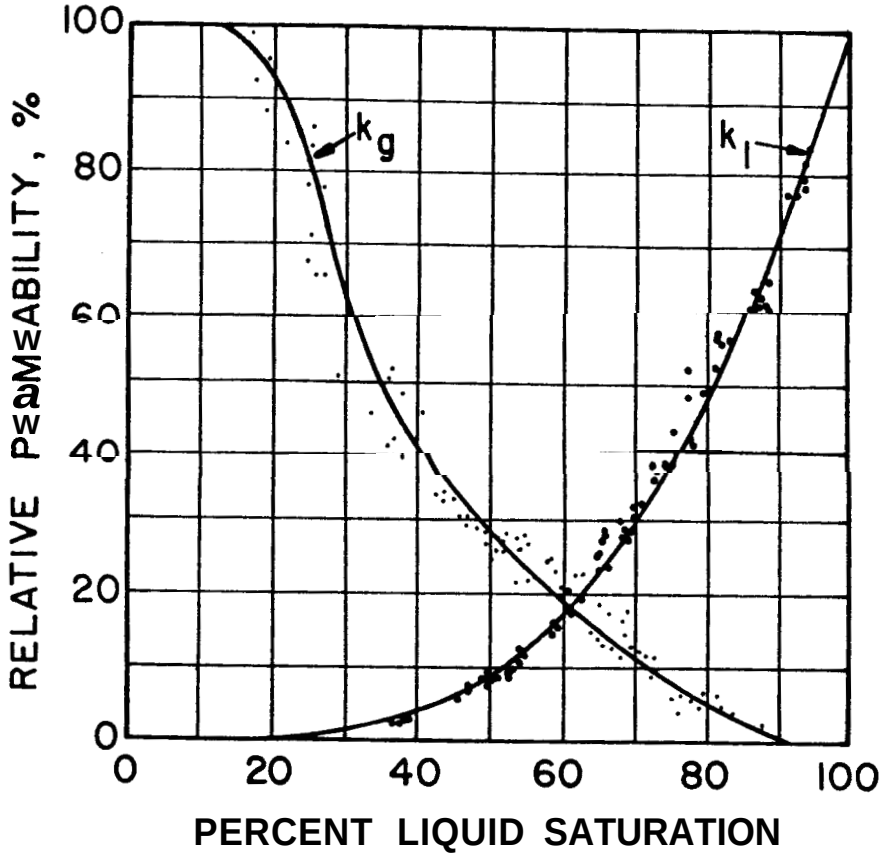

FIG. 2-7: A TYPICAL EXAMPLE OF RELATIVE PERMEABILITY CURVES REFERRING TO A LIQUID (k_l) AND A GAS (k_g) (AFTER WYCKOFF AND BOTSET, 1936; SCHEIDEGGER, 1974)

$$R_g = \frac{k_g}{K} \cdot \frac{K}{k_{g@S_{\ell r}}} = \left[1 - \left(\frac{S_\ell - S_{\ell r}}{1 - S_{gc} - S_{\ell r}}\right)\right]^2 \left[1 - \left(\frac{S_\ell - S_{\ell r}}{1 - S_{\ell r}}\right)^2\right]$$

$$\text{when } (1 - S_{gc}) > S_\ell > S_{Rr} \qquad \textbf{(2-18)}$$

$$R_\ell = k_{r\ell} = \frac{k_\ell}{K} = \left[\frac{S_\ell - S_{\ell r}}{1 - S_{\ell r}}\right]^4$$

$$\text{when } 1 > S_\ell > S_{\ell r} \qquad \textbf{(2-19)}$$

The relative permeability curves are normalized to give $R_g = 1$ when $S_\ell = S_{\ell r}$. $R_g = 0$ when $S_g = S_{gc}$, $R_\ell = 1$ when $S_\ell = 1$, and $R_\ell = 0$ when $S_\ell = S_{\ell r}$. For the oil, water, and/or gas systems that Corey studied, it was also understood that $R_g = 0$ when $S_{gc} > S_g > 0$, $R_\ell = 0$ when $S_{\ell r} > S_\ell > 0$, and that $R_g = k_{rg} = k_g/K$ only when $S_{\ell r} = 0$ or $K = k_{g@S\ell r}$.

Corey (1956), Johnson (1968), and Standing (1975) discuss techniques of estimating S_{Rr} and S_{gc} from gas-oil relative permeability data. Standing (1975) also presented a general relationship for $\frac{k_{g@S_{\ell r}}}{K}$:

$$\frac{k_{g@S_{\ell r}}}{K} = 1.08 - 1.11\, S_{\ell r} - 0.73(S_{\ell r})^2$$

$$\text{when } 0.2 < S_{Rr} < 0.5 \qquad \textbf{(2-20)}$$

Geothermal systems are somewhat different from oil/gas/water systems in that residual (nonflowing) liquid water may vaporize and flow as steam (Kruger and Ramey, 1974). Thus, R_g would increase over the unit R_g @ $S_{\ell r}$ value as the liquid saturation decreased below the S_{Rr} value. Corey's equations also assume that the fluids do not interact with the rock. This

may not be a good assumption for hydrothermal systems with/without dissolved salts. Since no measured steam-water relative permeability curves have been presented in the literature to date, it cannot be demonstrated that Corey's equations do or do not properly characterize steam-water flow.

Garg, Pritchett, and Brownell (1975) treated modified Corey equations (Corey, 1956) in a way similar to Atkinson (1975). However, Garg et al. also assumed $R_g = 1$ when $S_\ell < S_{\ell r}$ and $R_\ell = 1$ when $S_\ell > (1-S_{cg})$.

Although the above formulation may accurately describe some gas relative permeability curves, it would be expected that R_g would increase beyond unity as the liquid vaporizes and interferes less with the total gas flow. Using the same logic, R_ℓ should increase as the gas saturation decreases from S_{cg} to zero. According to the proper Corey equations, R_ℓ should be unity when $S_g = 0$, not when $S_g = S_{gc}$.

Faust and Mercer (1975) and Toyoni (1974) used modified Corey equations that were in agreement with Corey (1954) when $S_{\ell r} = S_{gc}$ (= 0.05), and $k_{rg} @ S_{\ell r} = K$.

Moench (1976) studied steam transport in vapor-dominated systems using:

$$k_{rg} = (1-S_\ell)^2 (1-S_\ell^2) \qquad (2\text{-}21)$$

This expression agrees with Corey's equation when $S_{gc} = S_{\ell r} = 0$.

Herkelrath (1977) treated steam-water flow in a hypothetical fractured material using:

$$k_{r\ell} = (S_\ell)^3 \qquad (2\text{-}22)$$

$$k_{rg} = 1-S_\ell \qquad (2\text{-}23)$$

This is the same as the Corey-type equations with $\lambda_c = \infty$ and $S_{gc} = S_{\ell r} = 0$. From Standing (1975) and Frick (1962), a value of $\lambda_c = \infty$ represents an unconsolidated sand or a uniform pore size in a drainage process. Herkelrath's study dealt with the "heat-pipe" effect in a vapor-dominated system; that is, very high heat transport caused by convection of condensible vapors.

Thomas and Pierson (1978) used:

$$k_{rw} = \left[\frac{S_\ell - S_{\ell r} - S_{gc}}{1 - S_{Rr} - S_{gc}}\right]^4 \tag{2-24}$$

$$k_{rg} = \left[1 - \frac{S_\ell - S_{\ell r} - S_{gc}}{1 - S_{\ell r} - S_{gc}}\right]^2 \left[1 - \left(\frac{S_\ell - S_{\ell r} - S_{gc}}{1 - S_{\ell r} - S_{gc}}\right)^2\right]$$

$$S_{\ell r} = 0.3;\ S_{gc} = 0.05 \tag{2-25}$$

These equations reduce to the proper Corey equations when $S_{gc} = 0$ and $k_g @ S_{\ell r} = K$. Notice that for $S_\ell = S_{\ell r} = 0.3$ and $S_{gc} = 0.05$, $k_{rg} = 1.15$. It is not clear why this formulation for relative permeability was used.

Relative permeability curves used in oil thermal recovery simulators usually consider oil, water, and steam plus gas, and therefore are not directly applicable to a geothermal system. For the case of zero oil saturation, Crookston, Culham, and Chen (1977) use:

$$k_{rg} = S_g 3[2 - S_g] \tag{2-26}$$

$$k_{rw} = \left[\frac{S_w - S_{wr}}{1 - S_{wr}}\right]^4 ;\ S_w > S_{wc} \tag{2-27}$$

$$k_{rw} = 0 ;\ S_w \leq S_{wc} \tag{2-28}$$

These equations reduce to Corey's equations when $S_{wr} = s_{gc} = 0$ and $k_g @ S_{wc} = K$. The dominant process modeled here would be steam condensation, which is an imbibition process. Corey's equations are for drainage processes.

The next section presents the experimental techniques used to obtain gas-liquid relative permeability.

2.3 Experimental Techniques Used to Obtain Gas-Liquid Relative Permeability

In the following sections we will briefly discuss experimental methods of determining relative permeability. The gas-drive method will be covered in detail.

2.3.1 Methods of Experimentally Determining Relative Permeability

Osoba, Richardson, Kerver, Hafford, and Blair (1951) described and evaluated five methods of measuring relative permeability in the laboratory. The five methods were: **(1)** Penn State, (2) single core dynamic, **(3)** gas drive, *(4)* stationary liquid, and (5) Hassler.

For determining gas-liquid relative permeabilities, the gas drive technique is often used because it is rapid and reliable.

2.3.2 Methods of Calculating Relative Permeability from Gas or Liquid Drive Displacement Data

Welge (1952) was the first to modify the Buckley-Leverett theory and present the equations required to calculate (relative) permeability ratios from linear displacement data. Johnson, Bossler, and Naumann (1959) later extended this theory to allow the calculation of individual relative permeabilities. The base permeability was the pre-drive effective

permeability at the initial wetting phase saturation. Jones and Roszelle (1976) then presented a simplified graphical technique that yielded individual relative permeabilities with the absolute (brine) permeability as a base.

The next section presents some of the factors that influence gas-drive relative permeability measurements.

2.3.3 Factors Affecting Gas-Drive Relative Permeability Measurements

Osoba et **al.** (1951) described several techniques of reducing capillary end effects. One method was to use high rates of flow without exceeding the darcy flow limitation. If end effects were not reduced, the calculated wetting phase effective permeability was too low. Hysteresis effects caused by drainage-imbibition were also discussed.

Geffen, Owens, Parrish, and Morse (1951) described reduction of end effects by increasing the pressure gradient across the core. The expansion of gas along the length of the core increases the gas saturation while the capillary end effect increases the liquid saturation. This gas expansion effect can be reduced by using pressure drops small compared to a high average pressure.

Welge (1952) stated that gas (at nearly constant pressure) displacing liquid may be considered an immiscible displacement if the concentration of the gas in the liquid **is** constant. If the pressure is nearly constant with respect to space and time, changes in gas density and solubility are negligible.

With regard to scaling, Rapoport and Leas (1953) found that for an oil-water system defined by its viscosity ratio, interfacial tension, and contact angle, a critical scaling factor LVu_w (core length, injected fluid

velocity, injected fluid viscosity) can be evaluated. Linear floods performed at scaling factors larger than the critical value yield identical recovery vs injection curves and were independent of rate, length, and capillary end effects. However, recovery did vary with viscosity ratio changes. Values of the scaling coefficient required to reach stabilized flow appeared to increase with permeability. For the materials tested, the critical scaling coefficient was between 0.5 and 3.5 (cp-cm2)/min. In addition, Rapoport demonstrated that most practical field operations were operated under stabilized conditions.

It has been suggested that the relative permeability curve for a solution gas drive case may differ from that for an external gas drive due to the different saturation distributions that exist at a given average fluid saturation. However, Stewart, Craig, and Morse (1953) found that permeability ratios (Welge's method) determined for solution gas drive and external gas drive were: **(1)** identical for sandstones, and (2) similar for limestones with intergranular sandstone-type porosity. Stewart et al. also found that for 6-11 in length intergranular limestone cores of 2-300 md, a pressure differential of 20 psi was sufficient to reduce capillary end effects.

Owens, Parrish, and Lamoreaux (1956), in a paper written before Johnson et al. (1959), evaluated the gas drive method for determining (relative) permeability ratios. They showed that gas drive and steady-state gas-oil relative permeability tests were in good agreement on homogeneous samples. A wide variation resulted for non-uniform samples. It was also concluded that the magnitude of pressure differential required to minimize end effects varied inversely with the core permeability. The length of the "stabilized zone" was inversely related to injection rate.

Therefore, to reduce the effects of the "stabilized zone" and "end effects," it was determined that "the pressure differential should be of such magnitude that a volume of gas approximately equal to one-half the pore volume of the test sample should be produced at the downstream pressure conditions in a time interval of 60 seconds." Owens et al. (1956) also concluded that, contrary to common belief, gas expansion did not influence gas drive data using Welge's method. Thus, high static pressures were not required.

Corey and Rathjens (1956) studied the effect of stratification on relative permeability measurements made on laboratory cores. When flow was parallel to the bedding planes, the critical gas saturation was low (close to zero) and S_m values often exceeded unity. S_m was the extrapolated end-point saturation when $k_{rg} = 0$. When flow was perpendicular to the stratification, critical gas saturation was high, the oil relative permeability curve was steep at high oil saturations, and S_m values were often less than unity. Oil relative permeabilities were often less sensitive to slight stratification than were gas relative permeabilities.

Kyte and Rapoport (1958) determined that stabilized water flooding conditions for water-wet cores could be obtained by maintaining a total pressure drop of 50 psi or greater, regardless of core length. They used cores up to 32.80 cm in length.

Davidson (1969) studied the effect of temperature on the permeability ratio of oil-water and gas-oil systems. Davidson concluded that nitrogen-oil permeability ratios appeared to increase with temperature due to molecular slippage (Klinkenberg effect), and possibly due to changes in interfacial properties. Davidson also concluded that neither: (1) gas-in-oil solubility changes with temperature and pressure, nor (2) changes from Darcy to non-Darcy flow were important for his experiments. He did not evaluate oil vaporization effects.

Jones and Roszelle *(1976)* concluded that a graph of $(\Delta p/q)$ vs volume injected must be a straight line unless either: **(1)** the initial saturation throughout the core was non-uniform, or *(2)* the core was not homogeneous.

Richardson and Perkins *(1957)* observed gravity segregation as water displaced oil in a lucite model that was *6* ft long, *6* in high, and **3/8** in thick. Waterfloods were made at *0.14* cc/sec and **0.31** cc/sec, and corresponded to reservoir velocities of *0.047* and 0.10 ft/day. Gravity segregation was observed at both flow rates, the water under-running the oil more at the lower injection rate. However, rate affected the recovery injection curve to a very minor degree. The important point was that at these same rates, a gas-liquid system would show even more gravity segregation due to the greater density difference.

Craig, Sanderlin, Moore, and Geffen *(1957)* used scaled reservoir models in their laboratory study of gravity segregation in frontal drives. In linear gas or water drives, gravity effects caused recovery at breakthrough to be *20%* of that otherwise expected. Although these results were obtained with immiscible fluids, Craig et al. believed them to be applicable to gas-drives in which capillary forces were "insignificant." Using scaling equations similar to those of Rapoport (1955), a convenient correlating term was obtained by multiplying the geometric dimension scaling parameter,

$$\frac{x}{y}\sqrt{\frac{k_y}{k_x}}$$

by the ratio of viscous pressure gradient to the gravity gradient,

$$\frac{q_i \mu_o}{\sqrt{k_x k_y}\, g \Delta p}$$

The result,

$$\frac{q_i \mu_o X}{k_x g \Delta\rho y}$$

was characterized by q_i, the injection rate divided by cross-sectional area; μ_o, the displaced fluid (oil) viscosity; **x**, system length; y, system thickness; k_x, horizontal specific permeability; Ap, fluid density difference; and g, gravitational constant. Smaller density differences, higher rates, and thinner and longer systems tended to reduce gravity effects.

One can appreciate the magnitude of gravity segregation by comparing the vertical and horizontal components of: **(1)** pressure or potential gradient, **(2)** velocity gradient, or **(3)** time required for gas to flow some characteristic distance.

Goode **(1978)** suggested dividing a characteristic length by fluid velocity to obtain a characteristic time. For instance:

$$\frac{t_V}{t_H} = \frac{\left(\frac{L}{u}\right)_V}{\left(\frac{L}{u}\right)_H} = \frac{\frac{L_V}{\left(\frac{k}{\mu}\right)_V \Delta\rho g}}{\frac{L_H}{\left(\frac{k}{u}\right)_H \frac{dp}{dx}}} = \frac{L_V \Delta p}{L_H^2 \Delta\rho g}$$

$$\text{when } \left(\frac{k}{\mu}\right)_H = \left(\frac{k}{\mu}\right)_V \text{ and } \frac{dp}{dx} = \frac{\Delta p}{L_H} \qquad (2\text{-}29)$$

In this case, L_V can be the radius and L_H the length of a horizontal, cylindrical core. The larger t_V/t_H, the less likely gravity segregation will influence the results.

The next section presents important aspects **of** the heat transfer involved in nonisothermal flow through porous media.

2.4 Heat Transfer in Nonisothermal Flow Experiments

Miller and Seban (1951) determined that thermal conductivity in the direction of flow was not important for the vaporizing propane flow experiments of Miller (1951). Atkinson and Ramey (1977) concluded that axial thermal conductivity was not important for the steady-state, nonisothermal liquid flow experiments of Arihara (1974) and Arihara and Ramey (1976). Atkinson estimated thermal conductivity from the results of Adivarahan, Kunii, and Smith (1962). Arihara (1974) determined the overall heat transfer coefficient for his experiments by injecting cold water into a hot core, hot water into a cold core, and finally, by injecting condensing steam into a cold core.

For the case of vaporizing liquid flow, Arihara evaluated axial thermal conductivity and radial heat transfer through the coreholder. Thermal conductivity was estimated using correlations prepared by Anand, Somerton, and Gomaa (1972), and by Gomaa and Somerton (1974). Arihara concluded that the heat flux due to conduction and radial convection was minor compared to the convective heat flux of the flowing fluid. In other words, he had nearly isenthalpic flow.

The next section discusses the effect of frequency on the capacitance of water-saturated porous media. As shown by Chen (1976), water saturation can be measured using a capacitance probe.

2.5 The Effect of Frequency on the Capacitance of Water-Saturated Porous Media

Dielectric phenomena have been described in detail by Smyth (1955). Hill (1969) has discussed the effect of the applied field frequency on polarizability. Hill also discussed the effect of frequency on interfacial

polarization as it occurs in heterogeneous mixtures. Sillars (1937; Smyth, 1955) and van Beek (1967) have presented specific examples of frequency and distribution effects in heterogeneous mixtures.

Keller and Licastro (1959) and Parkhomenko (1967) have presented a large amount of data demonstrating the effect of frequency and water saturation on core dielectric constant and resistivity.

A number of studies of porous media capacitance versus water content are discussed next. Anderson (1943) used an A.C. Wheatstone bridge at a frequency of 1 kHz and found low capacitance sensitivity at high water contents. Thomas (1966), using a bridge at 30 MHz, found high sensitivity at high water saturations with a nearly linear water content versus logarithm capacitance relationship. Laws and Sharpe (1969), using a bridge at 30 MHz, found that their results varied with salt concentration and cable length.

Meador and Cox (1975) recently described their successful efforts in developing a dielectric constant logging device to estimate formation brine saturation. Using a theoretical model, laboratory-scale experiments, and field trials, they concluded that a two-frequency sonde was required to account for both the dielectric constant and the formation resistivity. Meador and Cox found that 16 MHz and 30 MHz signals were adequate for the oil-brine systems they studied. Meador and Cox modified the Lichtnecker and Rother equation to obtain a general equation for the dielectric constant of porous media-fluid mixtures. However, no frequency dependence was built into this equation.

Chen (1976), using a 7.5 MHz frequency difference method, obtained a nearly linear relation between capacitance probe signal and water content.

The next section describes the primary objective of this study, which is to establish the basic character of steam-water relative permeability curves.

3. STATEMENT OF THE PROBLEM

The primary objective of this study is to establish the basic character of drainage steam-water relative permeability curves. Any difference existing between gas-liquid and single-component steam-water relative permeability curves should be identified. It is therefore necessary to perform experiments that will provide both boiling flow and gas drive relative permeabilities as a function of liquid water saturation. The next section describes the experimental apparatus used in this investigation.

4. EXPERIMENTAL APPARATUS

The experimental apparatus used in the steady, nonisothermal steam-water flow experiments is shown in the schematic diagram in Fig. 4-1. The core holder is located within the air bath. Deionized water is deaerated in a flask by vigorous boiling. One pump and accumulator maintains the confining pressure. The filtered, deaerated water is pumped through a furnace for preheat before entry into the core inlet. An accumulator is used to damp pump pulsations.

Effluent fluid from the core is passed through a heat exchanger, filtered, and the backpressure maintained with a fine metering valve. Timed weighing of the effluent water allows determination of total mass produced, and thus the mass flow rate. Pressures are measured at the inlet, outlet, and across the core with pressure transducers. Temperatures are measured with thermocouples and recorded at the inlet, around the air-bath, and along the length of the core. Liquid water saturation is measured along the core length with the capacitance probe and its associated electronics.

Slight modifications were made in this apparatus for the unsteady, nitrogen displacing water, isothermal experiments. As shown in Fig. 4-2, a gas injection line was added at the inlet, and a high-pressure gas-liquid separator was added at the outlet.

Details of the major parts of the apparatus are discussed in the remainder of this section.

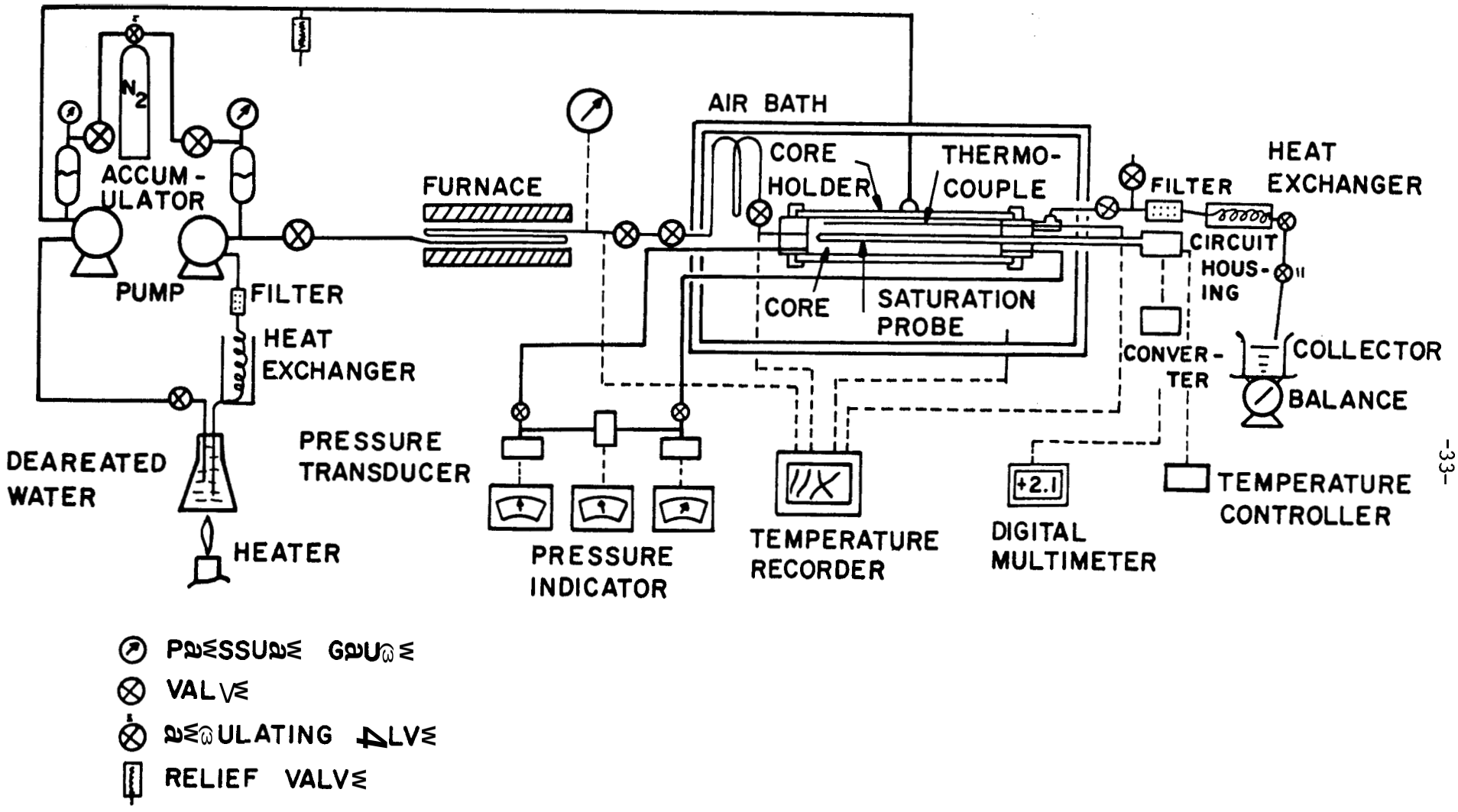

FIG. 4-1: SCHEMATIC DIAGRAM OF NONISOTHERMAL, STEAM-WATER FLOW APPARATUS

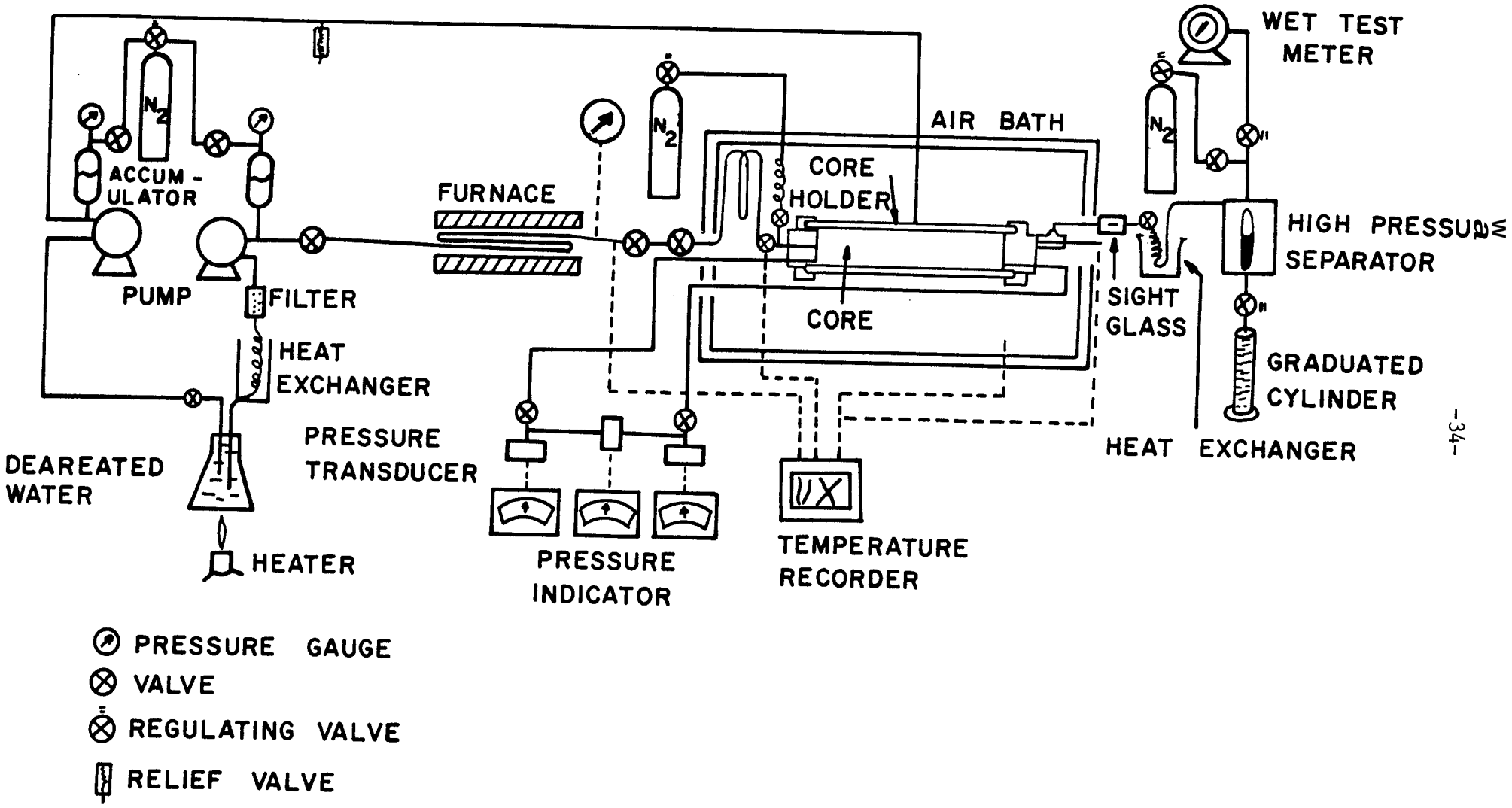

FIG. 4-2: SCHEMATIC DIAGRAM OF ISOTHERMAL, NITROGEN-WATER FLOW APPARATUS

4.1 Core Holder

The core holder used in the two-phase flow experiments is of the Hassler-type, as shown in Fig. 4-3. The core holder is similar to that used by Arihara (1974) and Chen (1976), and is based on a design by S. Jones of the Marathon Oil Co.

The core holder is made of *304* stainless steel for sufficient strength and corrosion resistance at elevated pressures and temperatures. The end caps are made of brass to reduce thread seizure problems. The brass inlet plug has two ports for fluid inflow and for pressure measurement. The brass outlet plug has three ports for fluid outflow, pressure measurement, and for the capacitance probe guide. The heat exchanger fitting shown in Fig. *4-4* was used to pass the thermowell through the outlet flow port.

The silicone rubber sleeve allows the application of confining pressure in the annular region to prevent fluid bypass at the sleeve-core boundary. Water **is** the preferred confining fluid because nitrogen gas can pass through the sleeve. Ethylene propylene, another type of elastomer, was also used as a sleeve material.

With the compression ring in place and a vacuum on the sleeve annulus, cores can be removed and inserted into the core holder assembly by removing the outlet end bracket and removing the outlet plug.

4.2 Liquid Water Saturation Measurement

The Baker capacitance probe described by Arihara *(1974)* and Chen *(1976)* is used to determine the liquid water saturation profile along the length of the synthetic consolidated sandstone core. Liquid water has a dielectric constant of *56* at *212°F* (100°C) and *28* at *464°F* (240°C),

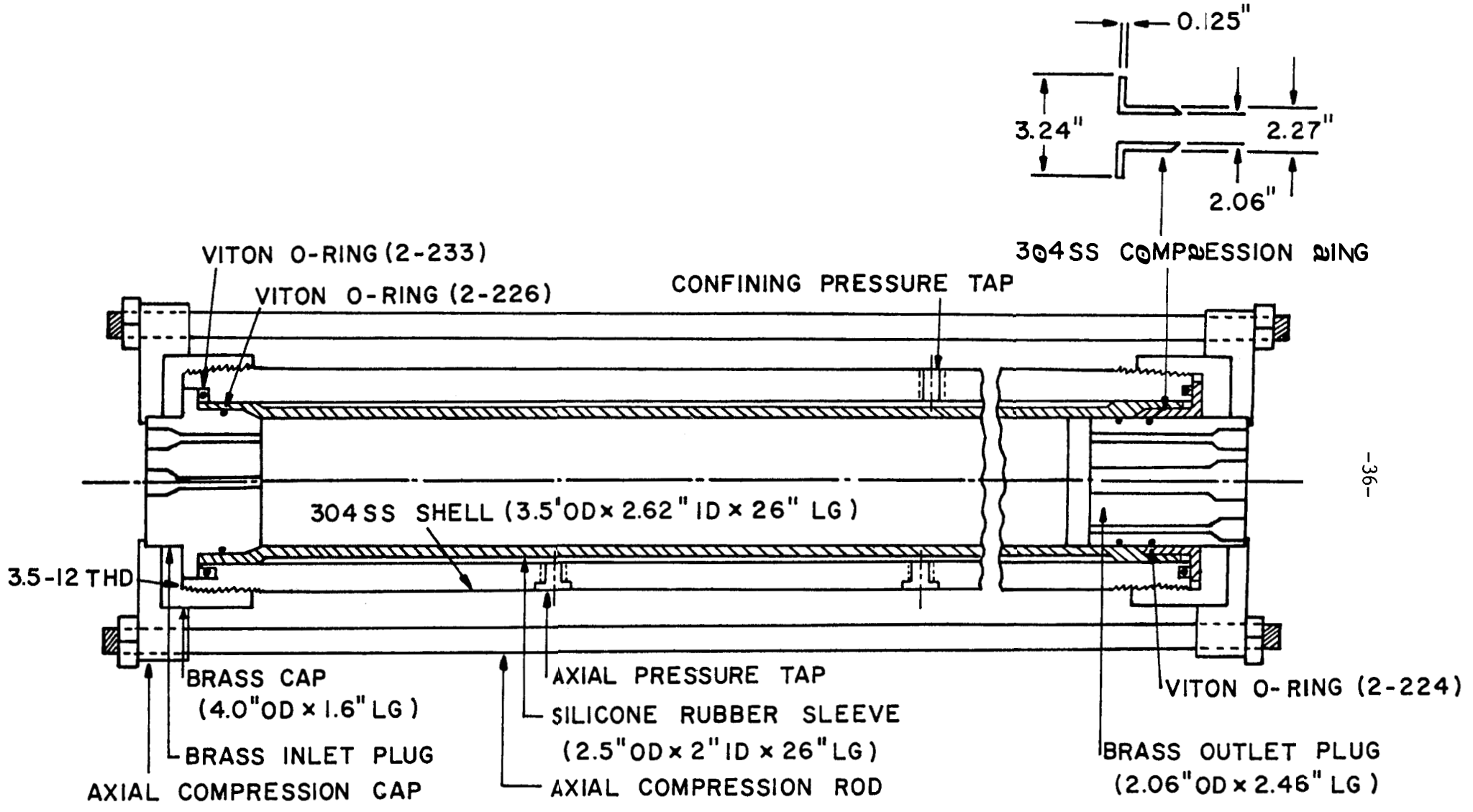

FIG. 4-3: CORE HOLDER FOR CONSOLIDATED SANDSTONE CORE

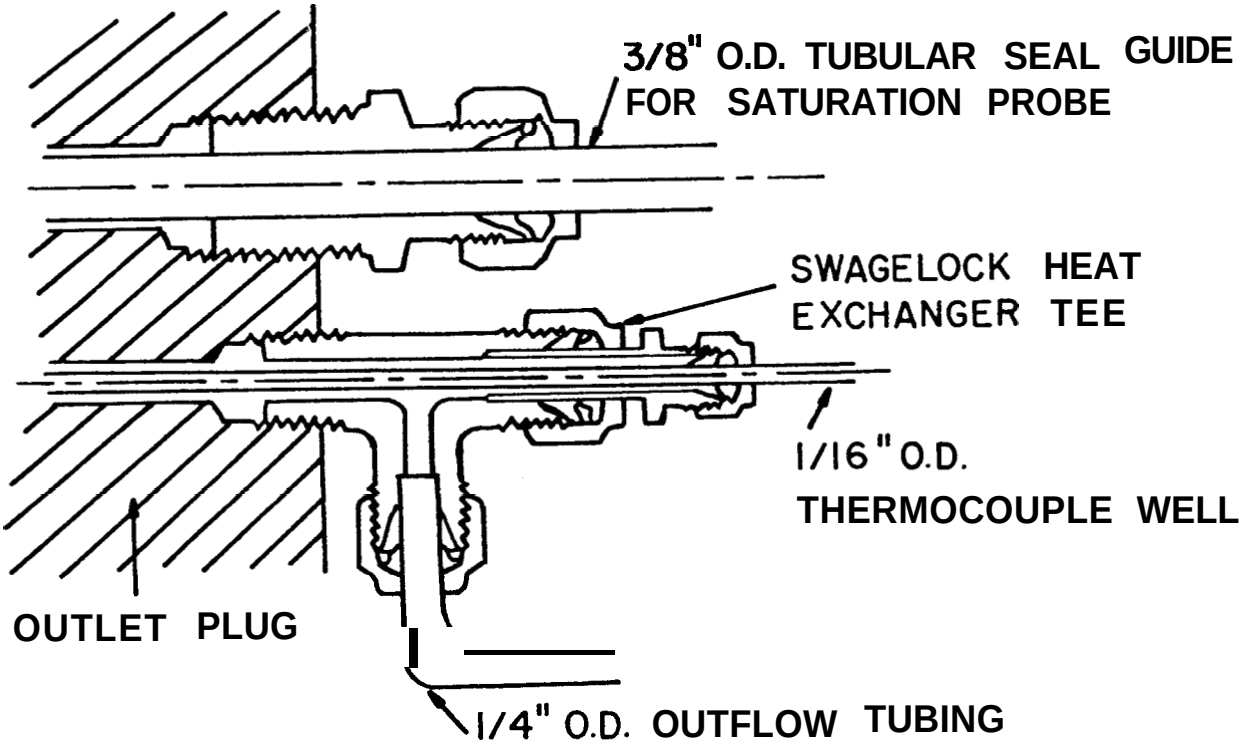

FIG. 4-4: DETAILS OF OUTLET FITTINGS (ARTHARA, 1974)

whereas sandstone is 4-6 and dry steam or gas is about **1.** This difference in dielectric constant allows the probe to detect liquid water saturation as the probe is moved through a probe guide cast into the center of the synthetic sandstone. Details of the probe and probe electronics are presented in Appendix 2.

The capacitance probe must be calibrated to provide a signal that can be related to liquid water saturation. Chen (1976) demonstrated that the same calibration resulted for synthetic consolidated sandstone short cores at room temperature as for long unconsolidated sand packs at elevated temperature, as shown in Fig. 4-5. Long consolidated cores at elevated temperature were not used for calibration due to the difficulty of obtaining uniform saturations along the core length.

Minor changes in the components of the probe and probe electronics and subsequent tuning adjustments required that the probe be recalibrated. Calibration was performed using long unconsolidated sand packs in the core holder shown in Fig. 4-6. Results are given in Section 6.

A Hewlett-Packard Q-meter was used to obtain sandpack capacitance as a function of frequency and liquid water saturation.

4.3 Air Bath

A NAPCO air bath maintains the core holder in a constant, high-temperature environment. A high-speed fan and louvres were added to maintain a uniform (±5°F:3°C) temperature distribution around the core holder.

The working volume is 41-1/4 in by 17-1/2 in by 24 in. The unit is rated at 2,800 watts with a maximum operating temperature of 400°F (204°C).

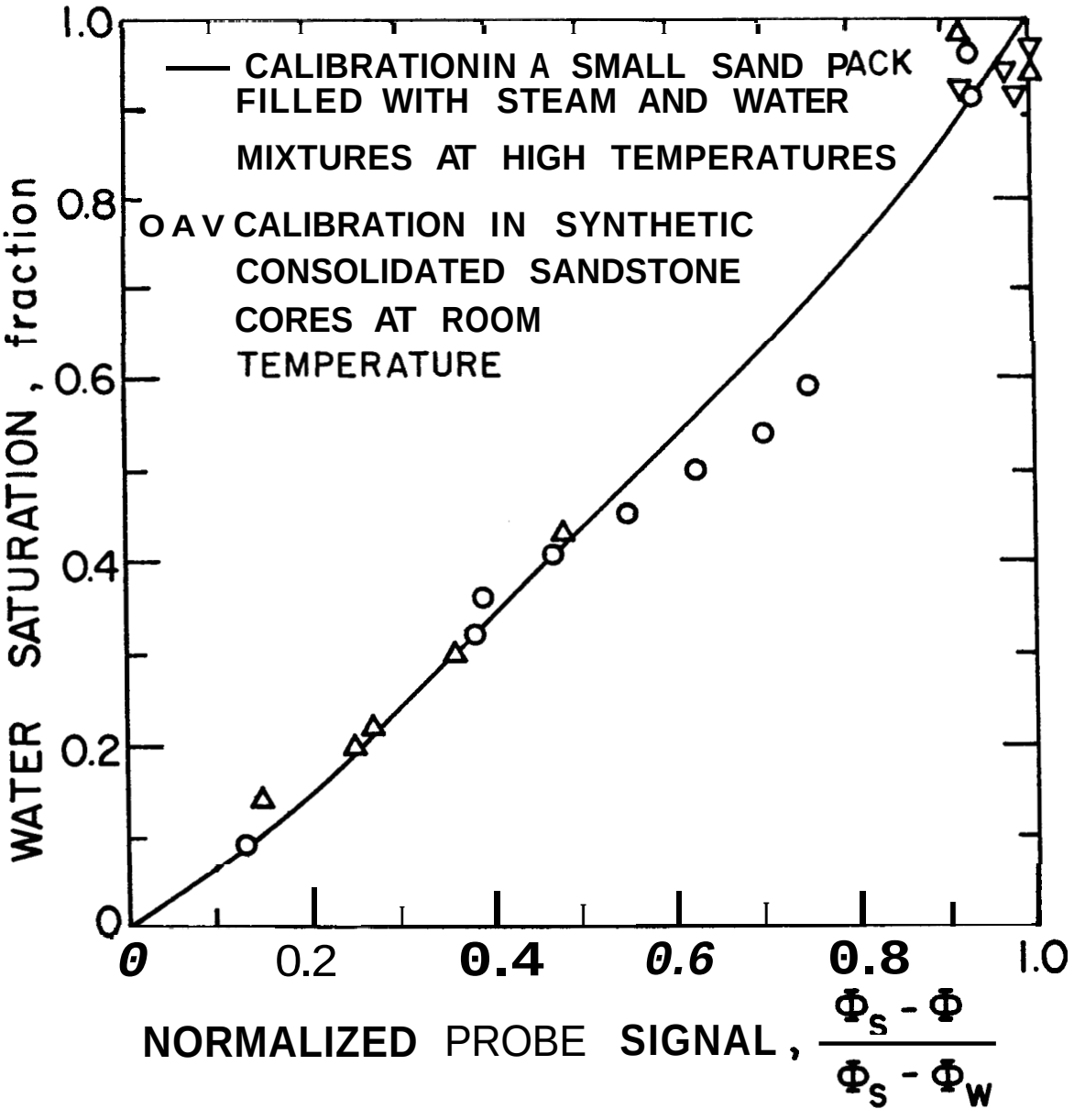

FIG. 4-5: COMPARISON OF THE CALIBRATION OF THE PROBE IN DIFFERENT MEDIA AND AT DIFFERENT OPERATING TEMPERATURES (CHEN, 1976)

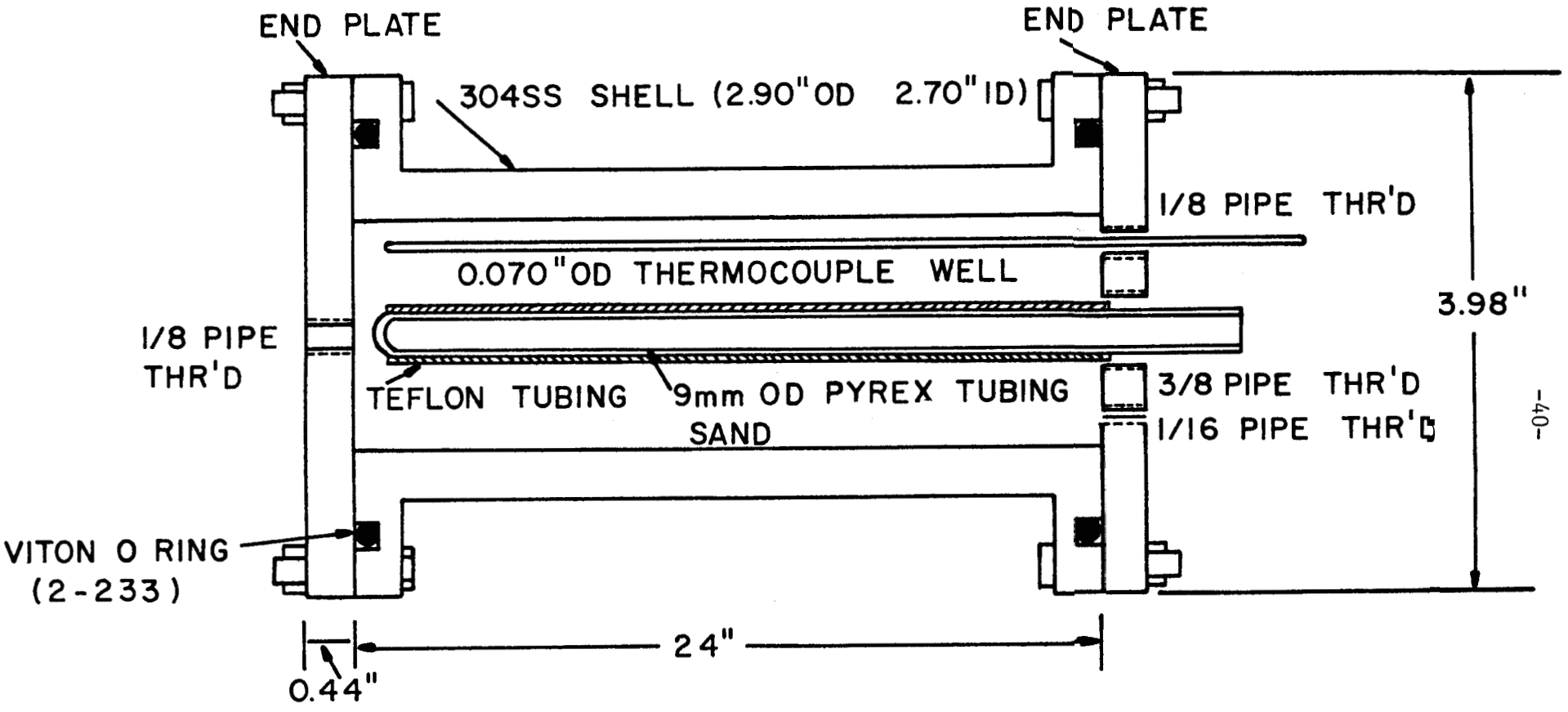

FIG 4-9: CORE HOLDER FOR UNCONSOLIDATED SAND PACK (CHEN, 1976)

4.4 Temperature Measurement

Type J, iron-constantan, sheathed thermocouples were used to measure all flowline, air bath, and core temperatures. Axial temperatures in the core were measured with a 0.040 in (1.02 mm) outside diameter thermocouple sliding within a 0.072 in (1.83 mm) outside diameter, 0.009 in (0.23 mm) wall thickness stainless-steel tube. The tube was closed (welded) at one end and cast in the synthetic consolidated sandstone core. The rated accuracy of the thermocouples was ± 3/8 - 3/4% or ±2-4°F (1-2°C) at 350°F (177°C).

A 24-point recorder was used to record all temperatures. The recorder has a sensing time of 1.5 sec per point. The rated accuracy of the recorder is ±0.3% of span, or ±1.8°F (1.0°C).

A single-point thermocouple-recorder calibration check was made using boiling water. At this temperature, the additive rated error is ±4-6°F (2-3°C) at 350°F (177°C). The thermocouples indicated the boiling temperature of water to be 212°F ±2°F.

4.5 Pressure Measurement

Diaphragm-type variable magnetic reluctance pressure transducers were used to measure pressure drop across the core and pressure at the core inlet and outlet. Pressure displaces a stainless steel diaphragm and varies the inductive loop between two "E" cores. A digital voltmeter is used with a carrier demodulator transducer indicator to provide digital pressure readout. The unit is calibrated on a nitrogen gas dead weight tester. Transducer linearity is rated at 0.5% full scale for the best straight line. Hysteresis is rated at 0.5% of pressure excursion. The transducer indicator accuracy is rated at ±1% meter full scale or 0.01% static change with

suppression control. The 3-1/2 digit, digital voltmeter has a **0.1%** of reading + one digit accuracy. Calibration indicated an overall reproducible accuracy of **±1%** of full scale.

Several bourdon tube pressure gages were also used to allow a visual check of confining pressure and core inlet pressure.

4.6 Pump and Accumulator

The controlled volume pump is designed to displace up to 5.1 gallons per hour (5.4 cc/sec) at **100** psig (6.8 atm). A plunger operates in oil at a fixed stroke. The resulting pressure actuates a Teflon diaphragm, which displaces the pumped fluid. Although a fixed volume of oil is displaced by the plunger, pumping capacity is controlled by adjusting the volume of oil that bypasses the diaphragm cavity. The rated repetitive accuracy of the discharge volume is **±1%** of range, or ±0.051 gallons per hour (±0.054 cc/sec). Observed accuracy was about ±5% setting in the range of settings used. A 60-micron filter is located upstream of the pump.

A hydropneumatic accumulator immediately downstream of the pump helps suppress the pump pulsations. Nitrogen gas, precharged to 150 psig (10-2 atm), is separated from the pumped fluid by a rubber bladder. Nitrogen pressure can be adjusted to optimize pumping performance.

4.7 Electric Furnace and Temperature Controller

A 2,000°F (1,093°C) rated high-temperature tubular furnace is used to heat the core inlet water. The stainless steel injection tubing makes three passes through the 2 in (5.1 cm) diameter by 24 in (61 cm) length furnace working volume. A percentage timer-type controller is used to maintain the desired furnace temperature. The furnace exit fluid temperature for a given control setting is a function of mass flow rate.

4.8 Flowline Sight-Glass

For the isothermal gas-drive experiments, a glass tube Fisher-Porter flowrator is used as a sight glass to identify the instant of gas breakthrough. The produced fluids are passed through a heat exchanger before passing through the sight glass.

4.9 High-pressure Gas-Liquid Separator

For the isothermal gas-drive experiments, the fluids are produced into a stainless steel, high-pressure gas separator. A regulating valve allows the liquid to be produced from the separator at a rate such that the gas-liquid level remains constant. A sight glass is used to identify the liquid level. Another regulating valve is continually adjusted to maintain a constant gas backpressure on the separator and core outlet. To establish separator pressure, nitrogen is injected into the separator while water only is pumped through the core. A change in water level in the low volume separator can be read to ± 1 mℓ water using the graduated sight glass. The gas balance is easy to maintain when the separator pressure and liquid level are kept constant.

4.10 Porous Media

Two types of porous media were used in this study. Unconsolidated sand was used for the capacitance probe calibration and a synthetic consolidated sandstone was used for the two-phase flow experiments.

4.10.1 Unconsolidated Sand Packs

The unconsolidated sand packs used for the static probe calibration runs were made with either 18-20 mesh sand or a uniform, 20-30 mesh silica sand. Unconsolidated sand was used for calibration because thermal

equilibrium was reached faster with the sand pack than with a consolidated core in a Hassler sleeve, as well as for other reasons.

4.10.2 Consolidated Sandstone Cores

Wygal (1963), Heath (1965), Evers et al. (1967), Arihara (1974), and Chen (1976) have described techniques for making synthetic, consolidated porous media. The cores used in the two-phase flow experiments in this study were made using the techniques and materials suggested by Arihara (1974) and Chen (1976).

The Fondu cement (Lone Star Lafarge Company) used in the consolidated cores is primarily mono-calcium aluminate ($CaO \cdot Al_2O_3$) rather than the tricalcium silicate ($3\ CaO \cdot SiO_2$) found in portland cement. On hydration, Fondu cement forms di-calcium aluminate and the relatively inert alumina is liberated.

Fondu cement was developed for making a concrete that would not be attacked by sea water or sulphate groundwater. It is also useful for high-temperature environments. The resistance to pure water is high, but the resistance to fluids with a pH of 4 or less is low.

Fondu cement sets slower than portland cement, but its 24-hr strength is greater than the strength of portland cement after 28 days. There is little volume contraction when the concrete is wet cured. One potential problem is the conversion that may occur over long periods of time in the presence of water at temperatures greater than 77°F. When $CaO \cdot Al_2O_3 \cdot 10\ H_2O$ converts to $(CaO)_3Al_2O_3 \cdot 6\ H_2O$, there may be a reduction in strength, and an increase in porosity and permeability.

Silica sand and gravel undergo a volume change and may cause spalling if used in concrete subject to temperatures greater than 400°F.

Despite these limitations, Fondu cement appears to have good overall qualities for use in synthetic, consolidated sandstone geothermal cores.

4.10.3 Synthetic Consolidated Sandstone Core Mold

The core mold shown in Fig. 4-7 is made of a 31 in length of 2 in inside diameter polypropylene tubing cut lengthwise to form two halves. The inside of each half-tube is covered with heavy duty duct tape to help provide a clean, smooth surface for the core mold. To assemble the mold, the two halves of polypropylene are then taped together along the cut edges and clamped between two halves of 2 in inside diameter brass tubing using stainless steel hose clamps. The clamped tubing is then assembled in the bracket and endpieces shown in Fig. 4-7. The bottom, or outlet, end of the core mold is an aluminum disk with an o-ring seal for the clamped tubing and 3 ports. One port is for the capacitance probe guide, which is a 9 mm outside diameter, 24-1/4 in (61.6 cm) long pyrex tube with one end closed. The open end has a 3/8 in (9.5 mm) outside diameter, 6-1/2 in (16.5 cm) long stainless steel tubular seal. The stainless steel end passes through the outlet end disk of the core mold. The second port is for the thermowell (thermocouple probe guide), which is a 28-30 in (71-76 cm) length of 0.072 in (1.83 mm) outside diameter, 0.009 in (0.23 mm) wall thickness, 321 stainless steel tubing. The third port is for the mold outlet valve.

Before assembly, the glass portion of the probe guide is inserted into a zero-gage, thin-walled (0.015 in - 0.38 mm) teflon tubing to reduce the risk of glass breakage due to the glass, metal, and core thermal

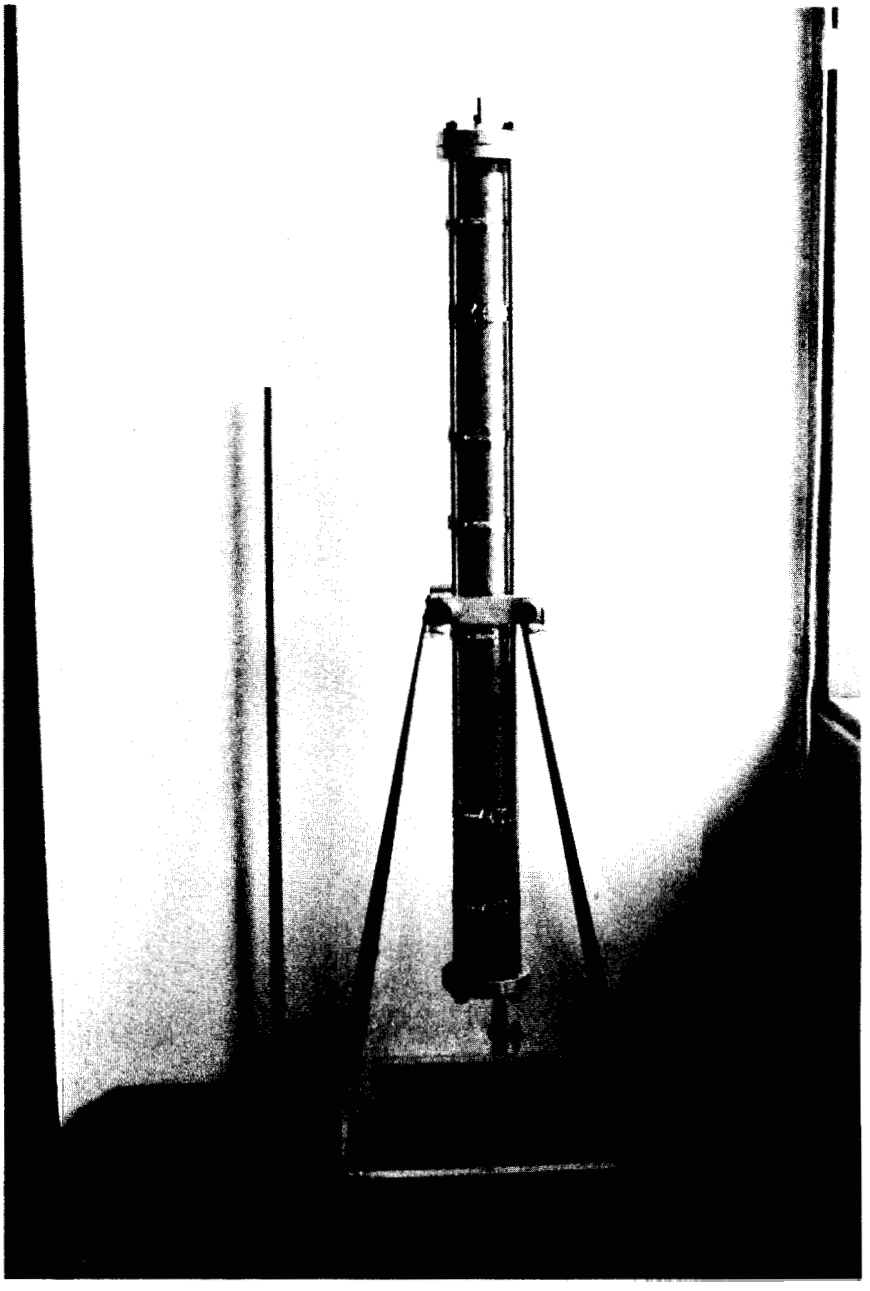

Fig, *4-7:* CORE MOLD APPARATUS [DEVELOPED BY ARIHARA *(1974)* AND CHEN (1975)] USED TO FABRICATE SYNTHETIC CONSOLIDATED CORES

expansion. Prior to insertion of the glass into the teflon tubing, the teflon tubing is first stretched slightly with a rod whose tip is flared to a diameter slightly larger than the diameter of the teflon tubing. The glass tubing within teflon tubing must be placed in an air bath at over 300°F to achieve the shrinkage that might occur under operating conditions.

Quartz glass was also used for the probe guide. However, it was found that the quartz glass broke or cracked almost as easily as the pyrex glass.

The next section presents the procedure used in the calibration and relative permeability experiments.

5. EXPERIMENTAL PROCEDURE

The experimental procedure is described in detail for: **(1)** calibration of the capacitance probe at high temperature, (2) fabrication of the synthetic consolidated sandstone cores used in the flow experiments, *(3)* steam-water, steady, nonisothermal, two-phase relative permeability experiments, and *(4)* nitrogen-water, unsteady, isothermal, gas-drive relative permeability experiments.

5.1 Probe Calibration

Either 18-20, 20-30, or 80-170 mesh sand was poured into the inlet end of the core holder shown in Fig. *4-6.* The glass probe guide and the thermowell were fixed in place at the core holder outlet end. The core holder was lightly tapped on the side and the sand surface lightly tapped from time to time, using the centralizer. The unconsolidated sand pack was then installed in the air bath.

At the temperature of interest, the sand pack was evacuated overnight. The next day, the core was saturated (under vacuum) with filtered, deionized water. The water was deaerated by vigorous boiling.

In a manner similar to that reported by Chen (1976), the probe signal was recorded at several locations along the length of the core. The core was partially depleted, allowed to reach thermal equilibrium (1-**10** hours), and the probe signal again recorded at several locations. This process was repeated until the core was dry. Average core water saturation was known after each depletion by a mass balance. Probe response was

normalized at each point using $((\Phi_s-\Phi)/(\Phi_s-\Phi_w)$ and averaged for the core.

This calibration technique was used with both the Baker-type electronics at 7.5 MHz, and with the Hewlett-Packard Q-meter from 40 kHz to 14 MHz.

The next section presents the techniques used in the fabrication of the synthetic sandstone cores.

5.2 Synthetic Sandstone Fabrication Technique

The following procedure was used to form cores with a permeability of 20-100 md and a porosity of 30-40%.

1) Sift about 2,400 g (80 wt %) of 80-170 mesh Ottawa silica sand. Wash and dry.

2) Mix sand thoroughly with 12-15 g (0.5 wt %)water to wet sand grains.

3) Gradually blend in about 600 g (20 wt %) Fondu calcium aluminate cement. Mix thoroughly.

4) Pour small quantities of the mixture into the core mold. Vibrate sparingly and lightly. Tap mixture surface with centralizer from time to time to eliminate bridging.

5) Inject deionized water from core mold top with a head of 3-5 ft of water.

6) Shut in inlet and outlet valves after water breakthrough is observed (2-5 hrs).

7) Allow core to hydrate in mold for 17 to 24 hrs.

8) After 17-24 hrs, carefully remove core from mold.

The following steps should be taken to avoid core cracking:

1) Do not use old cement that has hard lumps. Using cement which has absorbed moisture from the air causes increased setting times and decreased core strength.

2) Core mold should be clean before packing. Mold should be lined with new duct tape. The core may stick to a dirty mold and make successful removal difficult.

3) Wet cure the core after removal from mold. Wrap core in wet paper towels or spray with water and wrap in plastic to keep core moist.

The next section presents the procedure used in the steam-water, nonisothermal flow experiments.

5.3 Steam-Water Relative Permeability Experiments

At the temperature of interest, the core was evacuated overnight. Confining pressure was maintained in the 300-500 psig range. The next day, the core was saturated (under vacuum) with filtered, deionized water. The water was deaerated by vigorous boiling. Several pore volumes of waterwerepumped through the core. The outlet end regulating valve was then opened to maintain the desired flowrate and pressure drop across the core. Inlet end pressure was high enough above the vapor pressure to insure that only liquid water flowed into the core. Outlet end pressure was maintained below the vapor pressure.

Once the temperature profile along the core was stabilized, it was recorded along with the probe signal profile. In addition, inlet and outlet pressures, pressure drop, and air bath temperature were also recorded. The constant water flow rate was determined by timed mass weighings. The cold probe signal in air was also recorded to insure that

no zero shift occurred. The probe signal profile was obtained for the cases where $S_w = 1.0$ and $S_w = 0$ so that the normalized probe signal, $\Phi^* = (\Phi_s - \Phi)/(\Phi_s - \Phi_w)$ could be calculated. An isothermal, compressed water flow test was also run to obtain the absolute permeability to water.

The next section presents the procedure used in the unsteady, isothermal, gas-drive experiments.

5.4 Nitrogen-Water Relative Permeability Experiments

The core was saturated as described in Section 5.3. Water was pumped through the core, through the short heat exchanger, and into the high pressure gas-liquid separator. Water was drained from the separator using a regulating valve such that the liquid level in the separator remained constant. The back-pressure on the core was maintained above the vapor pressure by injecting nitrogen into the separator. Water flow rate, pressure drop, core, air bath and room temperatures, and confining pressure were recorded to determine the absolute permeability to water.

To initiate the gas-drive, the water injection line was closed at the core inlet as the gas injection line was opened. At the same time, a laboratory clock was started. The water regulating valve was adjusted to maintain a constant liquid level in the separator. Time, cumulative water production into a graduated cylinder, inlet and outlet pressure, and pressure drop were recorded. When gas breakthrough was first noticed in the outlet flowline sightglass, the outlet gas regulating valve was adjusted to maintain a nearly constant pressure drop across the core. Inlet pressure was regulated from a cylinder, and was therefore almost constant. Gas production into a wet test meter was also recorded as a function of time. Atmospheric pressure was also recorded, although its

variation was not important at the high pressures used in these experiments.

The next section presents the results of the calibration and relative permeability experiments,

6. RESULTS AND DISCUSSION

The results of this study are presented in the following three sections. The first section discusses the calibration of the capacitance probe. The effect of frequency on the calibration curve is also discussed. The second section presents steam-water relative permeability curves generated from nonisothermal, steady, steam-water flow experiments. Water saturation is measured with the capacitance probe. Finally, the third section presents gas-water relative permeability curves obtained from isothermal, unsteady, nitrogen-displacing-water flow experiments. The effect of temperature on relative permeability is also discussed.

6.1 Capacitance Probe Calibration

The capacitance probe calibration curves used later in this study were developed by obtaining the 100% water probe signal, Φ_w, at a number of locations along the length of a sand pack completely saturated with liquid water. As the core was stepwise depleted, the probe signal, Φ, was recorded at each location. After the final depletion, the signal for 100% steam, Φ_s, was recorded at each location in the steam-saturated sand pack. For each location, the normalized probe signal:

$$\Phi^* = \frac{\Phi_s - \Phi}{\Phi_s - \Phi_w} \qquad (6\text{-}1)$$

was calculated. The Φ^* values along the length of the core were then arithmetically averaged at each average water saturation, S_W, to obtain a probe signal - water saturation correlation.

The problem of returning to precisely the same location to measure water Saturation after each depletion was a minor problem because saturation gradients across the sand pack were not large after thermal equilibrium had been attained.

Water saturations for the calibration runs were approximated within 1% error as the mass fraction. Chen (1976) obtained the following expression for volumetric water saturation:

$$S_w = \frac{\bar{v}_w}{\bar{v}_s - \bar{v}_w}\left(\frac{m\bar{v}_s}{V_p} - 1\right) \qquad (6\text{-}2)$$

where:

$\bar{v}_w$ = specific volume of water

$\bar{v}_s$ = specific volume of steam

V_P = pore volume of sand pack

$m = m_s + m_w$ = mass of steam and water in sand pack

Since the pore volume equals the product of the 100% liquid saturated water mass, m_i, and the water specific volume, the saturation equation can be written:

$$S_w = \frac{m}{m_i}\left(\frac{\bar{v}_s}{\bar{v}_s - \bar{v}_w}\right) - \frac{\bar{v}_w}{\bar{v}_s - \bar{v}_w} \qquad (6\text{-}3)$$

With less than 1% error, $S_w = m/m_1$ is a good approximation for the saturated temperature and pressure ranges investigated in this study.

The capacitance probe was first calibrated for water saturation response to verify Chen's calibration curve (Fig. 4-5). However, using an 18-20 mesh sand and four twelve-volt batteries for the power supply, a much different calibration curve resulted, as shown in Fig. 6-1.

A great deal of time and effort was spent trying to isolate the cause of this shift in the calibration curve. Several months had passed since the equipment was last used. Finally, several electronic components were replaced, the 7.5 MHz operating frequency was verified, and the built-in regulated power supply repaired.

Figure 6-2 shows four calibration runs using either 80-170 or 20-30 mesh sand at 310°F. This calibration curve is in good agreement with the one developed by Chen. The recently repaired Baker-type electronics package was used in all four runs. The data expressed as triangles were obtained using a different power supply and frequency difference-to-analog converter than that used to obtain the data expressed as a circle or a square. Since the regulated power supplies appeared to be adequate, the four 12 volt lead-acid storage batteries used by Chen were no longer used.

Limited data taken with an 80-170 mesh sand yielded more scatter in the calibration curve than did runs with 20-30 mesh sand. This may have been caused by fines migration or non-uniform packing. Fine-grained sands tended to plug the outlet filters and cause long depletion run times.

During the course of the calibration experiments, a number of the probes were broken and rebuilt. The repair generally required replacement of the silver-plated glass tubing. It is therefore suspected that slight differences in probe construction had a minor effect on the

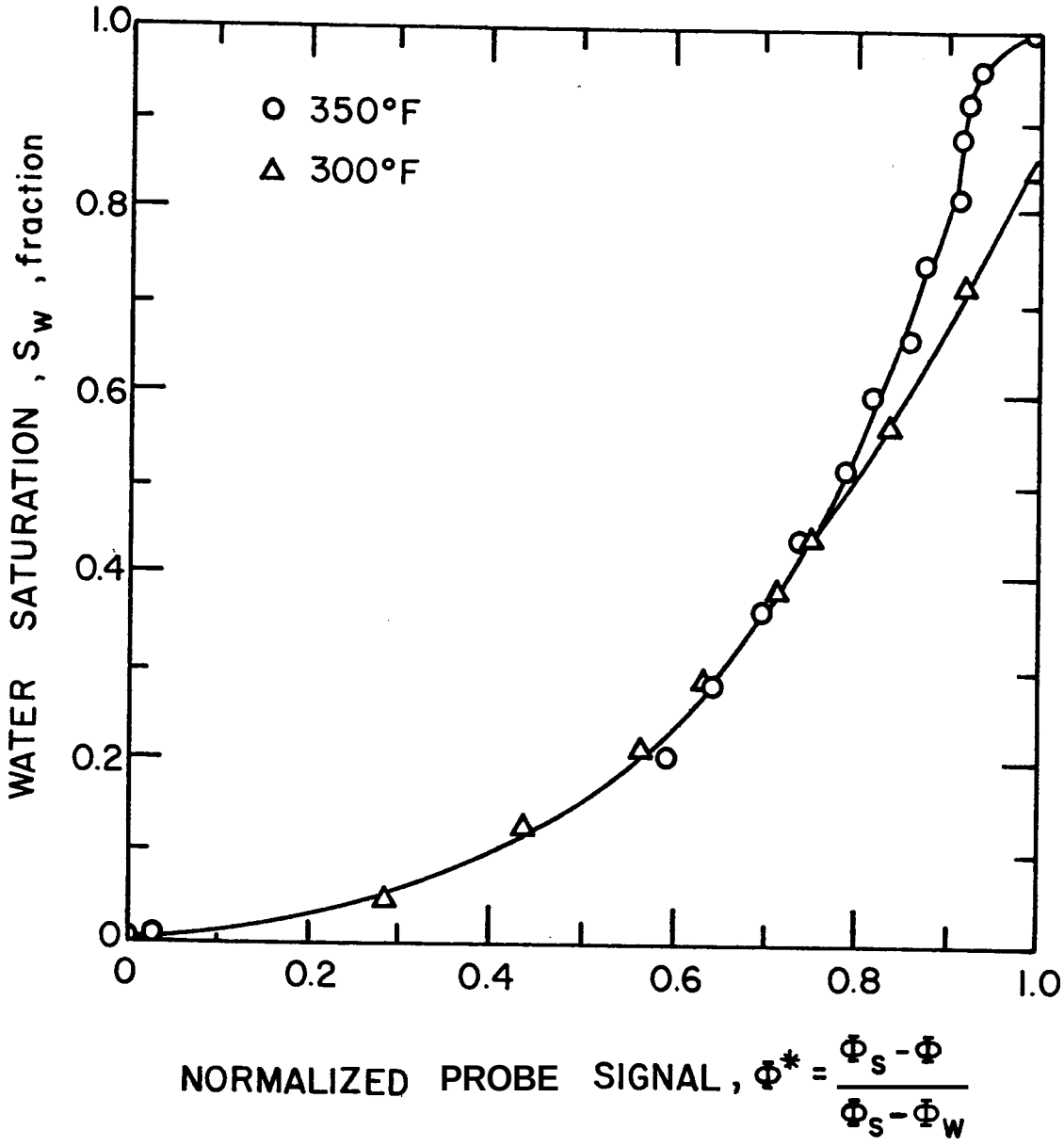

FIG. 6-1: WATER SATURATION VS NORMALIZED PROBE SIGNAL IN AN UNCONSOLIDATED SAND PACK (18-20 MESH) (BEFORE REPAIRING ELECTRONICS)

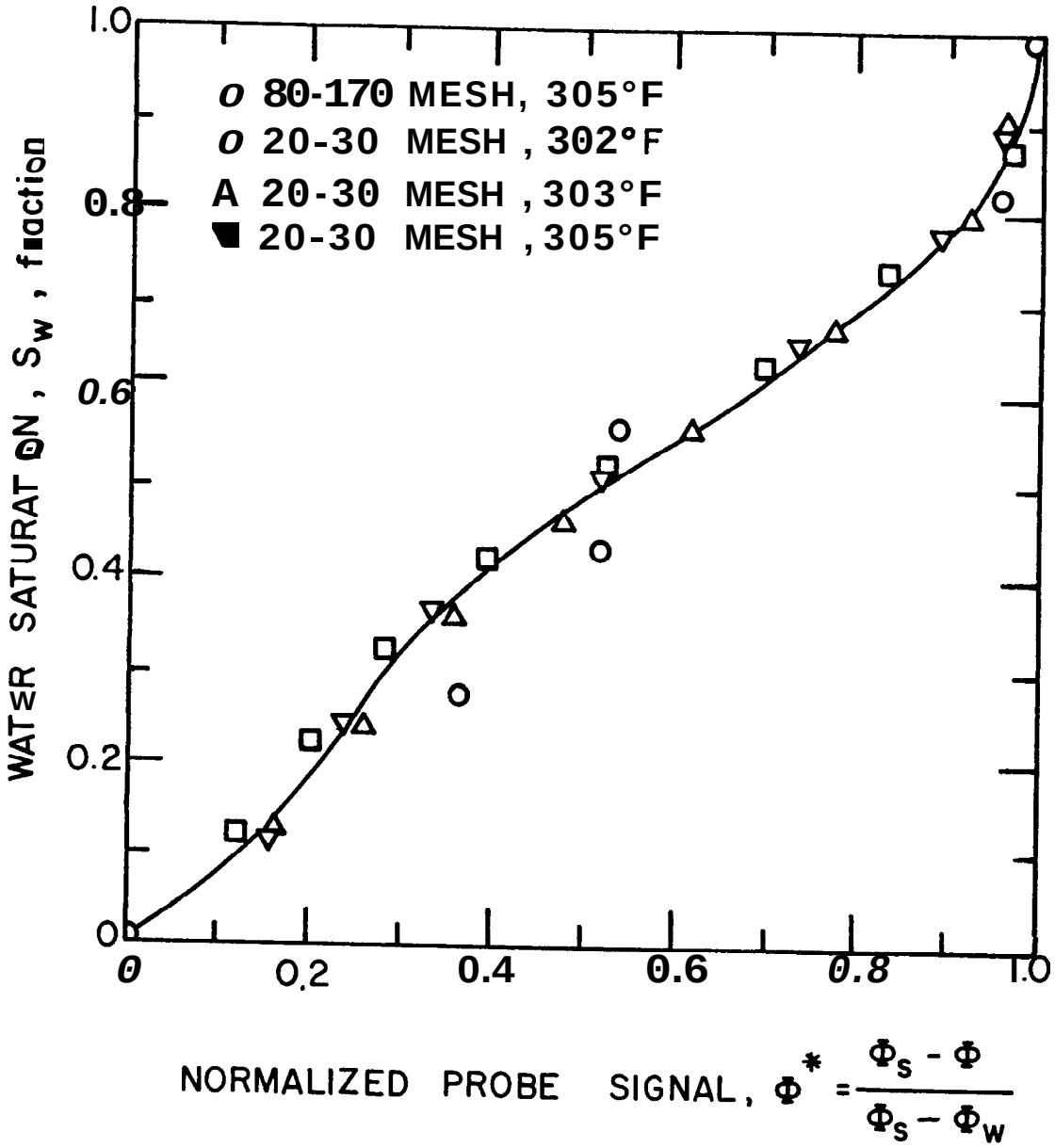

FIG. 6-2: WATER SATURATION VS NORMALIZED PROBE SIGNAL FOR SEVERAL SAND GRAIN SIZES IN UNCONSOLIDATED SAND PACKS

calibration response of each probe. Nevertheless, the calibration results shown in Fig. 6-2 show small scatter and are considered satisfactory.

6.1.1 Effect of Frequency on Probe Response

A study of the effect of frequency on probe response was also made. The dielectric literature suggested that heterogeneous materials show a strong frequency dependence. The results of this study are shown in Fig. 6-3. A more detailed run at 7.5 MHz is presented in Fig. 6-4. Normalized capacitance is: (1) nearly independent of frequency in the 750 kHz - 14 MHz range, and (2) strongly dependent on frequency in the 40-180 kHz range. This information is useful in that the higher frequencies can give the best water saturation resolution over a wide range of water saturation. The lower frequencies would be most useful for detecting small water saturation changes at very low water saturations.

The frequency-dependence study was carried out with a Hewlett-Packard Q-meter. Each resonant frequency required a different coil. The response of the Q-meter: coil assembly was affected by room temperature variation and required a correction of roughly -0.040 pf/°F. The 14 MHz readings were too unstable to allow temperature correction. A temperature correction of 0.04 pf/°F would shift the 14 MHz curve to the right for a closer agreement with the 7.5 MHz and 750 kHz curves. The 47 mH coil used at 40 kHz did not demonstrate a well defined temperature sensitivity.

The Q-meter provided an output in terms of a capacitance (picofarad) difference at the resonant frequency. This was in contrast to the Baker-type electronics, which provided a digital output that was related to the resonant frequency difference between the tuning (or sensing) circuit and a reference frequency. The Baker-type electronics package was chosen for general use because its operation required much less effort than the Q-meter.

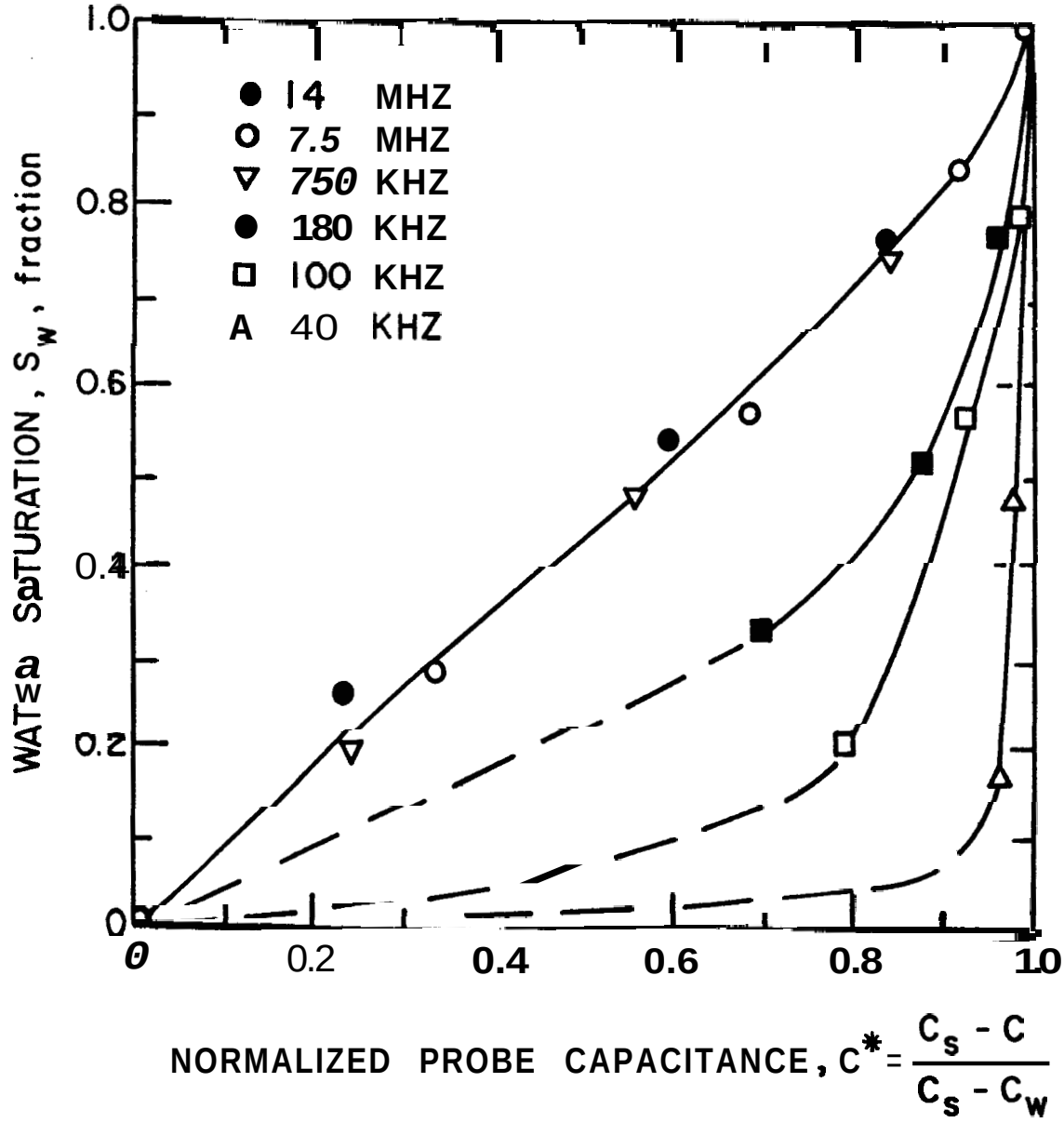

FIG. 6-3: WATER SATURATION VS NORMALIZED PROBE CAPACITANCE FOR SEVERAL FREQUENCIES IN AN UNCONSOLIDATED SAND PACK (310°F, 20-30 MESH SAND)

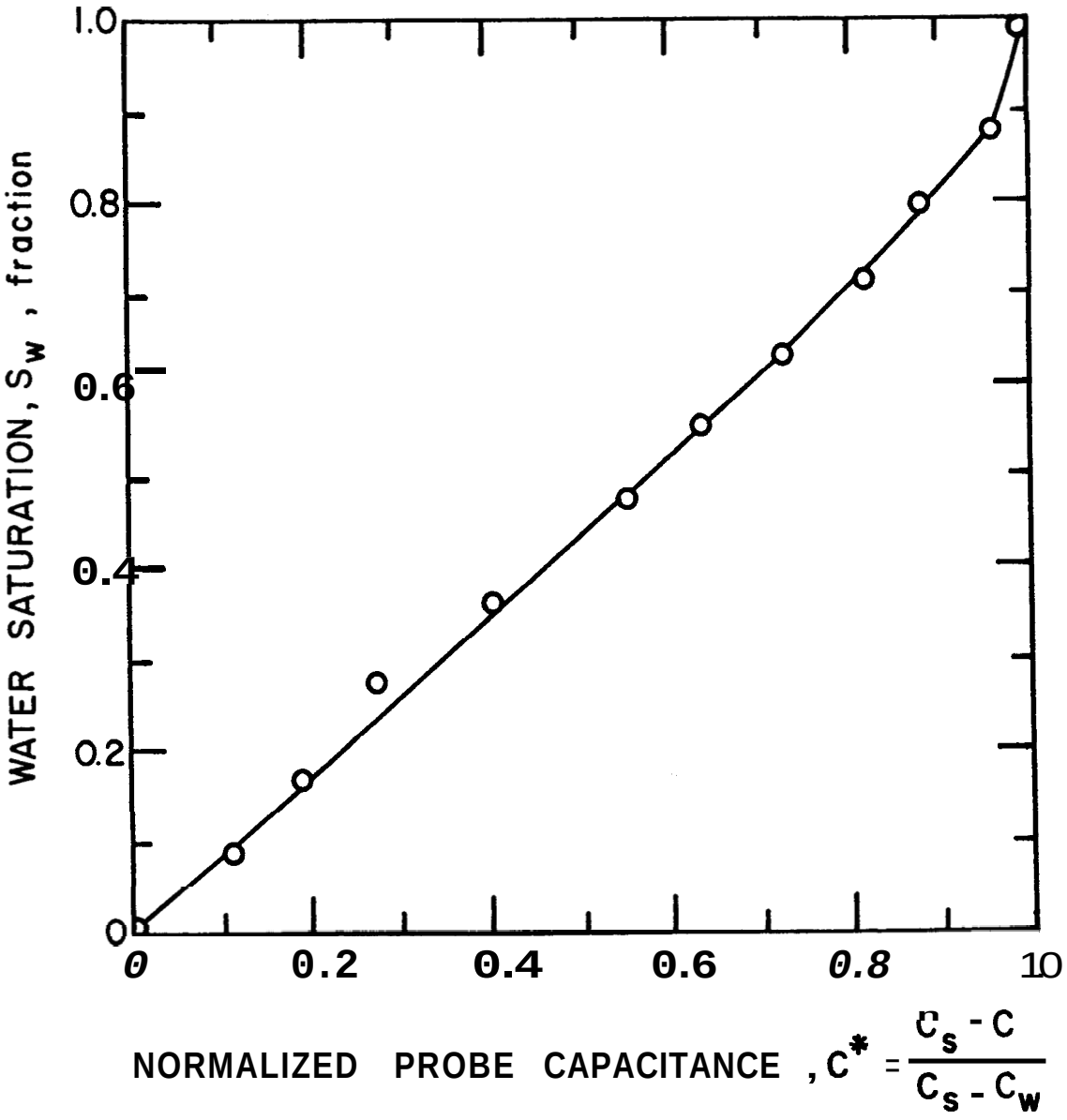

FIG. 6-4: WATER SATURATION VS NORMALIZED PROBE CAPACITANCE IN AN UNCONSOLIDATED SAND PACK (20-30 MESH, 305°F, 7.5 MHz)

It is interesting that the normalized capacitance (C^*) vs water saturation (S_w) and the normalized frequency (f_r^*) vs water saturation (or Φ^* vs S_w) calibration curves are similar at 7.5 MHz.

Since:

$$C = \left(\frac{1}{2\pi f_r}\right)^2 \frac{1}{L_c} \tag{6-4}$$

where:

C = capacitance in oscillating circuit

L_c = inductance in oscillating circuit

f_r = resonant frequency of circuit

Then:

$$C^* = f_r^* \quad \frac{(f_r+f_{rs})f_{rw}^2}{(f_{rw}+f_{rs})f_r^2} \tag{6-5}$$

where:

$$C^* = \frac{C_s-C}{C_s-C_w} \tag{6-6}$$

$$f_r^* = \frac{f_{rs}-f_r}{f_{rs}-f_{rw}} \tag{6-7}$$

Subscripts: $s = C$ or f_r measured in 100% steam-saturated core

$w = C$ or f_r measured in 100% water-saturated core

The group $(f_r+f_{rs})f_{rw}^2/[(f_{rw}+f_{rs})f_r^2]$ is almost unity because the resonant frequency for the steam-saturated core varies by only about 1% from the resonant frequency for the water-saturated core. Thus, $f_r^* \approx C^*$ is a good approximation at 7-10 MHz. These statements have been verified

by converting the change in capacitance data, AC, to capacitance, C, and then to frequency, f_r. Identical values are obtained for Φ* and C* to two decimal places.

The next section presents some of the temperature effects that should be considered when using the saturation probe.

6.1.2 Effect of Temperature on Probe Response

As the probe is pulled out of the core holder, more of the probe is exposed to the room temperature. This causes a gradual cooling of the probe with time. For a partially extracted probe, probe output can decrease by up to 0.6 mv given a cooling time of 2-3 minutes. This tends to increase the apparent steam saturation with time. To obtain repeatable results: (1) the probe should be fully inserted into the core, (2) pulled out and the reading taken immediately, and (3) the probe should then be left fully inserted into the core for 2-3 min before the next reading. A long time is required to obtain a profile of many points along the length of the core using this procedure.

Since the maximum variation in probe response is 15-30 mv, a variation of 0.6 mv caused by probe temperature change represents a 2-4% error. To decrease the time required for a complete traverse, an alternate procedure was actually used. The same time schedule was used for the probe traverse at each stage in the core depletion process. The use of the time schedule allowed the probe temperature change to be similar for each traverse, thus reducing the error below the above-mentioned value of 2-4%.

As noted by Chen (1976), the calibration curves for the capacitance probe were found to be nearly independent of temperature.

Because the dielectric constant of water decreases with increasing temperature, the capacitance also decreases and the resonant frequency ($f = [2\pi\sqrt{LC}]^{-1}$) increases. The normalized signal, or frequency $(f_s-f)/(f_s-f_w)$, discussed by Chen would therefore be expected to decrease with increasing temperature because $f_s > f$.

However, a second temperature effect also exists. At higher temperatures, the brass rod within the probe expands more with temperature increase than does the silver-plated glass tubing. For a parallel plate capacitor, capacitance is indirectly proportional to the distance between the plates. As the gap in the probe capacitor increases with increasing temperature, capacitance is expected to decrease, resonant frequency (or probe signal) increase, and normalized frequency (or normalized probe signal) decrease. Apparently, the parallel plate capacitor model is inadequate because Chen observed a decrease in probe signal with increasing temperature when the probe was immersed in air. Similar tests recently completed have verified this result. For instance, a probe that was partially removed from a hot, steam-saturated core for 3 minutes, provided a signal that was 0.6 mv larger than the signal from the probe when fully inserted into the core. As Chen concluded, the effect of temperature on the probe geometry compensates, in some as-yet-undefined way, for the effect of temperature on the dielectric constant of water.

Although the normalized probe signal appears to be independent of temperature, the use of the calibration curve requires some care. The main use of the probe is in nonisothermal, two-phase flow experiments.

Because water saturation determinations are required through a region of changing temperature, the 100% water-saturated (Φ_w) and steam-saturated (Φ_s) probe signals should be determined as a function of temperature so that Φ^* can be calculated properly for the probe signal at each temperature.

Using Φ_w and Φ_s values determined at the higher temperature of the injected, compressed water will cause an unpredictable error in the calculated normalized probe signal. Φ_w will tend to increase with increasing temperature due to the lowering of the dielectric constant of water, and Φ_w will tend to decrease with increasing temperature due to the thermal expansion character of the probe. These effects should be measured, not estimated. It is expected that Φ_s will only decrease with increasing temperature due to probe expansion.

For the moment, assume that Φ_w has a negligible change for some temperature range and that Φ_s increases by 1.0 mv with decreasing temperature. The assumption of a Φ_s value at the high inlet temperature (it is convenient to deplete the core at the end of the experiment to get Φ_s at the air bath temperature) will cause Φ_s to be less than actual. This will cause the normalized probe signal, Φ^*, to be less than actual because $\Phi_s - \Phi$ will be percentage-wise reduced more than $\Phi_s - \Phi_w$. The net effect is to cause the apparent steam saturation to be larger than it actually is. Recall that this example is for the case of constant Φ_w.

Additional experiments indicated an average Φ_w of -86 mv at 298°F, and a Φ_w of -82 mv at 84°F for a particular zero and span setting. This surprising result indicates that the probe signal decreases with increasing temperature rather than increasing as forecast. It is not understood why this occurs. At about 330°F, Φ_s = -69 mv.

The next section describes the effect that steam-water vertical separation may have on probe response.

6.1.3 Effect of Gravity Segregation on Probe Response

The effect of gravity segregation on the steam-water calibration curves is not known. If significant effects do occur, the following errors would probably result: **(1)** if the steam-water "interface" is far enough above the core centerline that the probe does not detect steam, then the normalized probe signal, Φ^*, will be larger than it would be for a homogeneous steam-water saturated medium at large water saturation values, and (2) if the steam-water "interface" is far enough below the core centerline that the probe does not detect liquid water, then the normalized probe signal, Φ^*, will be smaller than it would be for a homogeneous steam-water saturated medium at low S_w values. A proper analysis of the fluid distribution effects must include the effect of changing dielectric interfaces on the probe field; it is beyond the scope of this study.

The final comments concerning this study of the capacitance probe present recommendations for further study.

6.1.4 Future Improvements

This section presents guidelines for further study of the capacitance probe. In general, the Baker-type capacitance probe appears to work well. However, at times, stability is poor, resulting in a low confidence level in the water saturation data. The electronic circuit design is fairly simple, and perhaps can be modified to improve stability.

Using the calibration curves, probe response correctly represents water saturation to ±5-10% of pore volume. The lack of reproducibility is

highest in the 70-100% water saturation range. An analytic or numerical study of the effect of core holder metal parts, fluid distributions, and other dielectric interfaces on the probe field and probe response may lead to a better understanding of the shape of the calibration curve.

More effort should also be directed toward understanding the effect of temperature on probe response. Calibration curves should be developed for brine-steam mixtures.

This concludes the section on the capacitance probe. We now turn to the nonisothermal, steady, steam-water flow experiments in which the saturation probe was used.

6.2 Nonisothermal, Steady, Boiling Flow Experiments

This section presents data for three steady, nonisothermal, boiling flow experiments. Three different synthetic sandstone cores were used. The experiments were performed in a manner similar to that of Arihara (1974) and Chen (1976), as discussed in Sections 3, 4, and 5.

Compressed water was injected through the consolidated core. The outlet end pressure was maintained at a level such that boiling occurred within the core. The measured temperatures, pressures, probe signals, and flow rate data are presented in Appendix A3.2.

The following presents the method of interpretation, as well as the determination of axial thermal conductivity, overall heat transfer coefficient, and water saturation. Then the results of the three runs are discussed. The three runs presented in this section are representative of the many runs made in this investigation.

6.2.1 Method of Calculation

Arihara (1974) and Chen (1976) chose to assume that their flow data was not influenced by axial heat conduction or by radial heat transfer from the environment to the core. The assumption of an adiabatic process resulted in the isenthalpic, steady flow equations for drainage process relative permeability:

$$k_g/K = \frac{fw(\bar{uv})}{AK\left[-\frac{dp}{dx}\right]} \tag{6-8}$$

$$k_\ell/K = \frac{(1-f)w(\bar{uv})_\ell}{AK\left[-\frac{dp}{dx}\right]} \tag{6-9}$$

$$f = \frac{h-h_\ell}{h_{\ell g}} = \frac{w_g}{w} \tag{6-10}$$

where:

k = effective permeability, md

K = absolute permeability, md

f = flowing mass fraction of gas

μ = viscosity

h = enthalpy, Btu/lb

$\bar{v}$ = specific volume, ft^3/lb

$w = w_g + w_\ell$ = total weight rate of flow, lb/hr

p = pressure, psi

x = linear, horizontal distance, in

A = core cross-sectional area, ft^2

Subscripts: R = liquid (liquid water)

g = gas (water vapor)

Rg = liquid to vapor

The adiabatic flow assumption is inadequate for the low flow rates used in this study. Isenthalpic flow does not allow the development of a large vapor saturation. The required steady, non-adiabatic (or non-isenthalpic) flow equations follow:

$$\left(\frac{dq_H}{dx}\right)_{\substack{\text{forced}\\\text{convection}}} + \left(\frac{dq_H}{dx}\right)_{\substack{\text{axial}\\\text{conduction}}} + \left(\frac{dq_H}{dx}\right)_{\substack{\text{radial}\\\text{heat}\\\text{transfer}}} = 0 \qquad (6-11)$$

$$dx\left[(wh)_\ell + (wh)_g\right] + \frac{d}{dx}\left[-\lambda A\left(\frac{dT}{dx}\right)\right] + PU(T_\infty - T) = 0 \qquad (6-12)$$

Integrating along the length of the core from zero to x, assuming compressed water of enthalpy h is injected at the inlet end at weight rate w, and solving for the flowing gas mass fraction f:

$$f = \frac{h-h_\ell}{h_{\ell g}} - \frac{\lambda A\left[\left(\frac{dT}{dx}\right)_0 - \left(\frac{dT}{dx}\right)_L\right]}{wh_{\ell g}} + \frac{PU\int_0^L (T_\infty - T)dx}{wh_{\ell g}} \qquad (6-13)$$

where:

X = axial thermal conductivity, Btu/(hr-ft-°F)

U = overall heat transfer coefficient, Btu/(hr-ft^2-°F)

T = axial core temperature, °F

T_∞ = air bath temperature, °F

P = core perimeter, ft

A = core cross-sectional area, ft^2

q_H = heat flow rate, Btu/hr

The absolute permeability, **K**, is the 100% water-saturated core permeability determined from a separate flow test. Viscosity, specific volume, enthalpy, and pressure gradient can be obtained in the two-phase region from the measured temperature profile. It is assumed that there is no vapor pressure lowering and no capillary pressure effect.

The elimination of a major assumption, adiabatic flow, has created the need for several lesser assumptions to describe the axial and radial heat transfer. The axial heat transfer is discussed in the next section.

6.2.2 Axial Thermal Conductivity

Heat conduction along the length of the core can be calculated using Fourier's law. **An** axial thermal conductivity of $\lambda = 1$ Btu/(hr-ft-°F) was used in this study. No data is available for the thermal conductivity of flowing two-phase systems. Adivarahan, Kunii, and Smith (1962) presented data for the countercurrent flow of single-phase fluid and heat. They concluded that thermal conductivity was rate dependent. However, analysis of the Adivarahan (1961) data by the present author indicated that a radial heat gain (or loss) term was neglected. Inclusion of this heat transfer term can eliminate most of the supposed rate dependency.

Use of the Anand, Somerton, and Gomaa (1972) correlations indicated $\lambda = 0.3$ Btu/(hr-ft-°F) for a dry rock, and $\lambda = 0.9$ Btu/(hr-ft-°F) for a water-saturated rock with $\phi = 0.35$, $K = 30$ md, and $T = 250$°F.

Because (1) many rocks demonstrate a thermal conductivity larger than 0.9 Btu/(hr-ft-°F) and (2) the correlations used were based on rocks of lower porosity and higher permeability than the synthetic cores used in the present study, it was decided that $\lambda = 1$ Btu/(hr-ft-°F) was a reasonable value to use. The thermal conductivity was assumed constant, although it may vary with water saturation.

The following section discusses the selection of the core holder overall heat transfer coefficient.

6.2.3 Overall Heat Transfer Coefficient

The radial heat gain to the horizontal, cylindrical core can be characterized using Fourier's law and an overall heat transfer coefficient. The overall heat transfer coefficient, **U**, for the core holder was discussed in detail by Arihara *(1974).* Overall heat transfer coefficients determined by Arihara for a core holder similar to the one used in this study is shown in Fig. 6-5. For the single-phase flow of hot water in a cold core, the overall heat transfer coefficient was lower, and a stronger function of flow rate than for the case of cold water injection into a hot core. The differences between the two cases is a result of the increased film coefficient caused by the use of a fan in the high temperature air bath runs. No fan was used in the room temperature air bath runs. At the low flow rates of **0.1** - 0.2 lb/hr, the hot air bath curve extrapolates down to roughly **U** = 2 Btu/(hr-ft^2-°F).

The overall heat transfer coefficients obtained early in this study are also shown in Fig. 6-5. The heat transfer coefficients are larger than those obtained by Arihara because of the different core holder - hot air film coefficient. This film coefficient was different because the present fan: **(1)** is located in a different position than for Arihara's runs, (2) has a more powerful motor, and (3) can be controlled with adjustable louvers. At low flow rates (0.2 lb/hr), a value of U = 3 Btu/(hr-ft^2-°F) is expected using the same slope as Arihara's cold water, hot air bath curve.

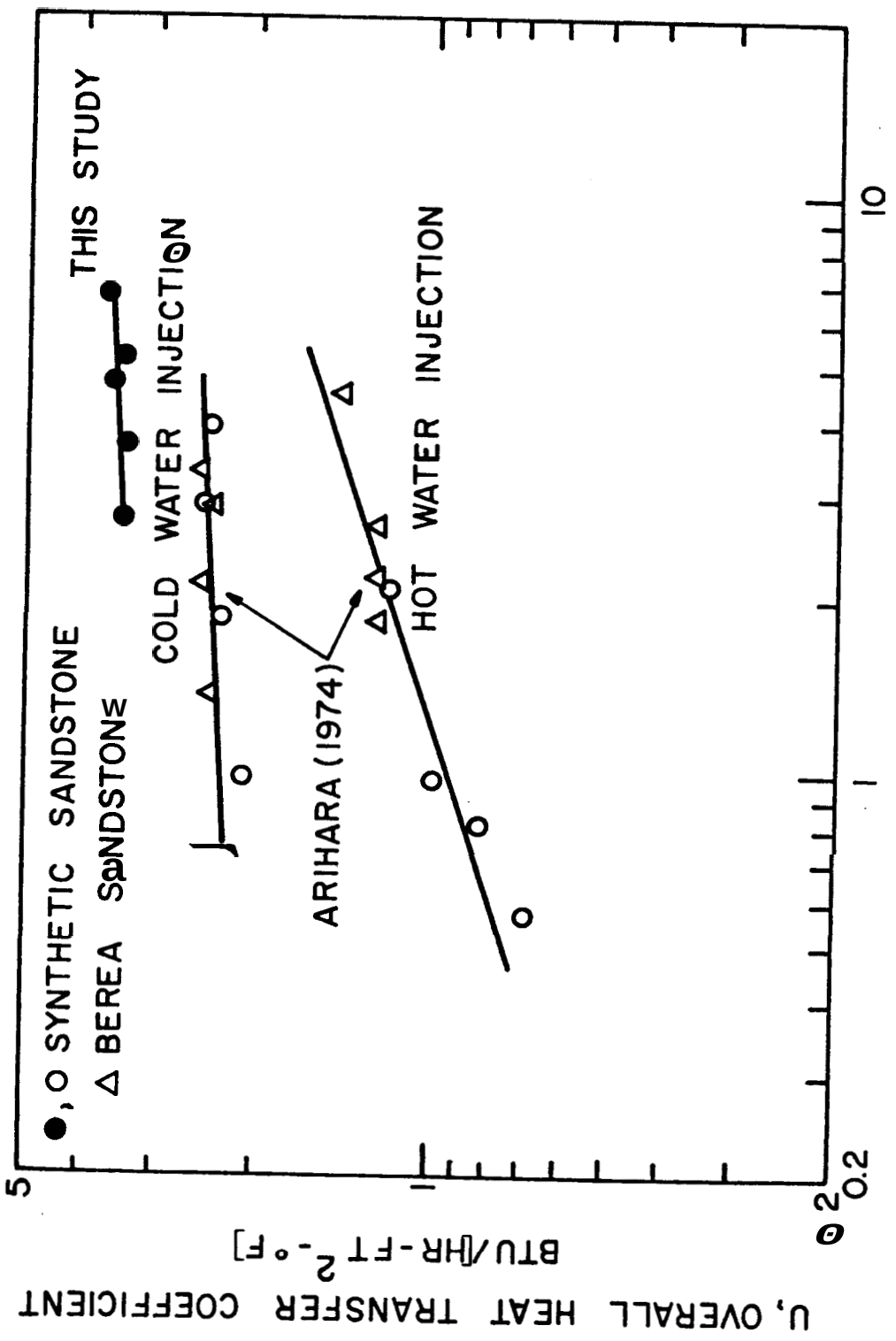

FIG. 6-5: OVERALL HEAT TRANSFER COEFFICIENT VS MASS INJECTION RATE

Heat transfer coefficients in this study were determined from an energy balance using the temperature profile and mass flow rate:

$$U = \frac{-w(h-h_{\ell}) + AX\left[\left(\frac{dT}{dx}\right)_0 - \left(\frac{dT}{dx}\right)_L\right]}{P\int_0^L (T_{\infty}-T)\,dx} \qquad (6-14)$$

The axial thermal conduction term is often negligible for these single phase experiments because the inlet and outlet temperature gradients are similar. Heat transfer coefficient variation along the length of the core can be detected with Eq. *6-14* by using the equation for the core holder segment of interest.

The value of the overall coefficient was assumed constant, although the brass end plugs and end caps may have caused variations near the core holder ends. Also, air flow around the core holder was probably not uniform.

Since the heat transfer coefficients obtained in the single-phase tests may be larger than actual coefficients in a two-phase fluid due to different core-silicone rubber sleeve film coefficients, a value of **U** = 2 Btu/(hr-ft^2-°F) was used in this study. Louvers, which direct air flow across the core holder, were also arranged to provide a low air flow, thus lowering the core holder film coefficient.

In addition to the overall heat transfer coefficient data discussed earlier, Arihara *(1974)* also obtained values for condensing steam injection in a cold air bath. Arihara found that for steam injection rates of **0.10** to 0.15 lb/hr, the overall heat transfer coefficient varied from ***1.4*** to *1.6* Btu/(hr-ft^2-°F).

6.2.4 Water Saturation Measurement

The large scatter in the water saturation measurements represents one of the major problems encountered in this study. One of the undesirable characteristics of the capacitance probe noted in the calibration study was the large data scatter present at high water saturations. Since: **(1)** the liquid water dielectric constant is much greater than the sand or water vapor dielectric constant, and *(2)* the sand and water vapor dielectric constants are much closer in magnitude than the sand and liquid water constants, this saturation data scatter is much greater at high liquid water saturations than at very low liquid water saturations.

It was found to be easier to smooth the normalized probe signal data before obtaining the water saturation profile. Due to the shape of the probe signal - liquid water saturation curve, Fig. *6-2,* more data scatter is induced by graphing the water saturation obtained from each normalized probe signal data point.

We turn now to consideration of the results obtained from the nonisothermal boiling runs.

6.2.5 Run SW1

This section presents the results of the medium flow rate, boiling flow run. Compressed water was injected into the inlet end of the *26* md core at a rate of *0.212* lb/hr. Confining pressure was applied to a silicone rubber sleeve. The temperature, normalized probe signal, and water saturation profiles are presented in Figs. *6-6,* 6-7, and *6-8.*

In this experiment, there was some uncertainty in the inlet pressure measurement. It is possible that a two-phase mixture was injected rather than single-phase compressed water.

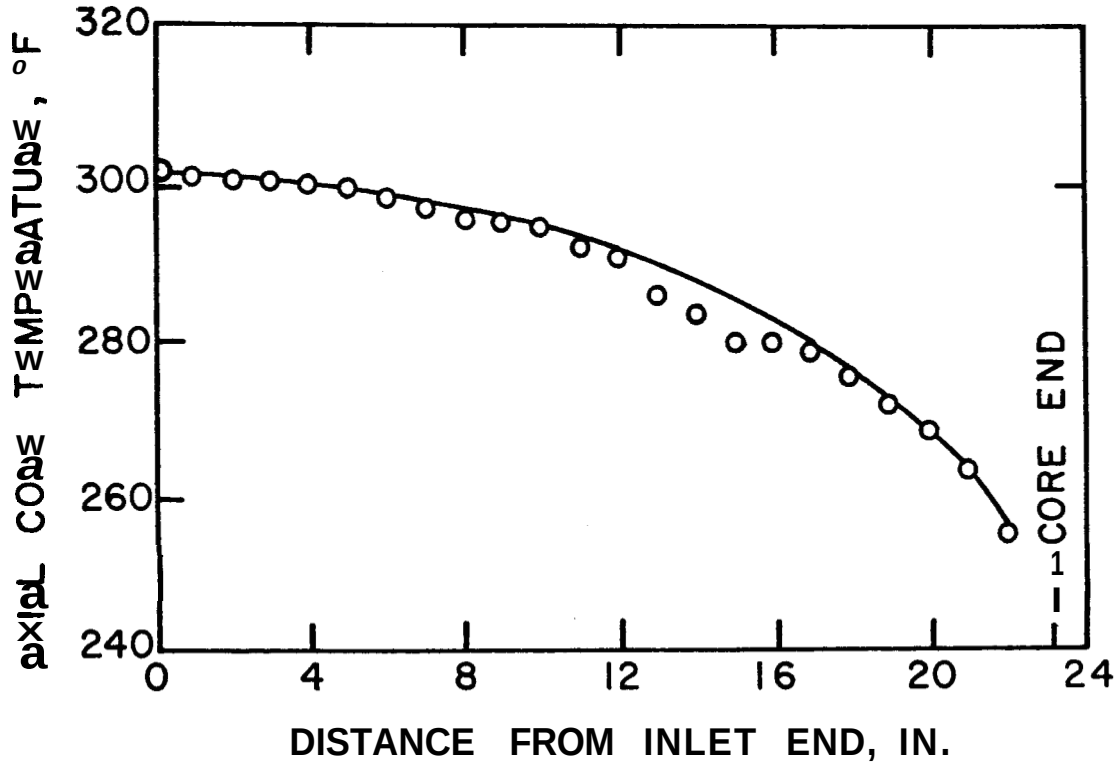

FIG. 6-6: TEMPERATURE VS DISTANCE, RUN SW1

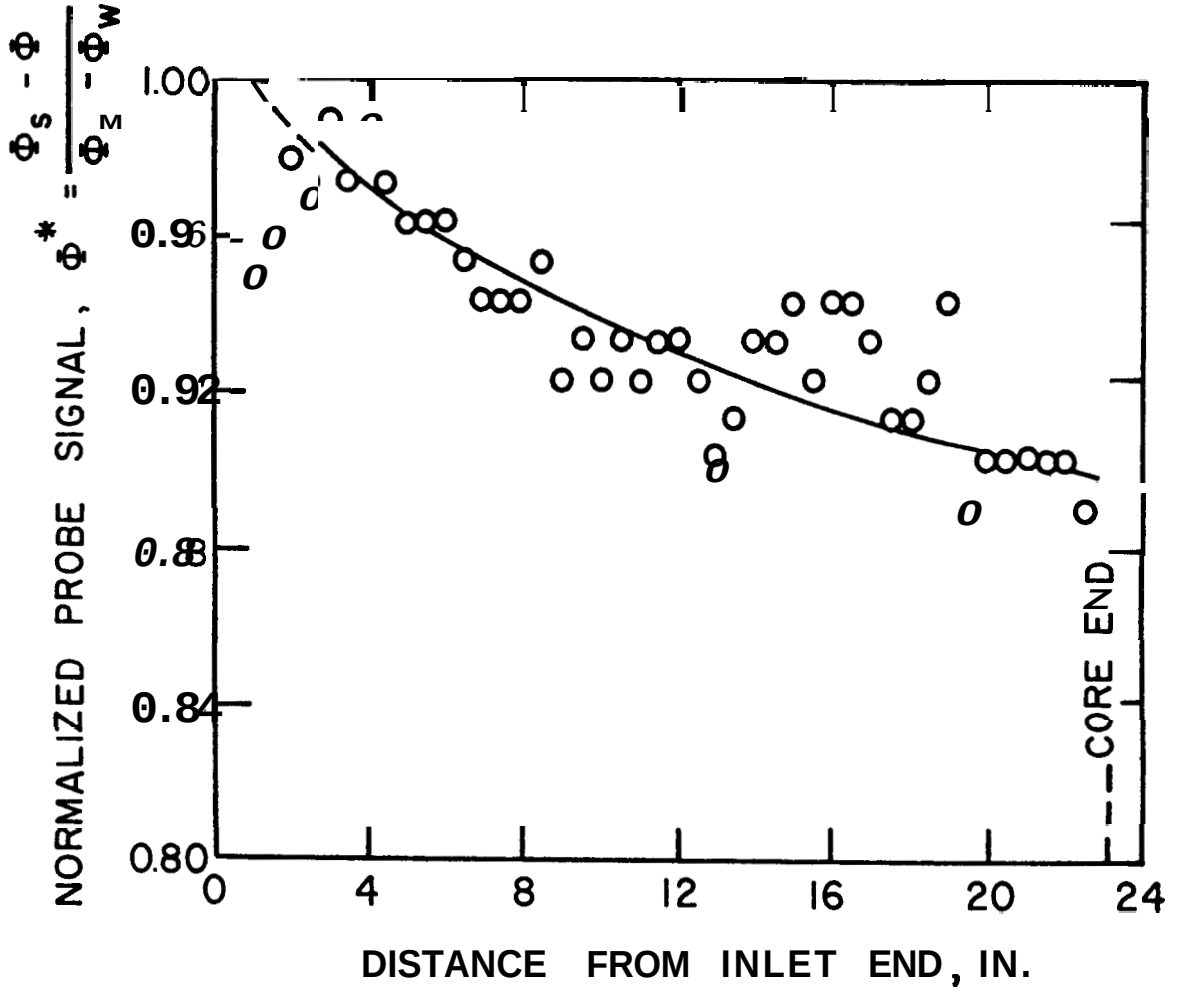

FIG. 6-7: NORMALIZED PROBE SIGNAL VS DISTANCE, RUN SW1

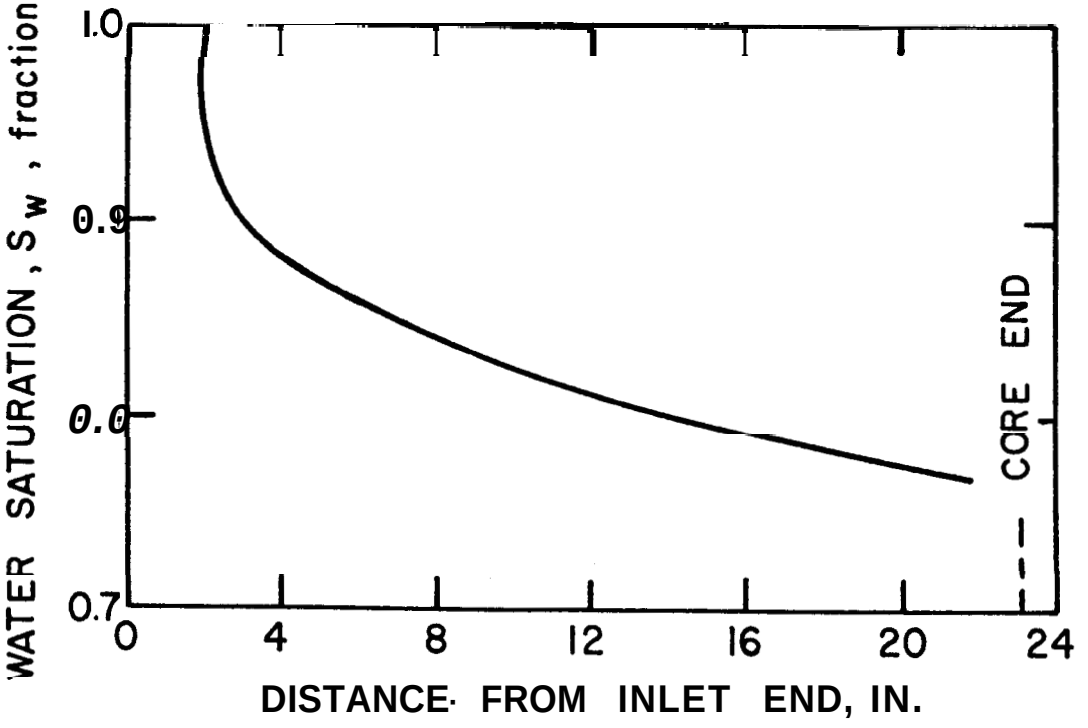

FIG. 6-8: WATER SATURATION VS DISTANCE, RUN SW1

The calculation of flowing gas mass fraction in Table 6-1 demonstrates that radial heat gain near the outlet end of the core dominated the formation of vapor. The steam-water calculations are presented in Table 6-2, and the relative permeability curves are shown in Fig. 6-9. Both the steam and liquid water curves are steep and cover only a narrow range of water saturation.

6.2.6 Run SW2

The results for a low injection rate run are presented in this section. Compressed water was injected into the inlet end of the 34 md core at a rate of 0.106 lb/hr. Confining pressure was applied to an ethylene propylene sleeve. The temperature, normalized probe signal, and water saturation profiles are presented in Figs. **6-10,** 6-11, and 6-12.

A crack in the core, perpendicular to flow, had no apparent effect on steam-water flow. The crack was located 7.5 inches **from** the inlet end of the core. The temperature profile demonstrates that flow rate was so low that a dry region of higher temperature developed near the outlet end of the core. Pressures were estimated in this region by extrapolation from the two-phase region to the measured outlet pressure. The ambient air bath temperature exceeded the inlet fluid temperature, thus contributing to vaporization.

The calculated flowing gas mass fraction in Table 6-3 demonstrates that radial heat gain from the environment dominated the formation of vapor. The values of overall heat transfer coefficient and axial thermal conductivity discussed earlier gives reasonable results and helps support the use of $\lambda = 1$ Btu/(hr-ft-°F) and $U = 2$ Btu/(hr-ft^2-°F).

TABLE 6-1: RUN SW1 CALCULATIONS FOR FLOWING GAS MASS FRACTION

x in	T_{core} °F	$(-\frac{dT}{dx})$ °F/ft	$xT_\infty - \int_o^x T dx$ °F-ft	h_ℓ Btu/lb	h_{fg} Btu/lb	1 $\frac{h-h_\ell}{h_g-h_\ell}$	2 $\frac{-A\lambda(\frac{dT}{dx})}{w(h_g-h_\ell)}$	3 $\frac{PU\int_o^x (T_\infty - T)dx}{w(h_g-h_\ell)}$	f = 1 - 2 + 3 Mass Fraction
0	302	0	0	271 8	908 5	0	0	0	0
2	301	5 50	-0 003	270 8	909 2	$1\ 10\times10^{-3}$	611×10^{-3}	$-\ 0163\times10^{-3}$	0 000573
4	300	7 20	133	269 7	910 0	$2\ 31\times10^{-3}$	810×10^{-3}	721×10^{-3}	0 00272
6	298	12 6	300	267 7	911 5	$5\ 50\times10^{-3}$	$1\ 52\times10^{-3}$	$1\ 62\times10^{-3}$	0 00570
8	296	14.4	.867	265.6	913.0	6.79×10^{-3}	1.62×10^{-3}	4.69×10^{-3}	0.00986
10	294	18 0	1 83	263 5	914 5	$9\ 08\times10^{-3}$	$2\ 02\times10^{-3}$	$9\ 89\times10^{-3}$	0.0170
12	291	26.4	3.40	260.5	916.7	12.3×10^{-3}	2.96×10^{-3}	18.3×10^{-3}	0.0276
14	283	30 0	5 77	252 2	922 5	$21\ 2\times10^{-3}$	$3\ 34\times10^{-3}$	$30\ 9\times10^{-3}$	0 0488
16	279	31.8	9.23	248.1	925.3	25.6×10^{-3}	$3\ 53\times10^{-3}$	$43\ 2\times10^{-3}$	0 0713
18	275	38 4	13 1	244 1	928 2	$29\ 8\times10^{-3}$	$4\ 25\times10^{-3}$	$69\ 7\times10^{-3}$	0 0953
20	268	55 2	18 1	23 9	933 1	$37\ 4\times10^{-3}$	6.08×10^{-3}	95.8×10^{-3}	0.127
22	255	97.3	24 6	232 7	942 1	$51\ 1\times10^{-3}$	10.6×10^{-3}	129×10^{-3}	0.170

T_o = 302°F
w = 0.212 lb/hr
h_{in} = 271.8 Btu/lb
A = 0.0218 ft^2

λ = 1 Btu/(hr-ft-°F)
U = 2 Btu/(hr-ft^2-°F)
P = 0 523 ft

TABLE 6-2: RUN SW1: CALCULATIONS FOR STEAM-WATER RELATIVE PERMEABILITY

x	(-dp/dx)	f	μ_s	μ_w	$\bar{v}_s$	$\bar{v}_w$			
in	psi/in	Mass Fraction	cp	cp	ft^3/lb	ft^3/lb	k_s/K^{**}	k_ω/K^{***}	S_w
0	0 371*	0	0 0140	0 180	⊇ 287	0 017⊂7	0	1 00	1 00
2	0 440	0 000⊂73	0 01⊂0	0 181	⊇ ∃77	0 017⊂6	0 011∃	0 8⊂7	0 97
4	0 690	0 00Z22	0 01⊂0	0 182	⊇ ⊂66	0 01745	0 034⊂	0 5⊂Z	0 88
6	1 03	0 0⊇470	0 01∃9	⊇ 18∃	⊇ ⊇5Z	0 0174∃	0 0498	0 ∃64	0 8⊇
8	1 ∃0	0 0098⊇	0 0139	0 185	6 8⊂⊂	0 01741	0 0851	0 289	0 85
10	1 55	0 0170	0 0139	0 187	7 0⊂Z	0 017∃9	0 127	0 243	0 8∃
12	1 73	0 0276	0 01∃8	0 1⊇9	7 ∃5⊂	0 01737	0 1∃1	0 218	0 81
1⊂	1 87	0 0⊂⊇8	0 01∃⊇	0 19⊇	8 Z67	0 01729	0 ∃46	0 Z03	0 ∃0
1⊇	2 03	0 071∃	⊇0135	0 199	8 775	0 017Z⊇	0 491	0 185	0 79
18	2 29	0 095∃	0.01∃4	0 20∃	9 3Z0	0 017Z2	0 ⊇1∃	0 1⊇∃	0 78
Z0	2 9⊂	0 1Z7	0 01∃∃	0 Z10	10 38	0 01716	0 70⊂	0 1Z⊇	0 77
22	3 96	0 170	0.0130	0 Z2∃	12 7⊂	0 0170⊂	0 839	0 09 0	0 77

* dp/dx assumed equal to 100% water flowing pressure gradient

** $k_s/K = \dfrac{118\ f(\mu\bar{v})_s}{(-dp/dx)}$

*** $k_w/K = \dfrac{118(1-f)(\mu\bar{v})_w}{(-dp/dx)}$

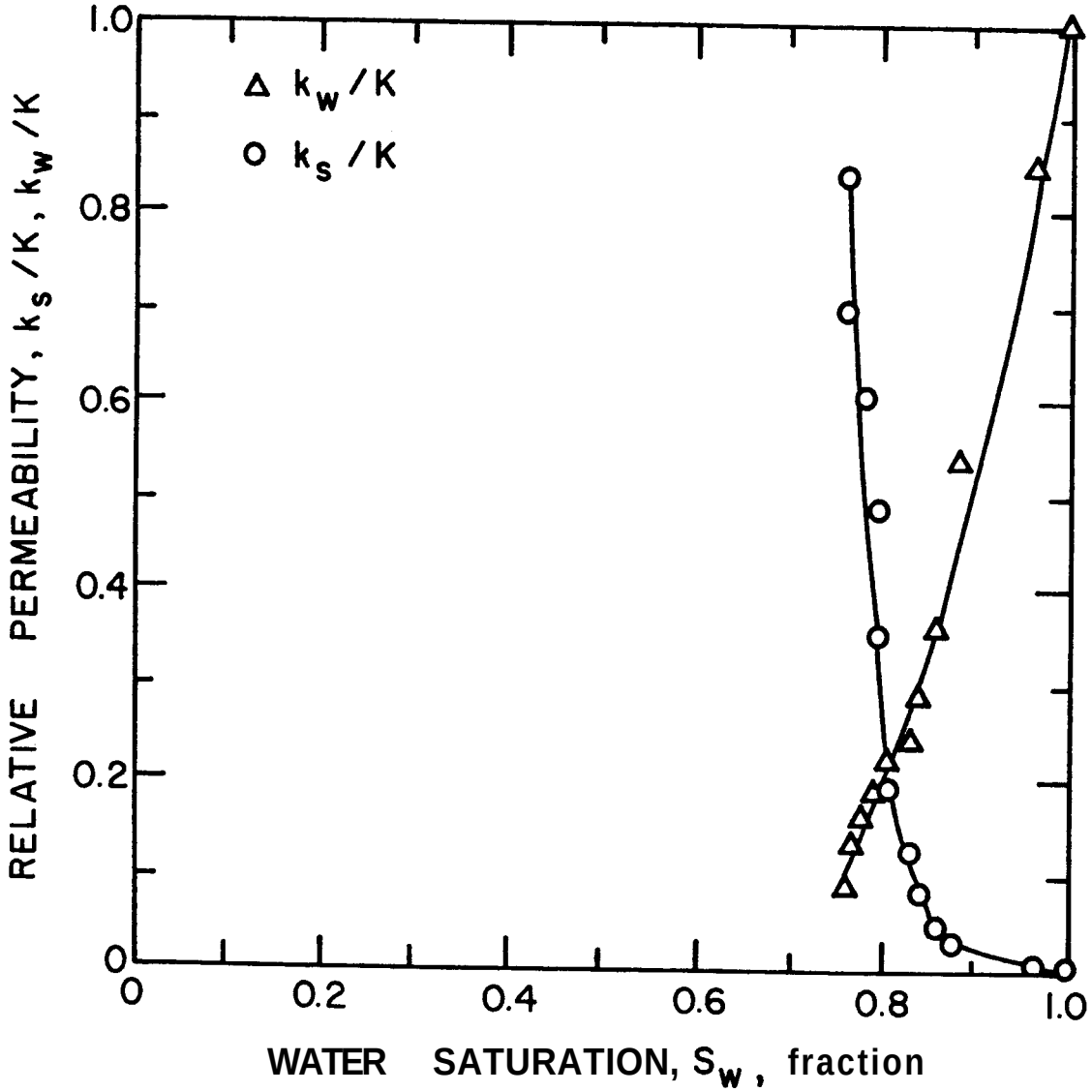

FIG. 6-9: STEAM-WATER RELATIVE PERMEABILITY VS WATER SATURATION FOR MEDIUM FLOW RATE, RUN SW1

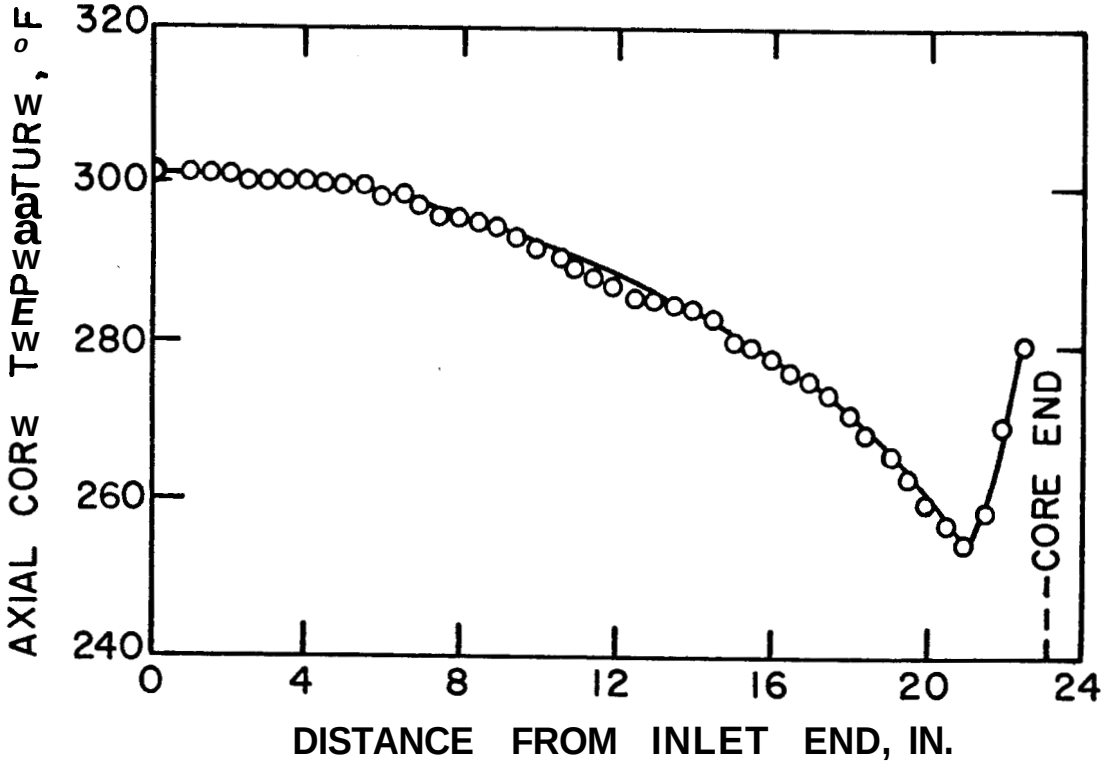

FIG. 6-10: TEMPERATURE PROFILE VS DISTANCE, RUN SW2

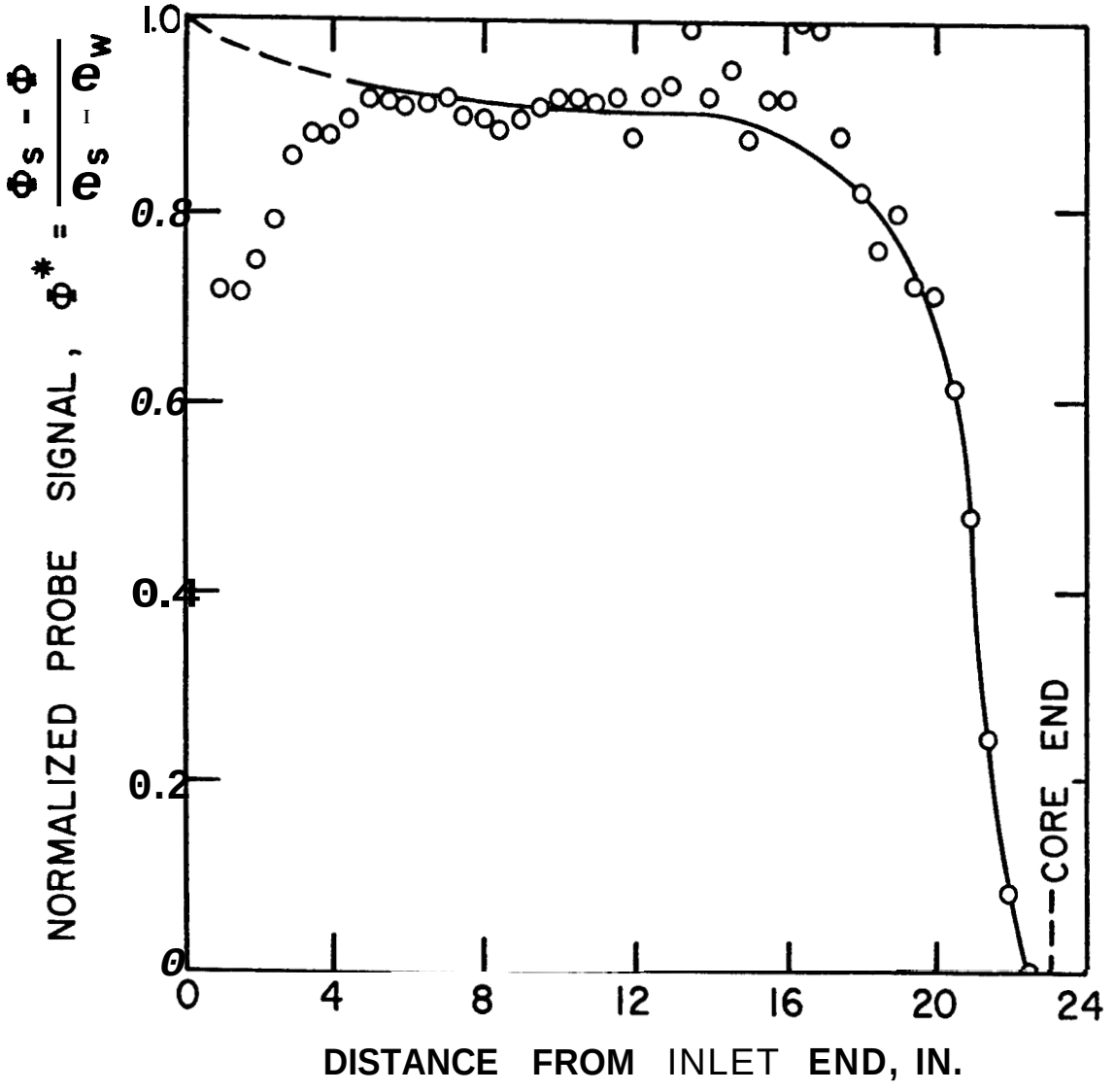

FIG. 6-11: NORMALIZED PROBE SIGNAL VS DISTANCE, RUN SW2

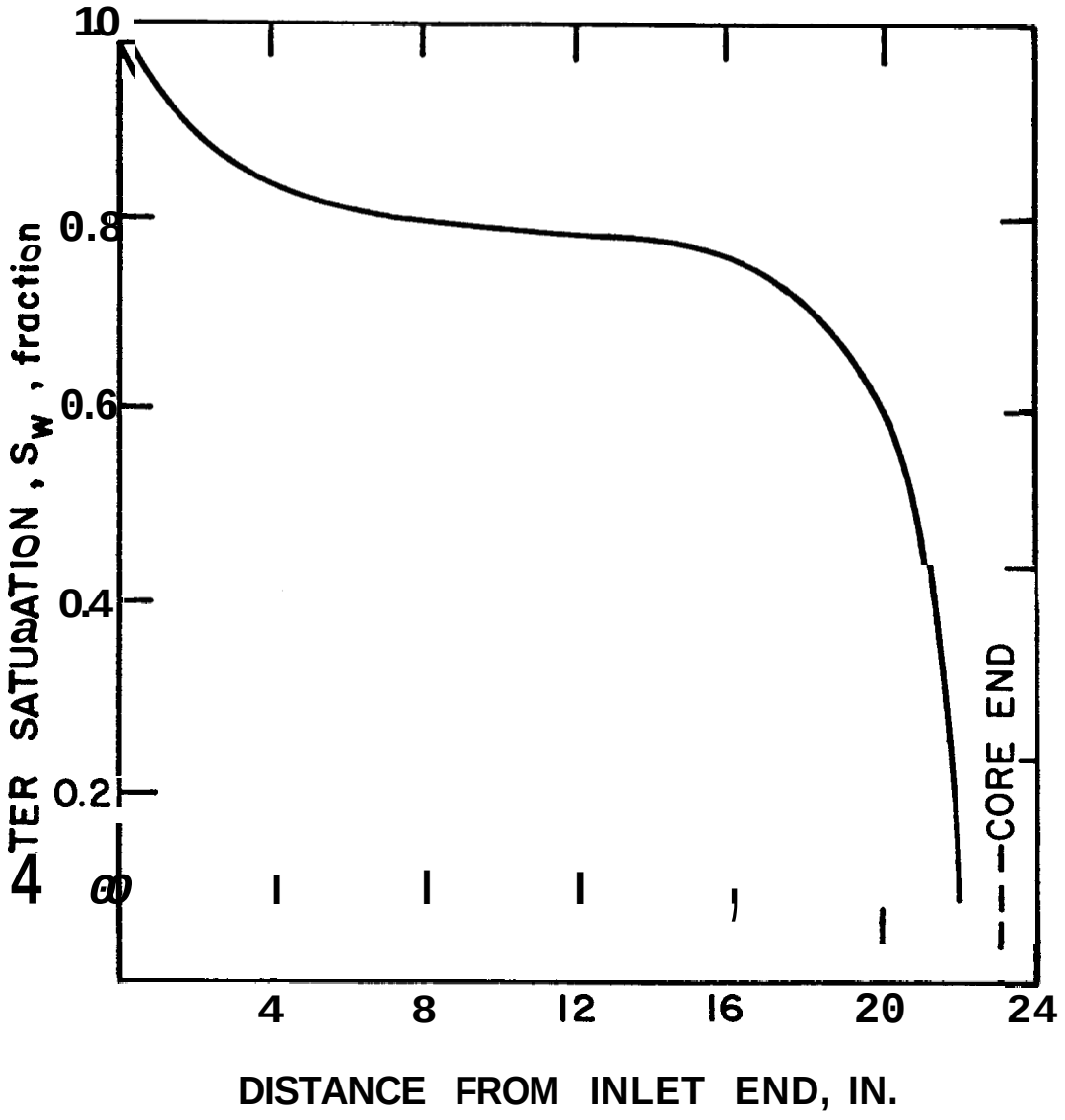

FIG. 6-12: WATER SATURATION VS DISTANCE, RUN SW2

TABLE 9-3: RUN SW2 CALCULATIONS FOR FLOWING GAS MASS FRACTION

x in	T_{core} °F	(-dT/dx) °F/ft	$xT_\infty - \int_0^x T\,dx$ °F-ft	h_ℓ Btu/lb	h_{fg} Btu/lb	1: $\frac{h-h_\ell}{h_g-h_\ell}$	2: $\frac{-A\lambda(dT/dx)_x}{w(h_g-h_\ell)}$	3: $\frac{P\omega \int_0^x (T_\infty - T)\,dx}{w(h_g-h_\ell)}$	f = 1 - 2 + 3 Mass Fraction
0	30Z	0	0	Z71 8	90≤ 5	0	0	0	0
2	302		Z 25	271 8	908 5	0	0	2C C×10^{-3}	0 0ZCC
C	301	9.00	C 70	Z+0 8	909 2	1 10×10^{-3}	2.04x10^{-3}	43 4×10^{-3}	0 0425
6	298	15.0	7.20	267.7	911.5	4.50x10^{-3}	3.38x10^{-3}	77.9x10^{-3}	0 0790
8	296	19.9	10 10	2 5 6	≡13 0	6 79×10^{-3}	4 48x10$^{-\equiv}$	109x10^{-3}	0 111
10	29Z	2C.0	13	261	915.9	11 2×10^{-3}	5 39x10$^{-\equiv}$	145x10^{-3}	0 151
12	287	25.2	17.8	256.3	919.6	16.9x10^{-3}	5 64x10$^{-\equiv}$	191x10^{-3}	0 202
1C	Z8C	Z8 8	22 7	253 3	9Z1 7	20 1×10^{-3}	6 43x10^{-3}	2C3x10^{-3}	0 257
16	278	35.4	28.4	247.1	926.0	26.7x10^{-3}	7 86x10^{-3}	303x10^{-3}	0 322
18	271	52 8	35 1	2C0 0	931.0	3C 2×10^{-3}	11.7x10^{-3}	372x10^{-3}	0 ≡95
20	259	69.6	C3 5	227 7	939 3	C9.9×10^{-3}	15.2x10^{-3}	457x10^{-3}	0 C89
Z1	Z5C	9 6	C7.9	Z2Z 7	9CZ +	5Z 1×10^{-3}	15 2×10^{-3}	501x10^{-3}	0 ≡38

T_∞ = 315°F
w = 0.106 lb/hr
h_{in} = 271.8 Btu/lb
A = 0.0218 ft^2

λ = 1 Btu/(hr-ft-°F)
U = 2 Btu/(hr-ft^2-°F)
P = 0.523 ft

The steam-water relative permeability calculations of Table 6-4 are graphed in Fig. 6-13. These curves show a wide range of steam-water relative permeabilities over a wide range of water saturations. The critical gas saturation appears to be nearly zero. We now turn to a third boiling flow experiment using a third core.

6.2.7 Run SW3

The results of a high injection rate run are presented in this section. Compressed water was injected into the inlet end of the 36 md core at a rate of *0.244* lb/hr. Confining pressure was applied to a silicone rubber sleeve. The temperature, normalized probe signal, and water saturation profiles are presented in Figs. *6-14,* 6-15, and 6-16.

The declining temperature along the first five or six inches of the core may be caused by the core temperature exceeding the ambient air bath temperature. The normalized probe signal curve was smoothed, considering that evaporative cooling does not start until 6 inches from the inlet end.

The flowing gas mass fraction calculations in Table 6-5 show that radial heat gain dominated the data to a lesser extent than in the lower injection rate runs, SW1 and SW2.

The calculated steam-water relative permeabilities are listed in Table 6-6. The relative permeability curve in Fig. 6-17 covers a very narrow steam relative permeability range. The apparent critical gas saturation is much higher for Run SW3 than for Run SW2.

The core used in this run was also used in the isothermal gas drive experiments discussed in Section 6.3. A comparison of the three steam-water runs is presented in the next section.

TABLE 6-4: RUN SW2 CALCULATIONS FOR STEAM-WATER RELATIVE PERMEABILITY

x in	(-dp/dx) psi/in	f Mass Fraction	μ_s cp	μ_w cp	$\bar{v}_s$ ft^3/lb	$\bar{v}_w$ ft^3/lb	k_s/K**	k_w/K***	S_w
0	0.142*	0	0.0140	0.180	6.4663	0.01747	0	1.00	1.00
2	0.900	0.0244	0.0140	0.180	6.2869	0.01747	0.108	0.154	0.88
4	0.900	0.0425	0.0140	0.181	6.3766	0.01746	0.190	0.152	0.83
6	1.15	0.0790	0.0139	0.183	6.6518	0.01743	0.287	0.115	0.81
8	1.55	0.111	0.0139	0.185	6.8438	0.01741	0.308	0.0834	0.80
10	1.75	0.151	0.0138	0.188	7.2481	0.01738	0.390	0.0716	0.79
12	2.05	0.202	0.0137	0.192	7.7944	0.01733	0.475	0.0585	0.78
14	2.20	0.257	0.0136	0.195	8.1460	0.01730	0.584	0.0514	0.78
16	2.85	0.322	0.0135	0.200	8.9077	0.01725	0.613	0.0370	0.76
18	3.30	0.395	0.0133	0.207	9.9069	0.01718	0.712	0.0294	0.71
20	3.95	0.489	0.0131	0.218	11.951	0.01708	0.875	0.0217	0.61
21	4.30	0.538	0.0130	0.224	12.949	0.01704	0.951	0.0185	0.47
22	4.65	0.652	0.0133	0.209	10.217	0.01717	0.860	0.0121	0.06****

* dp/dx assumed equal to 100% water flowing pressure gradient

** $$k_s/K = \frac{45.14 f (\mu\bar{v})_s}{(-dp/dx)}$$

*** $$k_w/K = \frac{45.14 (1-f) (\mu\bar{v})_w}{(-dp/dx)}$$

**** Not plotted in Fig. 6-13 because thermal end effect not properly modeled.

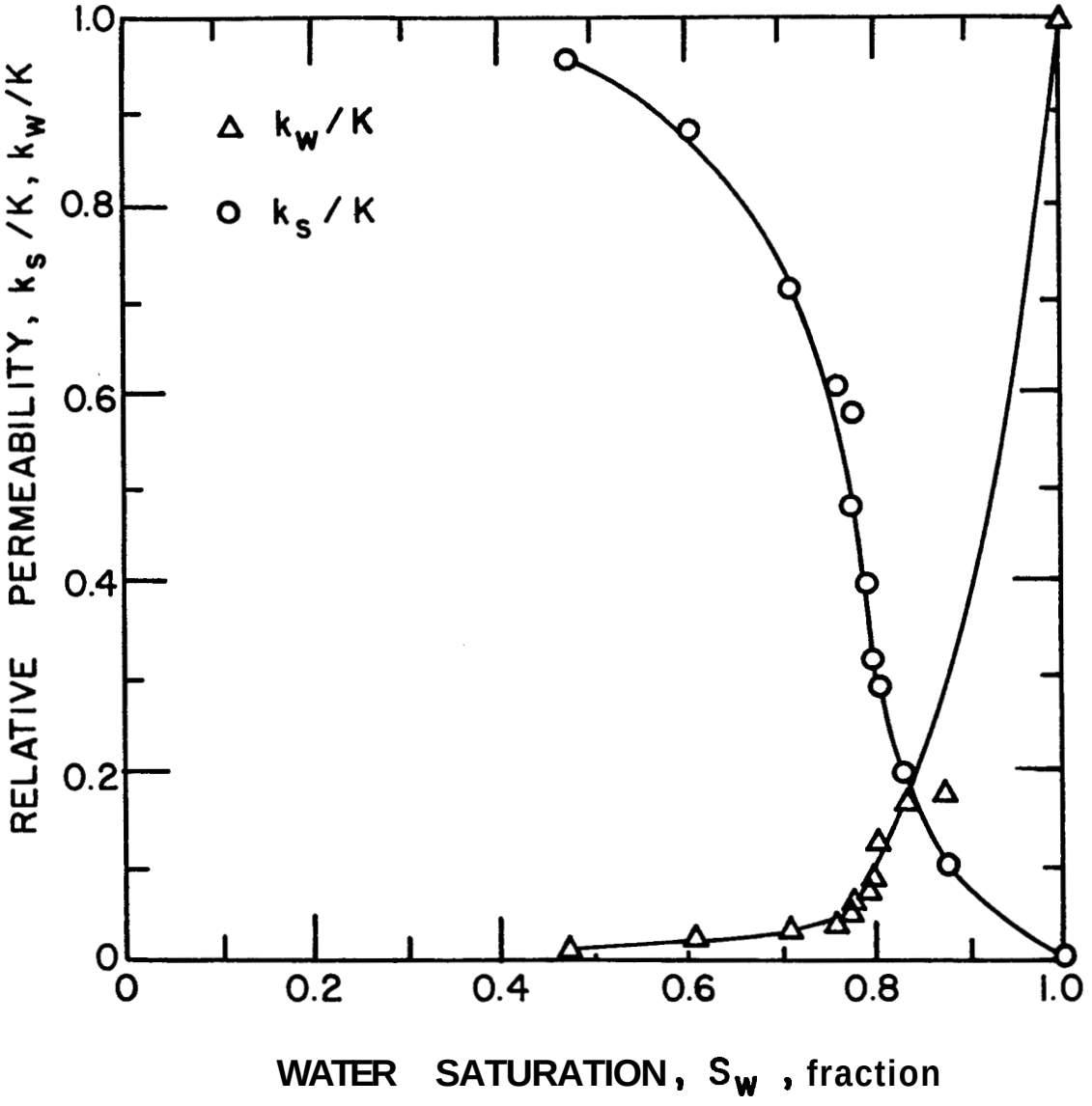

FIG. 6-13: STEAM-WATER RELATIVE PERMEABILITY VS WATER SATURATION FOR LOW FLOW RATE, RUN SW2

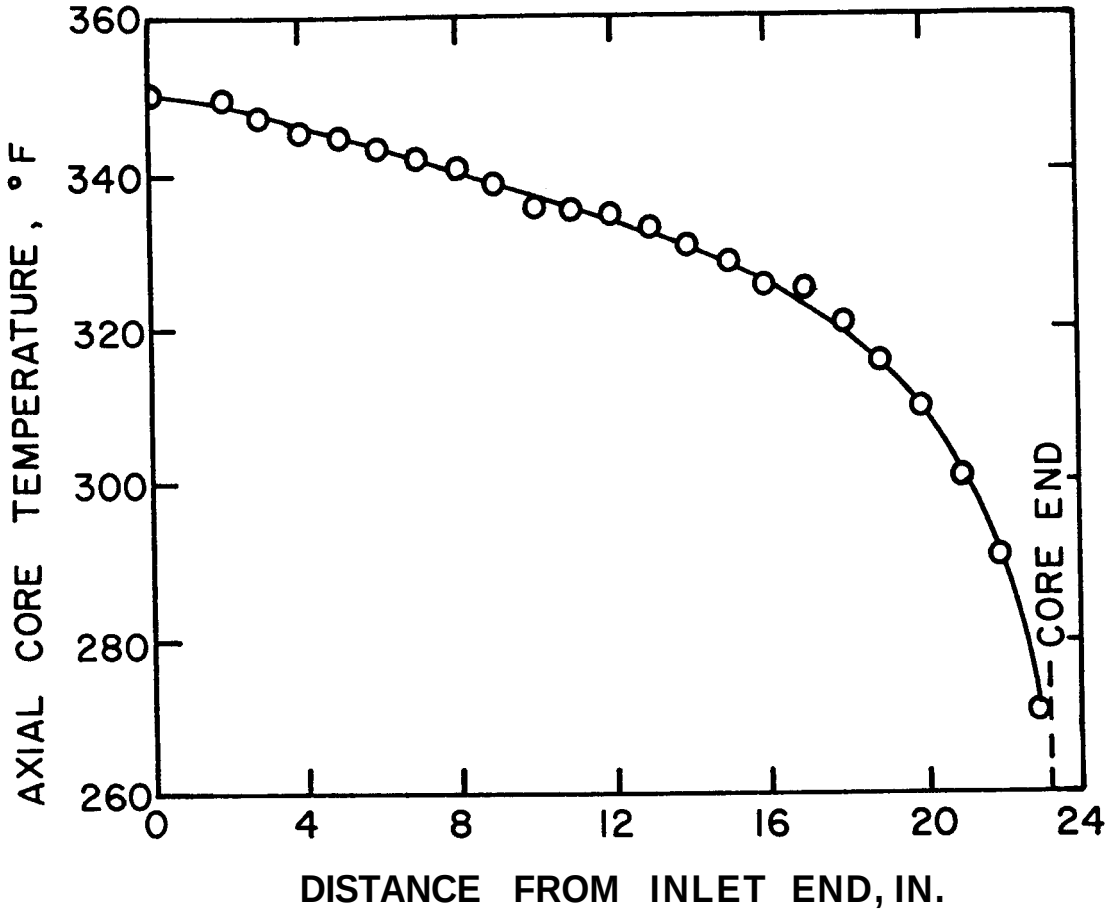

FIG. 6-14: TEMPERATURE VS DISTANCE, RUN **SW3**

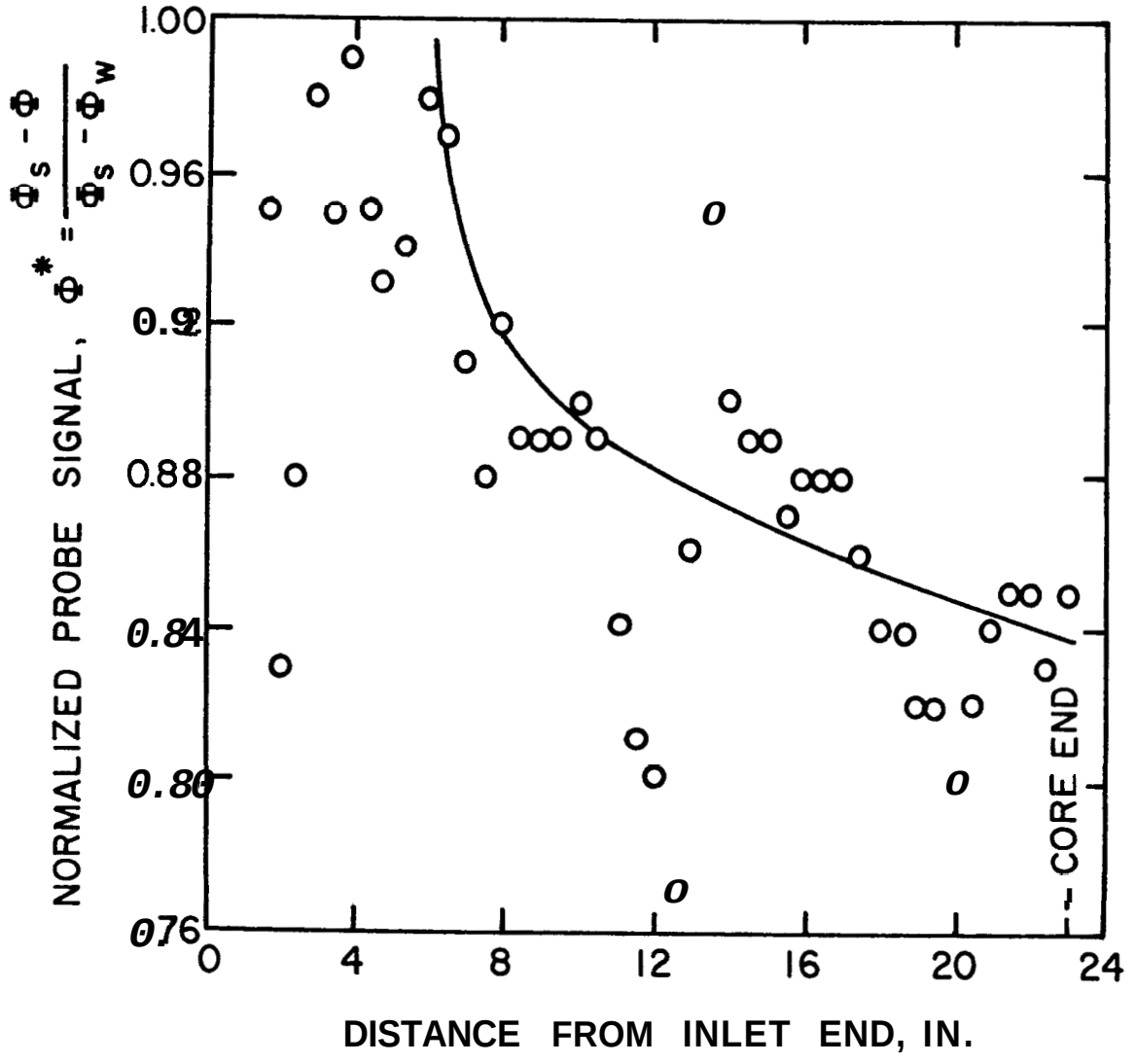

FIG, 6-15: NORMALIZED PROBE SIGNAL VS DISTANCE, RUN SW3

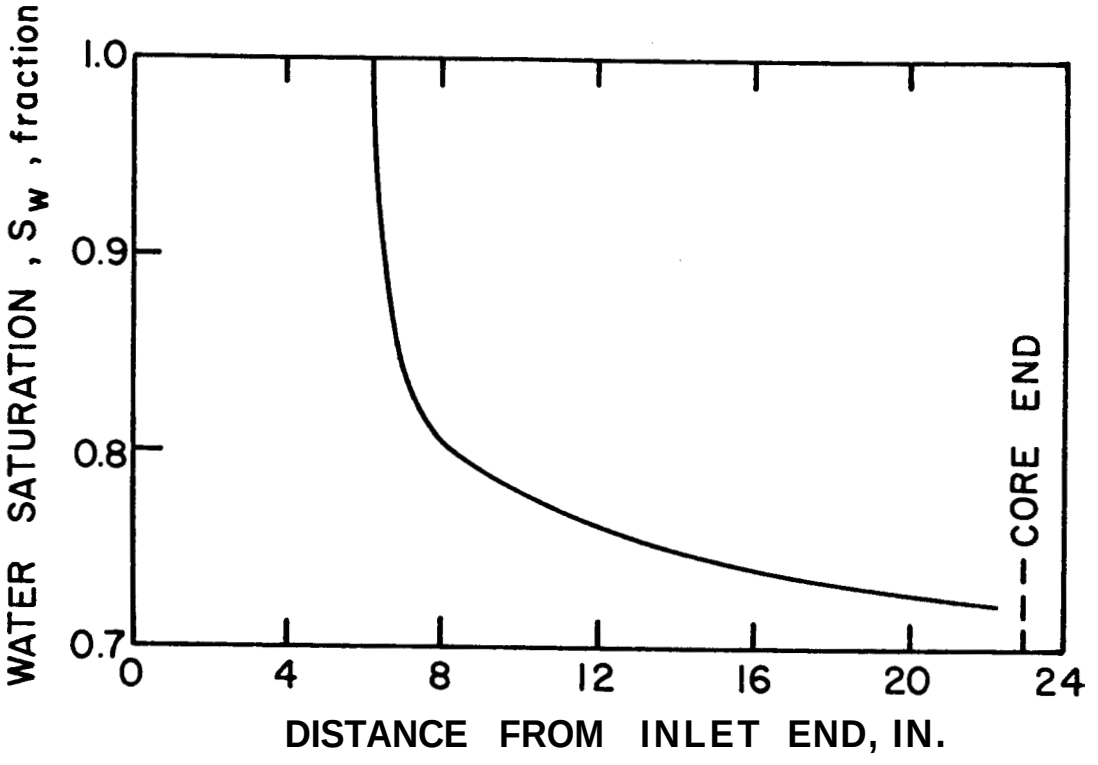

FIG, 6-16: WATER SATURATION VS DISTANCE, RUN SW3

TABLE 6-5: RUN SW3 CALCULATIONS FOR FLOWING GAS MASS FRACTION

x in	T_{core} °F	(-dT/dx) °F/ft	$xT_\infty - \int_0^x T\,dx$ °F-ft	h_ℓ Btu/lb	h_{fg} Btu/lb	1 $\frac{h-h_\ell}{h_{fg}-h_\ell}$	2 $\frac{-A\lambda(\frac{dT}{dx})}{w(h_g-h_\ell)}$	3 $\frac{P\int_0^x (T_\infty-T)dx}{w(h_g-h_\ell)}$	f = 1 - 2 + 3 Mass Fraction
0	350	0	0	321 8	870 6	0	0	0	0
2	349	14 4	-1 0	320 8	871 3	$1\ 15\times10^{-3}$	$1\ 68\times10^{-3}$	$-4\ 92\times10^{-3}$	-0 00525
4	345	15 0	-1 7	316 6	874 6	$5\ 95\times10^{-3}$	$1\ 53\times10^{-3}$	$-8\ 33\times10^{-3}$	-0 00391
6	341	18 0	-1 8	31[illegible] 5	876 3	$8\ 33\times10^{-3}$	$1\ 86\times10^{-3}$	$-8\ 81\times10^{-3}$	-0 00232
8	341	18 6	-1 5	312 [illegible]	877 9	$10\ 7\times10^{-3}$	$1\ 89\times10^{-3}$	$-7\ 32\times10^{-3}$	0 00149
10	336	18 8	-0 6	307 1	8 2 1	$16\ 7\times10^{-3}$	$1\ 90\times10^{-3}$	$-2\ 92\times10^{-3}$	0 0119
12	334	19 8	0 8	30[illegible] 0	883 7	$19\ 0\times10^{-3}$	$2\ 00\times10^{-3}$	$3\ 88\times10^{-3}$	0 0209
14	331	20.0	2 6	301 9	886 1	$22\ 5\times10^{-3}$	$2\ 62\times10^{-3}$	$12\ 6\times10^{-3}$	0 0327
16	326	31 8	5 3	296 6	890 1	$28\ 3\times10^{-3}$	$3\ 19\times10^{-3}$	$25\ 5\times10^{-3}$	0 0506
18	321	65 6	8 8	291 5	896 0	$33\ 9\times10^{-3}$	$4\ 56\times10^{-3}$	$62\ 2\times10^{-3}$	0 0715
20	309	76.4	13 6	279 0	903 3	$47\ 4\times10^{-3}$	$7\ 36\times10^{-3}$	$65\ 5\times10^{-3}$	0 105
22	291	166 3	20 9	26[illegible] 5	916 7	$66\ 9\times10^{-3}$	$16\ 2\times10^{-3}$	$97\ 7\times10^{-3}$	0 148

T_∞ = 344°F
ω = 0.244 lb/hr
h_{in} = 321.8 Btu/lb
A = 0.0218 ft^2

λ = 1 Btu/(hr-ft-°F)
U = 2 Btu/(hr-ft^2-°F)
P = 0.523 ft

TABLE -6: RUN SW3 CALCULATIONS FOR STEAM-WATER RELATIVE PERMEABILITY

x in	(-dp/dx) psi/in	f Mass Fraction	μ_s cp	μ_w cp	$\bar{v}_s$ ft^3/lb	$\bar{v}_w$ ft^3/lb	k_s/K**	k_w/K***	S_w
0	0.271*	0	.0153	.152	3.3418	.01799	0	1.0	1.0
2		-0.00525							1.0
4		-0 00391							1 0
6		-0 00232							1 0
8	2.47	0 00149	0 0151	0 157	3 7C0<	0 01788	0 00338	0.112	0 80
10	2.50	0 0119	0 01C9	0.160	3 9860	0 01783	0 0280	0.112	0 78
12	2.70	0 0209	0 0149	0.151	<.0897	0 01781	0 0467	0.103	0 76
14	3.57	0 0327	0 0148	0 162	C Z519	0.01778	0 0571	0.0773	0 75
16	4.80	0 0506	0 0147	0 165	4 5384	0 01772	0 0697	0.0573	0 74
18	7.00	0 0715	0 0146	0 168	4 8C9<	0 01767	0 0717	0.0390	0 73
20	12.0	0 105	0 01C3	0 176	5 70<9	0.01754	0 0707	0.0228	0 72
22	15.6	0 1C8	0 0138	0 189	7 3536	0 01737	0 0954	0.0178	0 72

* dp/dx assumed equal to 100% water flowing pressure gradient

** $$k_s/K = \frac{99.1 f (u\bar{v})_s}{(-dp/dx)}$$

*** $$k_w/K = 9\ \frac{1(1-f)(u\bar{v})_w}{(-dp/dx)}$$

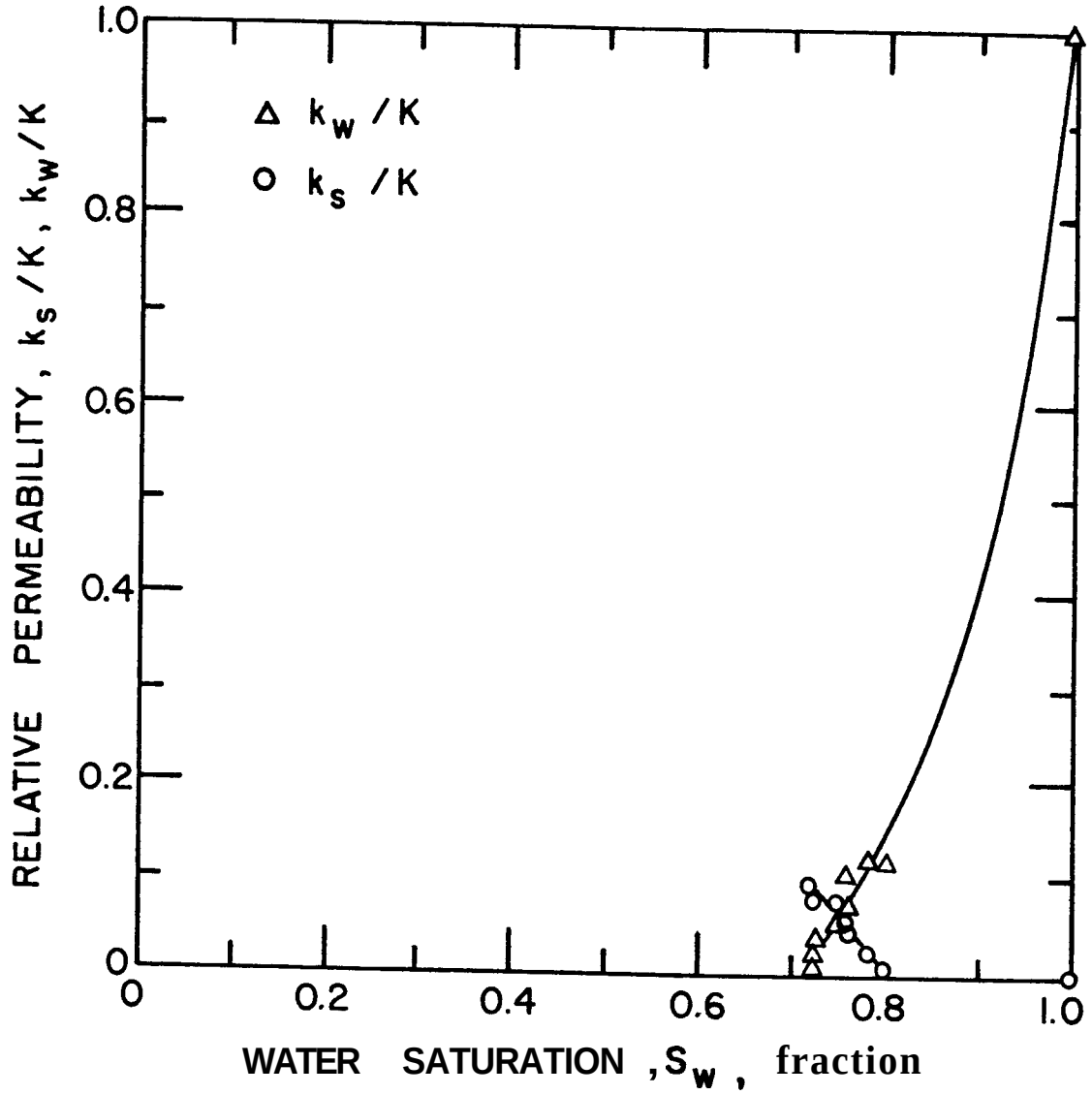

FIG. 6-17: STEAM-WATER RELATIVE PERMEABILITY VS WATER SATURATION FOR HIGH FLOW RATE, RUN SW3

6.2.8 Comparison of Three Steam-Water Runs

The most noticeable difference between the three sets of steam-water relative permeability curves is the location of the steam curve. Because the core properties of the three different synthetic cores are expected to be similar, the differences may be a function of flow rate, as described later in this section. The critical gas saturation appears to increase as the flow rate increases.

Using the present apparatus, flow rates can only be varied over a narrow range. Low flow rates result in a wider saturation range, but radial heat transfer and thermal end effects dominate at these lower flow rates. In addition, low flow rates require very low permeability cores in order to maintain sufficient backpressure to keep the inlet fluid compressed. Outlet pressure must remain low to encourage vaporization. Very low volume pumps are also required. It is not practical to use gas displacing water pumps, because the inlet fluid should be degassed prior to injection. Low flow rates may also contribute to gravity segregation effects.

Higher flow rates decrease the saturation range experienced and, as stated earlier, there is less resolution in the water saturation values at high water saturations. An apparent probe signal gradient for the case of **100%** liquid water, Φ_w, exists and may be caused by: **(1)** fines migrating to close to the outlet end during initial flushing of the core, (2) gas, produced by a reaction between the elastomer sleeve and water, that tends to migrate downstream, or **(3)** electronic or electrostatic reasons not apparent at this time. The presence of produced gas is probably not the explanation, because this effect does not vary with the pressure level of the compressed water. Many experimental runs were made

in this study; those shown here produced only minor amounts of non-condensable gas that are believed to be caused by a water elastomer reaction.

One possible explanation for the apparent rate effect is that at low flow rates, radial heat transfer dominates, causing a higher gas saturation near the outer edges of the core. Because the probe measures saturations near the core axis, the lower the flow rate, the greater the error in measured saturation. The measurement of a higher-than-actual average water saturation would cause the low flow rate curves to shift to the right, and thus give the impression of a low critical gas saturation. One problem with this explanation is that the water relative permeability curves then become inconsistent for the three runs. This would require explanation.

The formation of an annular ring of flowing water vapor and liquid water around a plug of mainly flowing liquid should also influence the relative permeability curves. The actual vapor and liquid effective permeabilities would be higher in each of their respective regions than they would be assuming homogeneous flow. To correct the low flow rate data, lowering the water relative permeability curve as flow rate decreased would contribute to both: **(1)** bringing the water relative permeability curves into closer agreement after making a qualitative correction shift to lower water saturation as flow rate decreased, and (2) forming a relative permeability curve of more reasonable shape compared to traditional gas-liquid relative permeability curves.

At this point, it becomes obvious that gas-water relative permeability curves are needed for these synthetic consolidated cores. Steam-water and gas-water relative permeability curves could then be compared.

The next section summarizes a study of the effect of temperature and pressure level on nitrogen-water drainage relative permeabilities at low confining pressures.

The effect of temperature on the relative permeability curves is expected to be minor because the confining pressure was maintained at a low value of 300-500 psig.

The lowering of the steam relative permeability curve for Run **SW3** is also suggestive of turbulence. However, Reynolds number calculations indicate that vapor turbulence is probably not a major factor for Run **SW3** *(0.244* lb/hr, f = *0.148):*

$$N_R = \frac{qd\rho}{A\mu} - 0.029$$

where d = characteristic pore diameter, ~ *0.018* cm

or:

$$N_R = \frac{qd\rho}{AS_g\mu} = 0.10$$

where S_g = *0.28*

The above calculations are qualitative because Reynolds number criteria are based on single-phase flow. Since the calculated Reynolds numbers are **low** (less than unity), it is believed that turbulence is not important (Amyx, Bass, and Whiting, 1960).

The next section evaluates the importance of gravity segregation in the boiling flow experiments.

6.2.9 Gravity Segregation

It is believed that gravity segregation does not dominate the data in these experiments. Using a form of Eq. 2-29 presented in the literature survey, characteristic time ratio values, t_v/t_H, of about three for Runs SW1 and SW2 and six for the high rate Run SW3 indicate that vapor tends to flow horizontally. An example calculation for Run SW3 follows:

$$\frac{t_v}{t_H} = \frac{L_v \Delta P}{L_H^2 \left[\frac{1}{\bar{v}_s} - \frac{1}{\bar{v}_w}\right]} = \frac{(0.0833 \text{ ft})(101 \text{ psi}) \left[144 \frac{\text{in}^2}{\text{ft}^2}\right]}{(1.925 \text{ ft})^2 \left[\frac{1}{.01737 \frac{\text{ft}^3}{\text{lb}}} - \frac{1}{7.3536 \frac{\text{ft}^3}{\text{lb}}}\right]} = 5.7$$

The next section discusses the possible influence of capillary end effects.

6.2.10 Capillary End Effects

Outlet end effects, caused by capillary retention of liquid water at the outlet face of the core, were not measured, and are not expected to influence this data significantly. Runs SW1, SW2, and SW3 had flowing pressure drops of 52 psi, 53 psi, and **101** psi, respectively. The water relative permeability curves do not increase in magnitude with increasing pressure drop.

The next section discusses the problem of confining pressure sleeve gas production.

6.2.11 Confining Pressure Sleeve Gas Production

Past studies have experienced trouble with: **(1)** gases emanating from the elastomer confining sleeves, and (2) confining gases passing through the elastomer sleeves. Chen (1976) solved the second problem by

using water as the confining fluid rather than nitrogen. Viton and silicone rubber tend to evolve gas when in the presence of steam and water. Materials selection charts indicated that ethylene propylene could withstand steam and hot water. Tests indicated that ethylene propylene sleeves also produced gas. Ethylene propylene discolored the produced water and produced a strong odor. Silicone rubber sleeves also discolored the water and had a slightly less offensive odor. Both silicone rubber and ethylene propylene maintained their integrity at temperatures above 350°F. Ethylene propylene smoked badly when placed in 250°F air. Silicone rubber was much more stable in hot air and had only a slight odor. As a result, silicone rubber was used in most of the experiments in this study. The fact that produced water was obviously affected by the sleeve material led to efforts to separate the elastomer from the core. Both kitchen quality aluminum foil and a soldered, thin copper foil were used to isolate the core from the elastomer. Both attempts failed. Permeability measurements of a Berea core with and without the foil showed the core-foil permeability was higher than the core permeability and decreased with increasing confining pressure at room temperature. This indicated fluid bypass along "wrinkles" formed at the core-foil interface. At this stage of the investigation, the elastomers did not have an observed, significant effect on the core. Subsequent investigation suggested that the silicone rubber sleeve causes the cores to lose their natural water wettability.

The next section suggests improvements for future boiling flow experiments.

6.2.12 Future Improvements

Future improvements to this type of experiment should include adiabatic sections along the core length in a manner similar to that of Miller (1951). This improvement may be difficult to implement with a Hassler-type core holder. Provision for temperature control along the core length by a set of separately controlled heat tapes will help reduce any problems caused by radial heat transfer from the environment. The drawback of adiabatic flow is the limited water saturation range that will be encountered.

Another possibility is to inject two-phase fluids of known enthalpy and quality. Otherwise, experiments similar to those conducted in this study should use a pump designed for very low rates, lower permeability cores should be fabricated, and greater control exercised over the air bath temperature distribution. A study of the thermal conductivity and overall heat transfer coefficients for multiphase flow in porous media should be made. Other methods of measuring water saturation profiles should also be investigated.

This concludes the section on the nonisothermal, boiling flow experiments. The next section presents the results of the isothermal, gas-drive experiments.

6.3 Isothermal, Unsteady, External Gas-Drive Experiments

This section presents the results for three unsteady, isothermal, nitrogen gas-displacing-water experiments. The experiments were performed at a variety of temperatures and mean pressures, using a high pressure gas-water separator at the outlet end, as described in Sections 4 and 5. The synthetic sandstone core used in the isothermal flow experiments was the *36* **md** core used in Run **SW3** of the nonisothermal boiling experiments.

Gas and water relative permeabilities can be obtained from the cumulative gas and water production data recorded as a function of time. Inlet and outlet pressures, as well as pressure drop and temperature, were also recorded. The data and calculations required to develop gas-water relative permeabilities are presented in Appendix A3.3.

The gas-water relative permeability curves presented in Fig. 6-18 demonstrate that at the temperatures (70-300°F) and low confining pressures (300-500 psig) used in this study, gas and water relative permeabilities were not strong functions of temperature.

The calculated gas-water relative permeability data at 78°F, 198°F, and 294°F almost fall on a single set of relative permeability curves. Much of the scatter in the gas curve is due to: **(1)** experimental error, (2) graphical analysis error, and **(3)** approximations used to describe the effects of water vaporization in the core. The three runs presented in this section are representative of the many runs made at different temperature and pressure levels.

The following section summarizes the calculations required to generate the relative permeability values.

6.3.1 Calculation Procedure

The calculation procedure suggested by Jones and Roszelle (1976) can be modified in the following way to determine gas-liquid relative permeabilities at various temperatures and pressures. Cumulative separator gas production is corrected from room conditions to average core conditions by suming the incremental production from time t_{j-1} to time t_j:

$$G_{sep} = \Sigma \Delta G_{sep} \qquad (6\text{-}15)$$

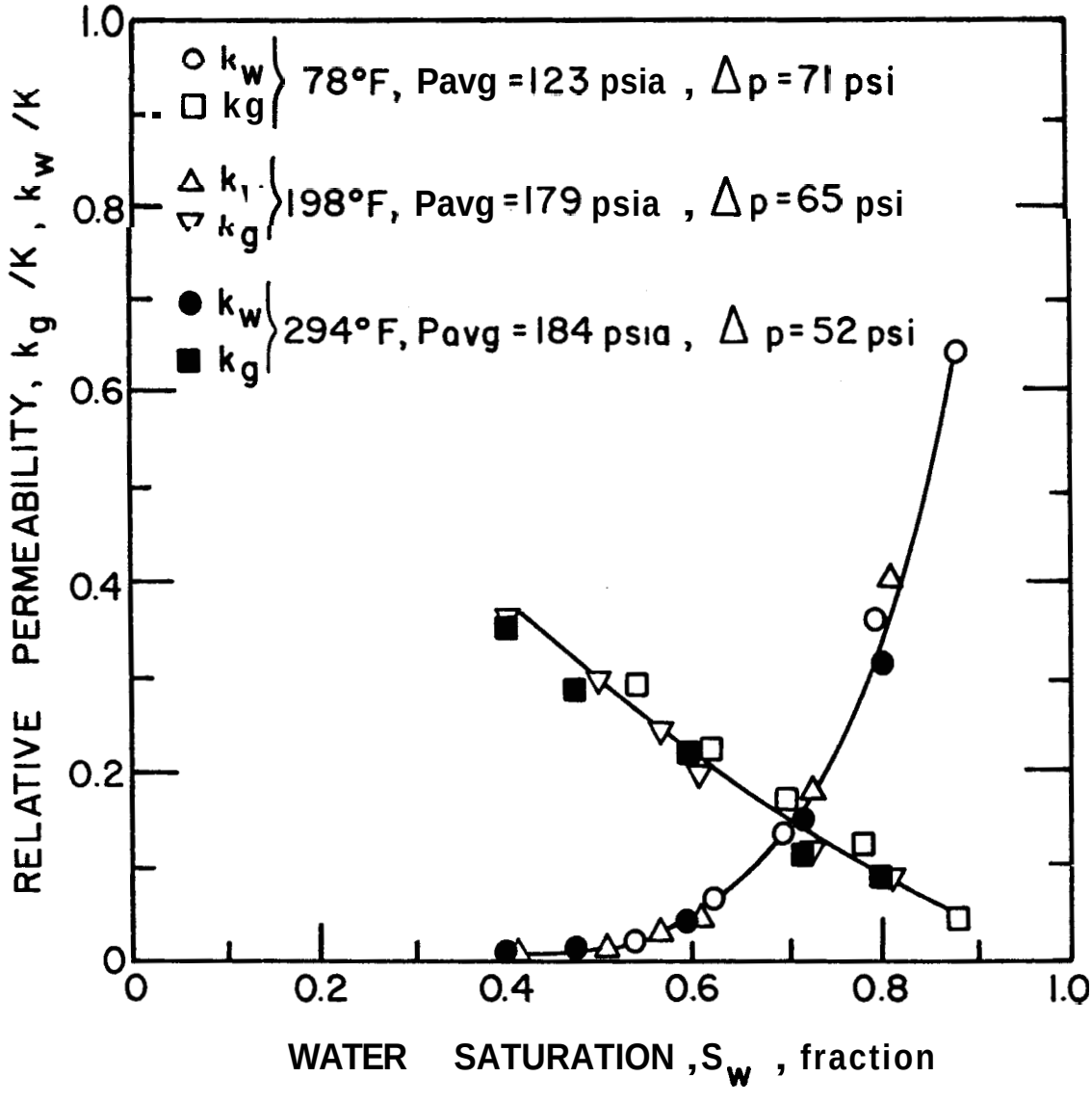

FIG. 6-18: GAS-WATER DRAINAGE RELATIVE PERMEABILITY VS WATER SATURATION FOR SEVERAL TEMPERATURES

where:

$$\Delta G_{sep}(T_{core},p_{avg}) = \Delta G_{sep}(T_{room},p_{bar}) \frac{p_{bar}}{p_{avg}} \frac{T_{core}}{T_{room}} \qquad (6\text{-}16)$$

and G_{sep} = separator gas production after breakthrough

T_{core} = core absolute temperature

T_{room} = room absolute temperature

p_{bar} = barometric absolute pressure

$p_{avg} = (p_{in}+p_{out})/2$ = average absolute pressure across core

$Z_{core} = Z_{room} = 1.0$

The cumulative gas injected into the core is:

$$G_{inj}(T_{core},p_{avg}) = [G_{sep}(T_{core},p_{avg})] \left[\frac{1}{1-y_{H_2O}} \right] + W_{p(room)} \frac{\bar{v}_{w,core}}{\bar{v}_{w,room}} \qquad (6\text{-}17)$$

where:

G_{inj} = cumulative gas injected into core

W_P = cumulative water produced from core

$\bar{v}_{w,core}$ = water specific volume at core temperature

$\bar{v}_{w,room}$ = water specific volume at room temperature

y_{H_2O} = mole fraction water vapor in nitrogen-water vapor gas mixture

The term $1/(1-y_{H_2O})$ is the correction factor that considers the gas expansion due to water evaporation.

The gas injection rate, q, is calculated for each time increment as:

$$q = \frac{(G_{inj}) - (G_{inj})_{j-1}}{t_j - t_{j-1}} \qquad (6\text{-}18)$$

The cumulative gas injection in units of pore volume is $Q_i = G_{inj}/V_p$, where V_p is the pore volume of the core sample. Average gas saturation, $\bar{S}_g$, is:

$$\bar{S}_g = 1 - \bar{S}_w = 1 - \frac{W_p}{V_p}\frac{\bar{v}_{core}}{\bar{v}_{room}} \qquad (6\text{-}19)$$

The average relative reciprocal mobility term:

$$\left[\frac{q\mu}{\Delta p}\right]_b \left[\frac{\Delta p}{q}\right] = \overline{\lambda^{-1}} \qquad (6\text{-}20)$$

can also be calculated where Δp is the pressure drop across the core and $(q\mu/\Delta p)_b$ is the single-phase data that is representative of the core absolute permeability to water. The term λ^{-1} is called the average relative reciprocal mobility because it is related to the relative permeabilities and viscosities of the two phases:

$$\overline{\lambda^{-1}} = \frac{K}{\frac{k_w}{\mu_w} + \frac{k_g}{\mu_g}} \qquad (6\text{-}21)$$

where:

k_w = water effective permeability

k_g = gas effective permeability

The next step is to graph $\bar{S}_g$ **vs** Q_i on coordinate graph paper. The outlet face gas saturation, S_{g2}, is then obtained **as** a function ***of*** cumulative gas injection, Q_i, by recording the zero Q_i intercept of the tangent at several values of Q_i. The initial $\bar{S}_g$ vs Q_i data points should

be linear to the time of gas breakthrough, This line should extrapolate back to $S_{g2} = S_{gi} = 0$.

Finally, graph $\overline{\lambda^{-1}}$ vs Q_i on coordinate graph paper, The outlet face mobility term, λ_2^{-1}, is obtained as a function of Q_i by recording the zero Q_i intercept of the tangent at several values of Q_i. The initial $\overline{\lambda^{-1}}$ vs Q_i data points should be linear to the time of gas breakthrough. This line should extrapolate back to the value of the water viscosity, μ_w.

The relative permeabilities can then be calculated:

$$k_{rw} = \frac{f_{w2}\mu_w}{\lambda_2^{-1}} \tag{6-22a}$$

$$k_{rg} = \frac{f_{g2}\mu_g}{\lambda_2^{-1}} \tag{6-22b}$$

where:

$$f_{w2} = \frac{\overline{S}_g - S_{g2}}{Q_i} \tag{6-23a}$$

$$f_{g2} = 1 - f_{w2} \tag{6-23b}$$

f_{w2} = fractional flow of water

f_{g2} = fractional flow of gas

The above equations assume no capillary effects ($p_c = p_g - p_\ell = 0$).

A computer program was used to process the raw lab data and calculate relative permeability. The data was smoothed using cubic spline subroutines from the International Mathematical and Statistical Library.

Optimum knot locations for the cubic splines were automatically determined by minimizing the least squares error. The computed slopes, intercepts, relative permeabilities, and saturations showed good agreement with values obtained by hand graphical analysis.

A review of the equations required to calculate gas and water relative permeabilities indicates that the porosity (or pore volume) estimate does not influence the calculated values of k_g/K or k_w/K. However, the outlet face saturations are dependent upon the porosity of the core. For the core used in this study, porosity was determined by first evacuating the core and then saturating it at a pressure of 300 psig. The difference in the weight of the dry core and the saturated core was then related to core porosity (34%).

We turn now to a discussion of important fluid properties and the impact of water vaporization on the experimental results.

6.3.2 Fluid Properties and the Effects of Water Vaporization

In this section, gas density and fluid viscosity relations are discussed. The importance of liquid water vaporization is also discussed in detail.

Using methods described in Reid, Prausnitz, and Sherwood (1977) and Katz et al. (1959), it was found that nitrogen density varies with temperature and pressure in the same manner as an ideal gas for the range of conditions encountered in this study (0-200 psig, 70-300°F).

Because the injected nitrogen is not saturated with water at core temperature and pressure, three water vaporization effects must be considered: (1) gas mixture viscosity reduction as the mole fraction of water vapor increases, (2) core drying, or water saturation reduction

caused by dry nitrogen injection, and (3) gas volume expansion as the mole fraction of water vapor increases. The potential importance of each factor is discussed in the following three sections.

6.3.2.1 Effect of Water Vaporization on Gas Mixture Viscosity

Dry nitrogen is diluted by water vapor when the nitrogen gas comes in contact with liquid water at elevated temperatures. This is caused by the high vapor pressure of water.

The mole fraction of water vapor in the nitrogen gas can be estimated from Dalton's and Raoult's laws:

$$y_{H_2O} = \frac{p_p}{p_T} = \frac{x_{H_2O} p_{vp}}{p_T} = \frac{p_{vp}}{p_T} \qquad (6\text{-}24)$$

where:

y_{H_2O} = mole fraction water in vapor phase

x_{H_2O} = mole fraction water in liquid phase (Henry's Law indicates $x_{H_2O} \approx 1.0$)

p_p = partial pressure of water in vapor phase

p_{vp} = vapor pressure of liquid water (from Steam Tables)

p_T = total pressure of vapor phase mixture

$y_{N_2} = 1 - y_{H_2O}$

The effect of vapor phase pressure and temperature on water vaporization is presented in Fig. 6-19.

The viscosities of water, steam, and nitrogen are required to calculate gas-mixture and water relative permeability, Liquid water viscosity was obtained from the Electrical Research Association 1967 Steam

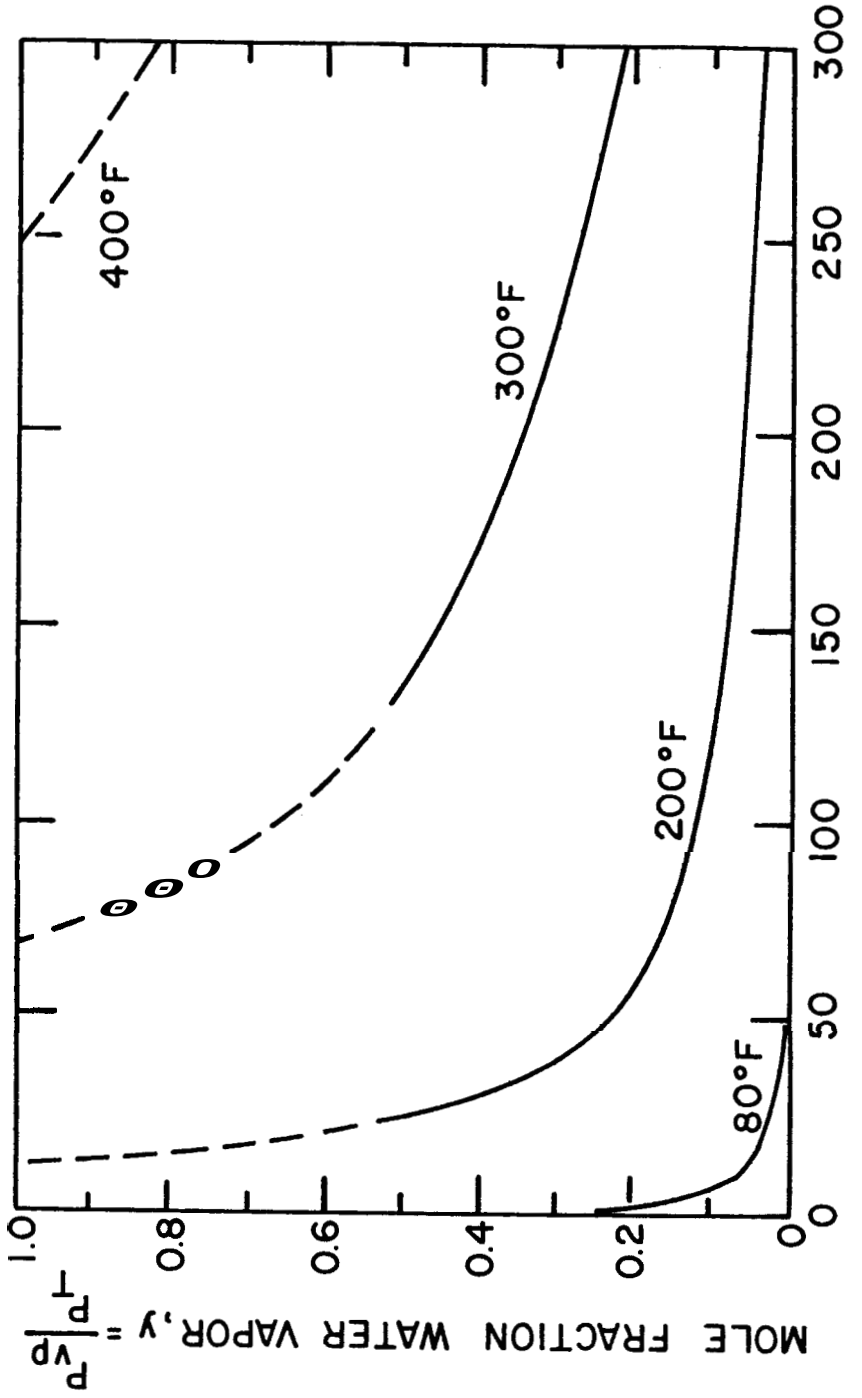

FIG. 6-19: WATER VAPOR CONCENTRATION IN NITROGEN-WATER VAPOR MIXTURE (CALCULATED USING RAOULT'S LAW AND DALTON'S LAW

Tables. Steam viscosity was estimated using an equation presented by Farouq Ali (1970):

$$\mu_{steam} = 0.17 \times 10^{-4} \, T^{1.116} \tag{6-25}$$

where:

μ = viscosity, cp

T = temperature, °K = °C + 273.1

Nitrogen gas viscosity was estimated using the Sutherland equation obtained from the International Critical Tables (V-2):

$$\mu_{N_2} = 0.01765 \left[\frac{296.1+110.6}{T+110.6} \left[\frac{T}{296.1} \right]^{3/2} \right] \tag{6-26}$$

where:

μ = viscosity, cp

T = temperature, °K

Using methods described by Reid, Prausnitz, and Sherwood (1977), it was found that the effect of pressure on the viscosity of nitrogen was not important for the range of conditions encountered in this study. The same conclusion is reasonable for the steam and the nitrogen-water vapor mixture viscosity. Although Farouq Ali (1970) presented equations characterizing the pressure dependence of steam viscosity, these relationships were not used because there is significant disagreement in the literature as to the magnitude and direction of viscosity change caused by pressure level. In any event, the low pressure levels used in this study would not affect gas mixture viscosity more than a few percent.

Table 6-7 indicates the potential importance of water vapor on vapor phase viscosity. The Herning and Zipperer (Reid et al., 1977; Ali, 1970) mixture law is used here (although more complicated techniques are often recommended for mixtures that include polar gases):

$$\mu_{mix} = \frac{y_1\mu_1(M_1)^{0.5} + y_2\mu_2(M_2)^{0.5}}{y_1(M_1)^{0.5} + y_2(M_2)^{0.5}} \qquad (6\text{-}27)$$

where:

M = molecular weight

y = mole fraction

μ = viscosity

6.3.2.2 Effect of Water Vaporization on Water Saturation

Water saturation at the core inlet may be less than the water saturation immediately downstream due to the vaporization of water by the dry nitrogen gas. The amount of core drying can be estimated in terms of grams of water produced per liter of nitrogen produced at room temperature and atmospheric pressure:

$$\frac{\text{gm } H_2O}{\ell N_2} = \frac{18\ y_{H_2O}}{(1-y_{H_2O})}\left[\frac{p}{RT}\right] \qquad (6\text{-}28)$$

where:

R = gas law constant, 0.08207 (ℓ atm)/(mol K°)

T = temperature, °K

p = pressure, atm

y_{H_2O} = mole fraction water in vapor phase

TABLE 6-7: NITROGEN-WATER VAPOR MIXTURE VISCOSITY AT SEVERAL TEMPERATURES AND PRESSURES

Temperature, °F	Total Pressure, psia	Viscosity, cp		Mole Fraction,	Gas Mixture Viscosity, cp
		Steam	Nitrogen	Water	
70	1C 7	0 00967	0 0176	0 02C7	0 017C
70	200	0 00967	0 0176	0 00182	0 0176
Z00	1C 7	0 012C	0 0Z07	0 78C	0 01 5
200	200	0 012C	0 0207	0 0576	0 0203
300	1C 7	0 01C5	0 02Z9	–	–
300	200	0 014E	0 0229	0 335	0 0Z05

As shown in Table 6-8, core drying is only significant at high temperatures and low pressures. Elevated pressure tends to reduce the magnitude of core drying. For the case where the core is at 294°F and 184 psia, 36.9 grams of water may be removed from the core due to vaporization, not gas-water immiscible displacement, for every 100 liters of nitrogen produced.

For a steady flow process, the evaporated water collected in the heat exchanger should be subtracted from the liquid water flow rates that are based on separator liquid effluent. Because the process under consideration is unsteady, the solution should be obtained using the fractional flow equation, the frontal advance equation, and a Welge-type equation that relates average water saturation to outflow end saturation. Afterwards, a correction should be made in the mobility terms.

If it is assumed that all water vaporization occurs at the inlet end of the core, then it can also be expected that a dry region ($S_g = 1.0$) may extend a distance x_{dry} into the core. The distance x_{dry} will increase with increased cumulative nitrogen injected.

The fractional flow equation:

$$f_g = \frac{1}{1 + \frac{\mu_g}{\mu_w}\frac{k_w}{k_g}} \tag{6-29}$$

and the frontal advance equation:

$$\left[\frac{\partial L}{\partial t}\right]_{S_g} = \frac{q_t}{A\phi}\left[\frac{\partial f_g}{\partial S_g}\right]_t \tag{6-30}$$

will apply for that part of the core downstream of the dried zone.

TABLE 6-8: AMOUNT OF WATER VAPORIZATION AT SEVERAL TEMPERATURES AND PRESSURES

Core Temperature, °F	Vapor Pressure of Water at Core Temperature, psia	Core Pressure, psia	Ambient Temperature, °F	Atm. Pressure, psia	Moles Water per Mole Dry Nitrogen, $y_{H_2O}/(1-y_{H_2O})$	Water Vaporized per Liter of Gas at Room Conditions gm $H_2O/(\ell N_2)$
78	0.475	123	78	14.7	0.00386/0.996	0.00285
198	11.1	179	73	14.7	0.0620/0.938	0.0690
294	61.2	184	75	14.7	0.333/0.667	0.369
299	66.0	131	69	14.7	0.504/0.496	0.759

Integrating the frontal advance equation from x_{dry} to L, and from time zero to the time when cumulative injection is Q_i:

$$f'_g = \frac{(L-x_{dry})}{L} \frac{1}{Q_i} \tag{6-31}$$

where:

$$f'_g = \frac{df_g}{dS_g} \tag{6-32}$$

$$Q_i = \frac{\int_o^t q_t \, dt}{LA\phi} \tag{6-33}$$

and the correction has been made for gas volume expansion caused by evaporation.

Welge's equation:

$$\overline{S}_g = S_{g2} \quad Q_i f_{w2} \tag{6-34}$$

is not appropriate, and another equation must be derived to relate average and producing end saturations during the gas drive. The new equation can be obtained in a way similar to that described in Craig (1971).

For the saturation-distance relationship shown in Fig. 6-20, the average displacing fluid saturation for the region from $x_1 (x_{dry})$ to L is:

$$\overline{S}_g = \frac{\int_1^2 S_g \, dx}{L-x_{dry}} \tag{6-35}$$

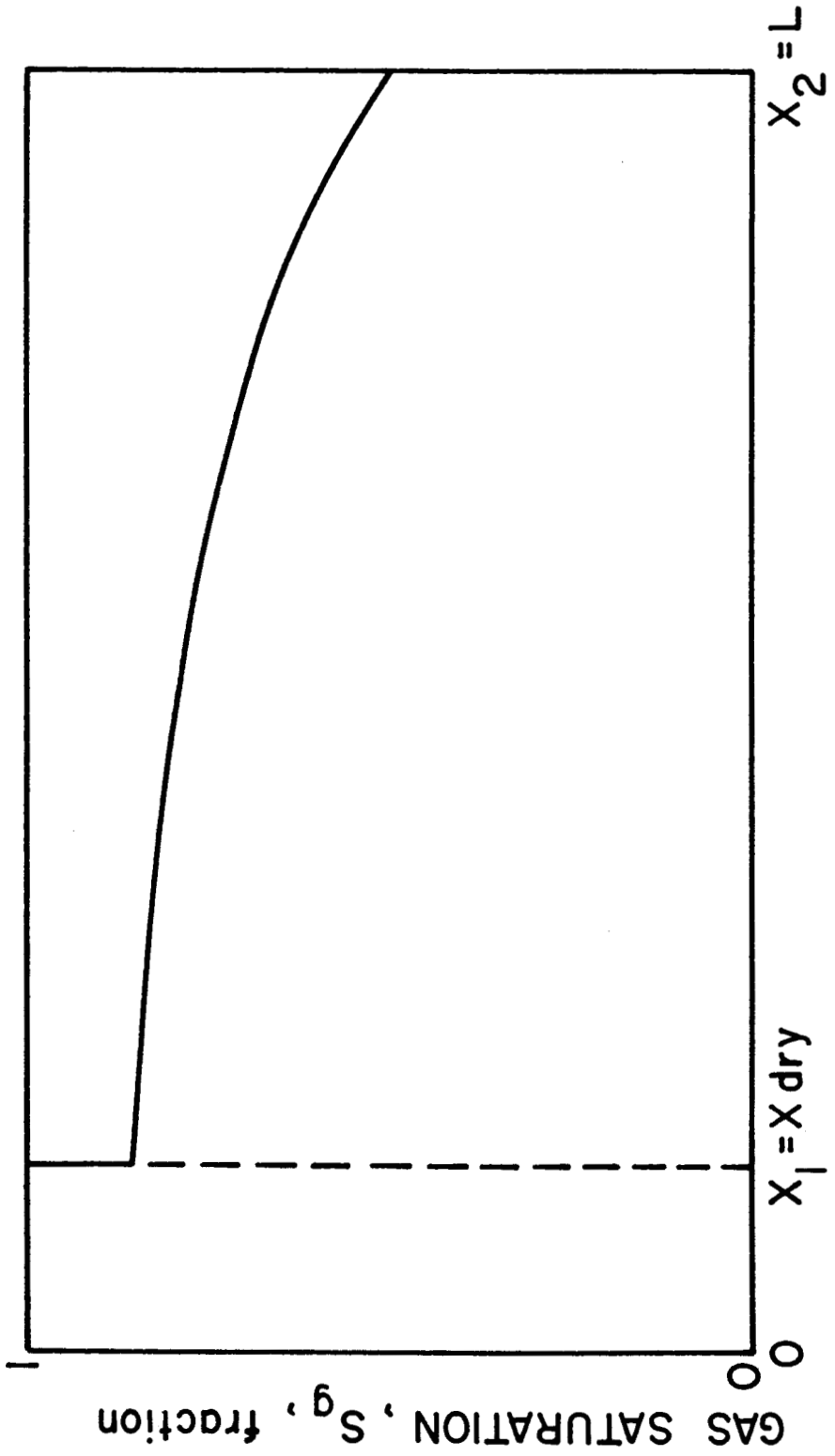

FIG. 6-20: SATURATION VS DISTANCE: SCHEMATIC FIGURE DURING DRY GAS INJECTION WITH WATER VAPORIZATION AT INLET

From Eq. 6-31, f'_g is proportional to $(L-X_{dry})$:

$$\bar{S}_g = \frac{\int_1^2 S_g df'}{f'} \tag{6-36}$$

Integrating by parts:

$$\bar{S}_g = \frac{S_{g2}f'_{g2} - S_{g1}f'_{g1} - \int_1^2 f'_g dS_g}{f'_{g2}} \tag{6-37}$$

The quantity f'_{g1} is unknown at $x_1 = x_{dry}$. Assume $f'_{g1} \to 0$ and $f_{g1} = 1$. The result is:

$$\bar{S}_g = S_{g2} - \frac{(f_2 - 1)}{f'_{g2}} \tag{6-38}$$

Using Eq.6-31 for the outflow end of the core:

$$\bar{S}_g = S_{g2} - \left[\frac{L}{L-x_{dry}}\right] f_{w2}Q_i \tag{6-39}$$

The above expression is the average gas saturation for the region from x_{dry} to L. The average gas saturation for the entire core is:

$$\bar{S}_g(0\to L) = [\bar{S}_g(0\to x_{dry})]\frac{x_{dry}}{L} + [\bar{S}_g(x_{dry}\to L)]\left[\frac{L-x_{dry}}{L}\right] \tag{6-40}$$

$$= (1)\frac{x_{dry}}{L} + \left[S_{g2} - \left[\frac{L}{L-x_{dry}}\right] f_{w2}Q_i\right]\left[\frac{L-x_{dry}}{L}\right] \tag{6-41}$$

$$= \frac{x_{dry}}{L} + S_{g2}\left[- f_{w2}Q_i \right. \tag{6-42}$$

where :

$$x_{dry} = \frac{\left\{\frac{\text{gm } H_2O}{\ell N_2}\right\} V_{N_2} \bar{v}_{w,core}}{A\phi} \qquad (6-43)$$

$$x_{dry} = \frac{(18)y_{H_2O}}{(1-y_{H_2O})} \frac{V_{N_2} \bar{v}_{w,core}}{A\phi R} \left[\frac{p}{T}\right]_{room} \qquad (6-44)$$

V_{N_2} = cumulative volume of nitrogen injected at room conditions

$\bar{v}_{w,core}$ = specific volume of liquid water at core conditions

V_p = core pore volume

A = cross-sectional area of core

ϕ = core porosity

The usual graph of $\bar{S}_g$ vs Q_i on coordinate graph paper will provide tangents of:

$$\text{slope} = f_{w2} \qquad (6-45)$$

$$\text{zero } Q_i \text{ intercept} = \frac{x_{dry}}{L} + S_{g2}\left[\frac{L-x_{dry}}{L}\right] \qquad (6-46)$$

The outlet end gas saturation, S_{g2}, and water fractional flow, f_{w2}, can be calculated because L is known and x_{dry} can be computed:

$$S_{g2} = \left[\text{intercept} - \frac{x_{dry}}{L}\right]\left[\frac{L}{L-x_{dry}}\right] \qquad (6-47)$$

$$f_{w2} = \frac{\bar{S} - \text{intercept}}{Q_i} \qquad (6-48)$$

The above results indicate that: (1) if no vaporization occurs, $x_{dry} = 0$ and the results reduce to the usual displacement equations, (2) using the intercept value, the correct f_{w2} and f_{g2} values will be calculated whether or not vaporization occurs ($x_{dry} \geq 0$), and (3) relative permeability will be graphed as a function of incorrect saturations if the intercept value is assumed to be the outlet face saturation, S_{g2}, when vaporization occurs ($x_{dry} > 0$).

Table 6-9 shows that only small gas saturation corrections are required at large injection volumes. In general, the required correction is small except for very large cumulative injection volumes at 'high temperatures and low pressures. The experiments in this study were terminated before the vaporization of liquid from the core affected the results appreciably.

It is interesting that inlet end water saturation reduction due to vaporization requires a correction in the outlet end water saturation.

The assumption that all water evaporation occurs at the core inlet is not strictly correct because, due to the flowing pressure gradient, some vaporization occurs along the entire length of the core. The region of unit gas saturation, x_{dry} in length, could perhaps be more appropriately considered a region of $(1-S_{wi})$ gas saturation of length $x_{dry}\left[\frac{1}{1-S_{wi}}\right]$, where S_{wi} is the irreducible water saturation. But a similar analysis would again indicate small corrections to the outflow liquid saturation.

Now, all that remains is to correct the relative reciprocal mobility terms, $\overline{\lambda^{-1}}$ and λ_2^{-1}, to consider the inlet region of lowered water saturation. This decreased water saturation should cause an increased

TABLE 6-9: OUTLET END SATURATION CORRECTED FOR WATER VAPORIZATION

E eriment Run No.	Volume Nitrogen Injected at Room Conditions liters	x_{dry} inch	Intercept [at $Q_i=0$] of the Tangent	Corrected Outlet End Gas Saturation, S_{g2} pore volume
NW2	232	0.676	0 585	0.572
NW2	115	0.336	0 539	0.532
NW2	56.7	0.165	0 505	0.501
NW3	89.5	2.05	0.598	0.5 59
NW3	61.3	1.40	0.571	0.5 43
NW3	29.9	0.685	0.528	0.5 14
NW3	14.2	0.325	0.469	0.4 61

flow rate and decreased pressure drop compared to the case of no evaporation. The decreased pressure drop (Δp) will lower the reciprocal mobility terms ($\overline{\lambda^{-1}}$ and χ_2^{-1}) and increase the calculated values of relative permeabilities over values obtained with no vaporization.

The methods of Johnson et al. (1959) and Jones and Roszelle (1976) can be combined to derive an approximate expression characterizing the relationship between relative reciprocal mobility (χ^{-1}), cumulative injection (Q_i), and relative permeability to water (k_{rw}).

At a given time in the displacement process, the total pressure drop across the core may be considered by a succession of steady states in space:

$$\Delta p = -\int_0^L \frac{\partial p}{\partial x}\, dx \qquad (6-49)$$

Using Darcy's law for the water phase over an incremental distance, and treating the total flow rate as a function of time (not space):

$$\frac{\Delta p K A}{q \mu_w} = \int_o^L \frac{f_w}{k_{rw}}\, dx \qquad (6-50)$$

The frontal advance equation integrated from x_{dry} to x is:

$$x - x_{dry} = L f_g' Q_i \qquad (6-51)$$

Thus at a given time:

$$dx = LQ_i df'_g \qquad (6-52)$$

and at $x = L$:

$$f'_g = \left[\frac{L-x_{dry}}{L}\right] \frac{1}{Q_i} \qquad (6-53)$$

Incorporating these results into Eq. *6-50* and differentiating both sides yields:

$$\frac{KA}{\mu_w L} d\left[\frac{\Delta p}{q_t Q_i}\right] = \frac{f_{w2}}{k_{rw}} df'_{g2} \qquad (6-54)$$

$$= \frac{f_w}{k_{rw}} \left[\frac{L-x_{dry}}{L}\right] d\left[\frac{1}{Q_i}\right] \qquad (6-55)$$

It was again assumed that $f'_g = 0$ at $x = x_{dry}$.

Using the definition of the drivative of a quotient:

$$\frac{f_{w2}}{k_{rw}} \quad \frac{\mu_w(L-x_{dry})}{KA} = \frac{\Delta p}{q_t} - Q_i \frac{d(\Delta p/q_t)}{dQ_i} \qquad (6-56)$$

Thus, a graph of $(\Delta p/q_t)$ vs Q_i provides tangents whose zero Q_i intercept *is:*

$$\frac{f_w}{k_{rw}} \quad \frac{\mu_w(L-x_{dry})}{KA}$$

The equation can be presented in terms of λ^{-1} (Jones and Roszelle) and Q_i because:

$$\overline{\lambda^{-1}} = \frac{KA}{L} \frac{\Delta p}{q_t} \tag{6-57}$$

Thus:

$$\frac{f_{w2}\mu_w}{k_{rw}}\left[\frac{(L-x_{dry})}{L}\right] = \overline{\lambda^{-1}} - Q_i \left[\frac{KA}{L}\frac{d(\Delta p/q_t)}{dQ_i}\right] \tag{6-58}$$

In this case, a graph of $\overline{\lambda^{-1}}$ vs Q_i provides tangents whose zero Q_i intercept is:

$$\text{intercept} = \frac{f_{w2}\mu_w}{k_{rw}}\left[\frac{(L-x_{dry})}{L}\right] \tag{6-59}$$

The water relative permeability is:

$$k_{rw} = \frac{f_{w2}\mu_w}{\text{intercept}}\left[\frac{(L-x_{dry})}{L}\right] \tag{6-60}$$

where x_{dry} is obtained from Eq. 6-43 and f_{w2} is obtained from Eq. 6-48.

The preceding Table 6-9 shows that near the end of Run NW3, x_{dry} is only 2.05 inches compared to the core length L of 23.1 inches. Thus, the correction to the gas and water relative permeabilities was small for all runs. Except for the last data point in Run NW3, the corrections for water saturation reduction due to vaporization are believed to be negligible. Therefore, the gas-drive relative permeabilities presented in this study were not corrected for water saturation reduction caused by vaporization. If larger volumes of nitrogen had been injected at elevated temperature, a correction would have been required.

The next section presents a method of correcting for the gas mixture volume increase resulting from water vaporization. This is the third and final water vaporization effect discussed in this report.

6.3.2.3 Effect of Water Vaporization on Gas Mixture Volume

This section demonstrates that the gas injection volume corrected for water vaporization must equal the volume of flowing nitrogen and water vapor. Because only the noncondensible nitrogen can be measured after the separator, the nitrogen volume must be increased to include the water vapor:

$$\text{vol}(H_2O+N_2) = \text{vol } N_2 \left[\frac{1}{1-y_{H_2O}}\right] \tag{6-61}$$

where y_{H_2O} = mole fraction H_2O in vapor phase.

This equation includes the assumptions of instantaneous liquid-vapor phase equilibrium, and that nitrogen, water vapor, and their mixtures behave like ideal gases. Figure 6-21 presents the correction factor as a function of temperature and pressure.

If one calculated the gas volumes, relative reciprocal mobilities, and gas-water relative permeabilities neglecting the impact of volume expansion, and labeled them Q_i', $\lambda^{-1}{}'$, k_{rg}', and k_{rw}', obvious approximate corrections might be made by the relations:

$$Q_i = Q_i' \frac{1}{(1-y_{H_2O})} \tag{6-62}$$

$$\overline{\lambda^{-1}} = \overline{\lambda^{-1}}' \, (1-y_{H_2O}) \tag{6-63}$$

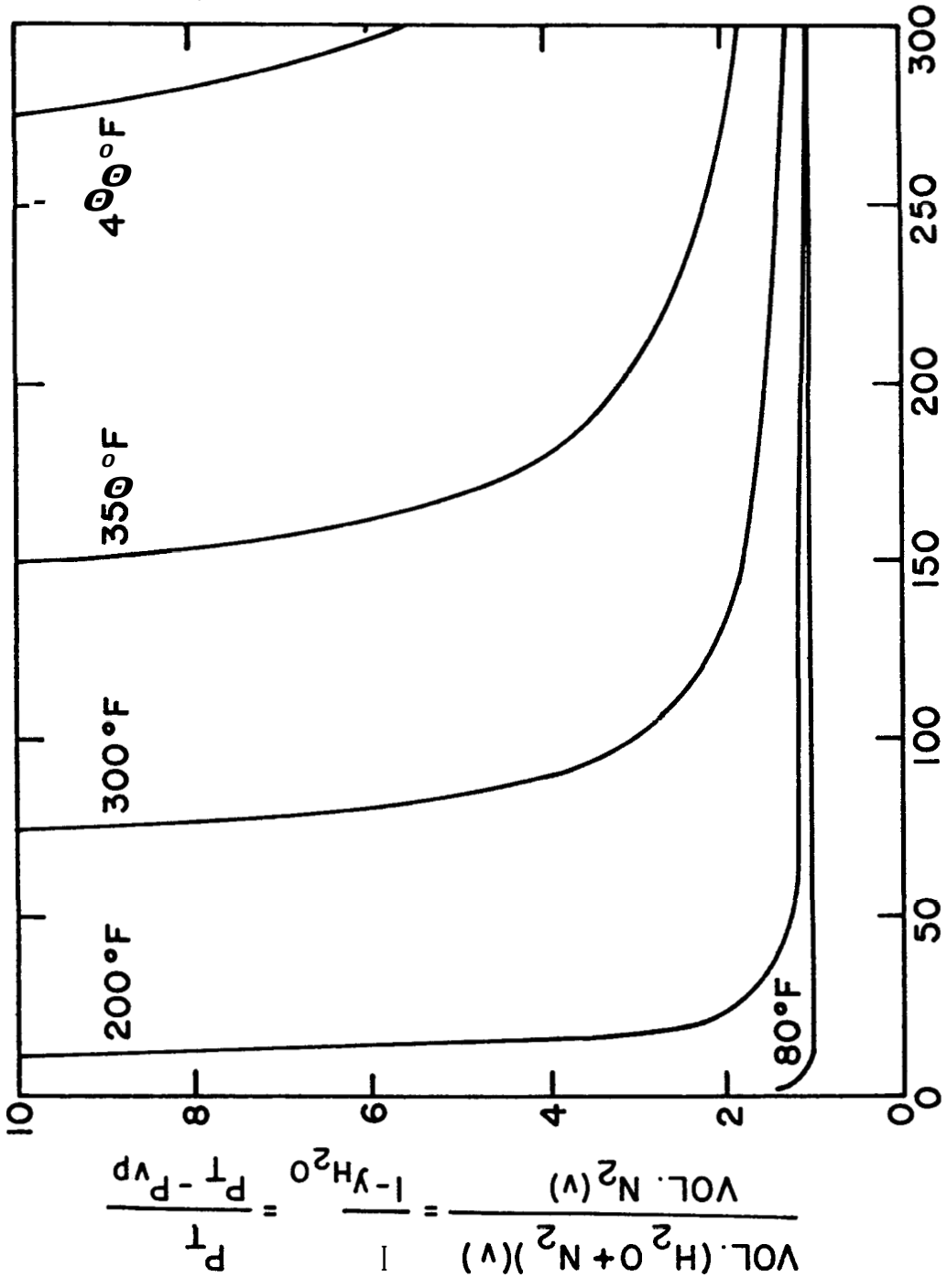

FIG. 6-21: CORRECTION FACTOR REQUIRED TO ESTIMATE NITROGEN-WATER VAPOR MIXTURE VOLUME FROM NITROGEN VOLUME (CALCULATED USING RAOULT'S LAW AND DALTON'S LAW)

$$k_{rg} = \frac{\mu_g}{\overline{\lambda_2^{-1}}'} \left[\frac{y_{H_2O}}{1-y_{H_2O}} \right] + k_{rg}' \qquad (6-64)$$

$$k_{rw} = k_{rw}' \qquad (6-65)$$

Equation *6-17* shows this method of correction is improper. Furthermore, there is enough scatter in the X^{-1} vs Q_i graph at low Q_i values that the relation $\overline{\lambda^{-1}} \approx \mu_w$ at $Q_i = 0$ must be used to draw the proper straight line through the early data before breakthrough. This may also influence the decision **on** where to position the curve just after breakthrough.

Without the volume expansion correction, $X^{-1'}$, or

$$\frac{\overline{\lambda^{-1}}}{(1-y_{H_2O})}$$

is incorrectly set to μ_w at $Q_i = 0$. It is not sufficient to set:

$$\frac{\overline{\lambda^{-1}}}{(1-y_{H_2O})} = \frac{\mu_w}{(1-y_{H_2O})} \qquad (6-66)$$

at $Q_i = 0$. The only way to correct the analysis is to regraph X^{-1} vs Q_i using the correct rates and volumes in $\overline{X^{-1}}$ and Q_i. The final correction may affect both gas and water relative permeability at low gas saturation.

The calculated gas-water relative permeability data <u>without</u> correction for gas expansion due to water vaporization is shown in Fig. *6-22.* The uncorrected gas data show an apparent decrease in gas relative permeability with increasing temperature. The water relative permeability appears to be temperature independent.

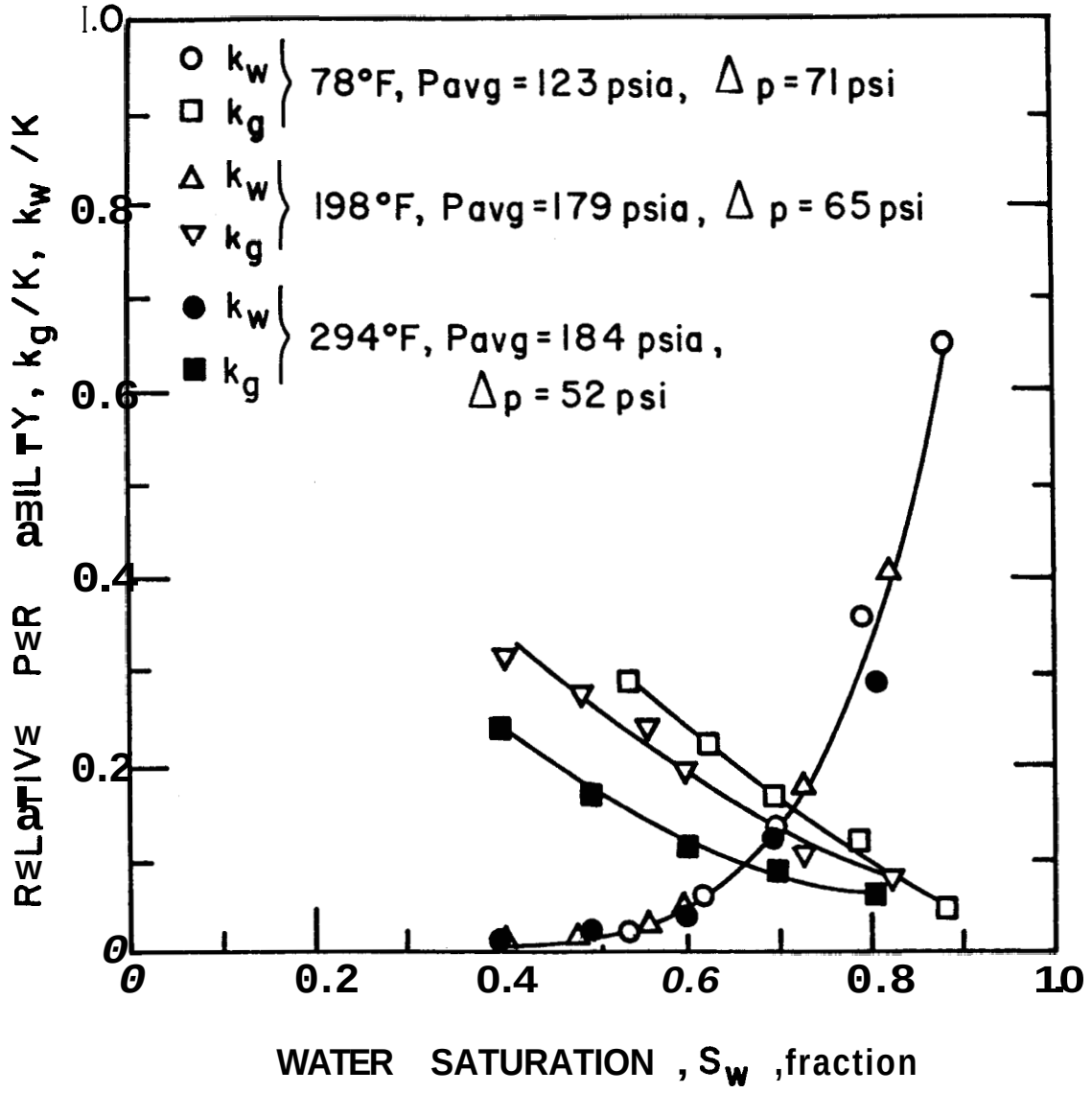

FIG. 6-22: GAS-WATER DRAINAGE, RELATIVE PERMEABILITY VS WATER SATURATION FOR SEVERAL TEMPERATURES USING RESULTS NOT CORRECTED FOR GAS VOLUME EXPANSION DUE TO WATER VAPORIZATION

The Fig. 6-22 gas relative permeabilities at 294°F would be increased by 12% if the viscosity of nitrogen (0.0228 cp) was used in Eq. 6-22b rather than the viscosity of a nitrogen-water vapor mixture (0.0204 cp). Figure 6-23 presents the calculated gas-water relative permeability data for the case where: (1) the gas viscosity used in Eq. 6-22b is that of nitrogen (not a nitrogen-water vapor mixture), and (2) there is no correction for gas expansion due to water vaporization. As mentioned earlier, no data in this report is corrected for water saturation reduction caused by water vaporization. Comparison with the corrected relative permeability curves in Fig. 6-18 shows that the correct gas relative permeability curves at various temperatures are close together at low water saturations. Thus, there appears to be no strong gas-water relative permeability temperature dependence in this synthetic core.

A related fluid behavior topic is the solubility of nitrogen in water. The next section demonstrates that the solubility changes far nitrogen-water systems are not significant for these experiments.

6.3.2.4 Nitrogen Solubility in Liquid Water

This section demonstrates why no allowance was made for changes in the nitrogen solubility of liquid water as a function of temperature and pressure. Before displacement begins, the core is completely saturated with partially degassed liquid water. The resulting equilibrium between injected gas and water may have a minor effect on water viscosity or water volume factor.

Henry's law for the solute nitrogen in the solvent water is:

$$p_p = x_{N_2} k_H \qquad (6\text{-}67)$$

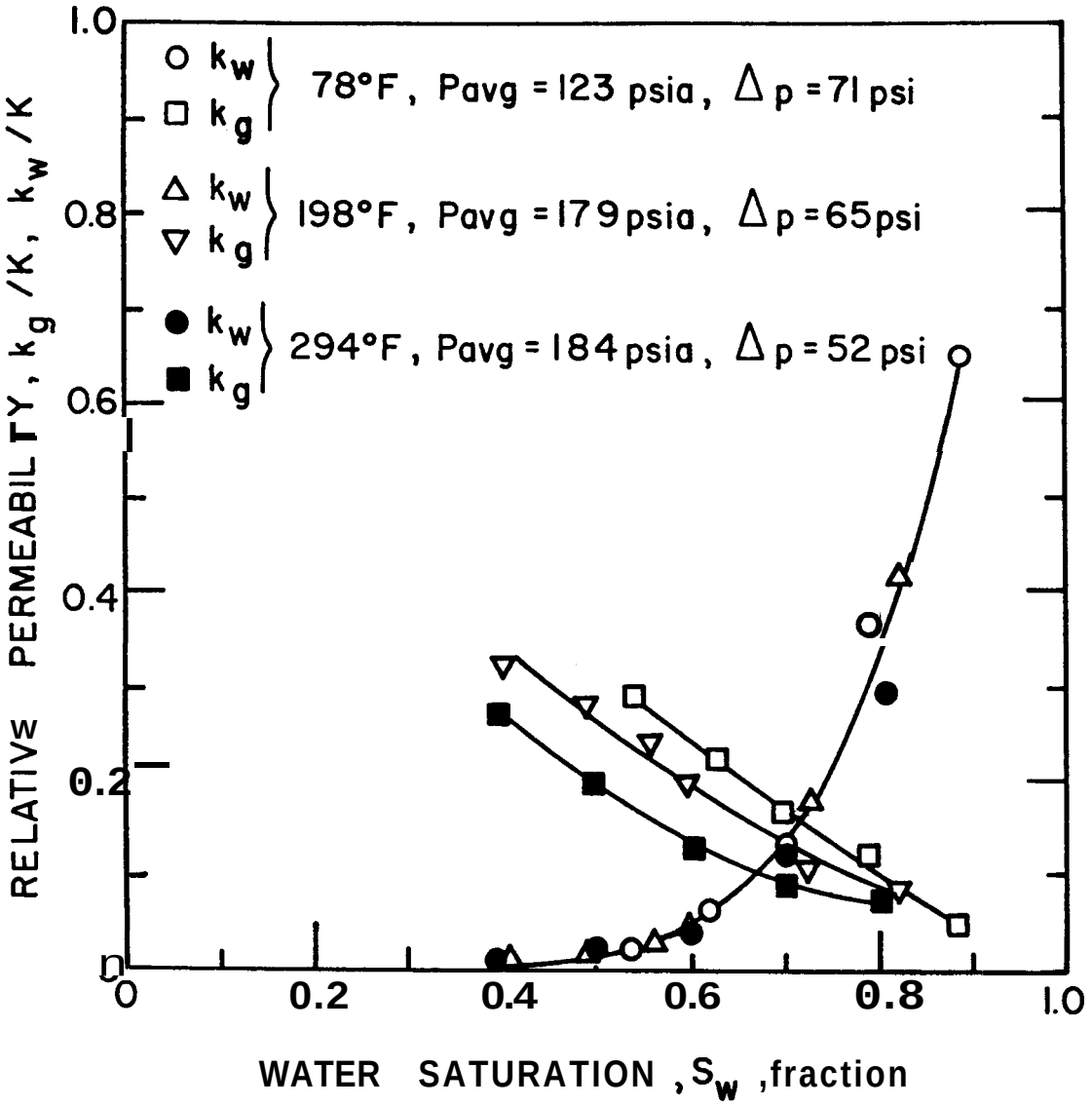

FIG. 6-23: GAS-WATER DRAINAGE RELATIVE PERMEABILITY VS WATER SATURATION USING: (1) THE VISCOSITY OF NITROGEN RATHER THAN A NITROGEN-WATER VAPOR MIXTURE, AND (2) RESULTS NOT CORRECTED FOR GAS VOLUME EXPANSION DUE TO WATER VAPORIZATION

where:

p_{pN_2} = partial pressure of nitrogen in vapor phase

x_{N_2} = mole fraction of nitrogen in liquid phase

k_H = Henry's law constant

For the case of maximum loss of nitrogen vapor phase to solution in the liquid water phase, assume zero nitrogen in the initial core water and nitrogen saturation at 70°F, 150 psia:

$$y_{H_2O} = \frac{p_{vp}}{p_T} = \frac{.363}{150} \approx 2.4\text{x}10^{-3} \frac{\text{mole } H_2O(v)}{\text{mole}(H_2O+N_2)(v)}$$

$$\therefore p_{pN_2} \approx p_T$$

$$x_{N_2} = \frac{p_{pN_2}}{k_H} = \frac{(150 \text{ psia}/14.7 \text{ psia/atm})}{8.5\text{x}10^4 \text{ atm/mol frac}} = 1.20\text{x}10^{-4} \frac{\text{mole } N_2}{\text{mole}(N_2+H_2O)}$$

Therefore, at 70°F (294.2°K) and 150 psia (10.2 atm):

$$\frac{\ell N_2}{\text{gm } H_2O} = \frac{x_{N_2}}{(1-x_{N_2})(18)} \frac{RT}{p}$$

$$= 1.58\text{x}10^{-5} \frac{\ell N_2}{\text{gm } H_2O} \qquad (6\text{-}68)$$

where:

R = 0.08207 (R atm)/(mol K°)

Even this maximum nitrogen loss effect is too small to include in the gas balance equations.

This concludes the discussion of important vapor-liquid equilibria effects. The next section presents an analysis of the importance of gravity segregation in the gas-drive experiments.

6.3.3 Gravity Segregation

The vertical separation of the vapor and liquid phases must be evaluated in two-phase flow experiments. The characteristic time ratio discussed earlier in this section and in the literature survey may be used to conclude that gravity segregation was probably not a major influence in these experiments:

$$\frac{t_v}{t_H} = \frac{L_v \Delta p}{L_H^2 \left[\frac{1}{\bar{v}_w} - \frac{1}{\bar{v}_g}\right]} \tag{6-69}$$

where:

$$\bar{v}_g = y_{N_2}\left[\frac{1}{\bar{v}_{N_2}}\right] + y_{H_2O}\left[\frac{1}{\bar{v}_{H_2O}}\right] \tag{6-70}$$

$$\bar{v}_{N_2} = \frac{RT}{Mp} \tag{6-71}$$

M = molecular weight

R = gas constant

T = absolute temperature

p = absolute pressure.

Experiments NW1, NW2, and NW3 had t_v/t_H values between 3 and 4, which means that vertical flow was much less important than horizontal flow.

The following section presents a brief evaluation of the capillary end effects.

6.3.4 Capillary End Effects

The repeatable results obtained at various pressures, pressure drops, and temperatures suggested that capillary end effects did not strongly influence the experimental data. Additional gas-drive runs for various pressure levels and pressure drops at a set temperature also suggested that end effects did not markedly influence the relative permeability curves shown in Fig. 6-18. With end effects, the calculated value for water relative permeability would be lower than for a run without end effects. The pressure drop across the core for the 78°F, 198°F, and 294°F runs shown in Fig. 6.3.1 was 71 psi, 65 psi, and 52 psi, respectively. The slightly lower water relative permeability values at higher temperatures (and lower pressure differences) when water saturation is in the 80-90% range may be caused in part by end effects.

Another laboratory phenomenon, Klinkenberg slip, is investigated in the next section.

6.3.5 Klinkenberg Slip

Klinkenberg slip, discussed in Section 2, was not considered in the analysis of the gas flow data. Figure 7 of Arihara (1974) suggests that the expected correction for slip at the high (8-12 atm) pressures used in this study would be fairly small. Ideally, the gas relative permeability curve should be lowered slightly to correct the minor slip effect. Amyx, Bass, and Whiting (1960) show that:

$$\frac{k_{uncorrected}}{k_{corrected}} = 1 - \frac{b}{p_m} \qquad (6\text{-}72)$$

where:

b = Klinkenberg slip factor

p_m = mean pressure

If b = 0.2 atm and p_m = 10 atm, then:

$$1 + \frac{b}{p_m} = \frac{k_{uncorrected}}{k_{corrected}} = 1.02$$

The above calculations are representative of the treatment of absolute permeability data. Slip effects for relative permeability data have been discussed in the literature survey and in the steam-water results sections. Rose *(1948)* showed that gas relative permeability can include slip by dividing the effective gas permeability by the absolute gas permeability determined at the same mean pressure. Correcting the water absolute permeability in this experiment by a factor of 1.02 is a negligible correction.

Davidson (1969) observed that the gas-oil permeability ratio, k_g/k_o, increased with increased temperature. Davidson believed this temperature dependence was caused by gas molecular slippage (Klinkenberg effect). Using either nitrogen or steam and Chevron USP Grade No. 15 white oil, Davidson did not consider the effect of gas volume expansion or gas-mixture viscosity change caused by the vaporization of oil.

Reasonable values can be estimated for oil vapor pressure and oil vapor viscosity. Assuming that vaporized oil does not condense while passing through the heat exchanger, the produced gas volumes measured may approximately represent the total gas (nitrogen + oil vapor) volume. The observed temperature dependence might be caused by a large

mole-fraction of low viscosity oil vapor in the gas stream at elevated temperatures. Additional study is required to support this explanation.

The next section summarizes a brief study of the effect of temperature on the absolute permeability to water of the consolidated synthetic sandstone core.

6.3.6 Effect of Temperature on Absolute Permeability

Although the results are not shown here, the water absolute permeability of the synthetic sandstone did not depend upon temperature in the range 70–300°F and at the low confining pressures used in this study. This result is in agreement with the results of Arihara (19'74) and Cassé (1976) in that minor permeability reductions with increased temperature have been observed at low confining pressures *(300–500* psig).

Additional experimental considerations and problems are presented in the next section.

6.3.7 Additional Considerations

Problems not considered in the preceding are core homogeneity, elastomer gas generation at high temperatures, and the possibility of turbulent flow.

Previous studies by Arihara (1974) and Chen (1976) with the artificial consolidated sandstone cores showed reasonable homogeneity with the same fabrication methods used in this study. However, sleeve gas generation was a major problem in Chen's study. Sleeve gas was not observed in the isothermal flow experiment because of the presence of nitrogen in the flowstream. Prior to nitrogen breakthrough, no noncondensible vapor bubbles were observed flowing through the outlet sight glass.

This lack of apparent gas generation in total liquid flow was expected because sleeve gas is primarily generated when the sleeve is in the :presence of steam.

At the end of the experimental runs, it was determined that the choice of core sleeve elastomer may affect core wettability. By observing water droplets placed on dry cores, it was concluded that unused synthetic cores, unused Berea cores, and synthetic cores used at elevated temperatures in ethylene propylene sleeves were more water wet than synthetic cores used at elevated temperatures in silicone rubber sleeves.

Finally, it is believed that gas phase turbulence was not important because, as shown in Fig. 6-18, there was no gas relative permeability lowering with increased pressure drop.

6.3.8 Future Improvements

Future experiments should be run to determine the effect of confining pressure on the temperature sensitivity of relative permeability. These experiments should be conducted with both synthetic and natural consolidated sandstones. Capillary pressure data should also be obtained for each sandstone.

Several improvements in the apparatus are also planned. The use of automatic regulating valves, an inlet flowrator, and the injection of nitrogen gas already saturated with water at core temperature and inlet pressure will help reduce the labor required to obtain and analyze the data from these experiments. A more durable, high pressure liquid-gas separator should also be designed and fabricated. It is also highly desirable to use elastomer confining sleeves or other materials that do not degas at high temperatures.

Finally, a study should be made to determine the extent of core anisotropy caused by: **(1)** steam-water hydrothermal alteration, *(2)* fines migration, and **(3)** fabrication technique.

We turn now to a comparison of the nonisothermal, steam-water relative permeability curves discussed in Section *6.2,* and the isothermal, gas-water relative permeability curves just presented in Section *6.3.*

6.4 Comparison of Internal (Nonisothermal) and External (Isothermal Drive Experimental Results

A comparison of the isothermal and nonisothermal relative permeability curves indicates that: **(1)** the high flow rate steam (nonisothermal, internal drive) relative permeability is less than the gas (isothermal, external gas drive) relative permeability for high water saturations, (2) the steam relative permeability appears to be greater than the gas (isothermal) relative permeability for the lowest water saturations examined, and *(3)* the water relative permeability for the nonisothermal, internal drive is less than the water relative permeability for the isothermal external gas drive.

One possible explanation for the difference between the steam and gas relative permeability curves is core anisotropy, as explained by Corey and Rathjens *(1956)* in Chapter *2.3.* A high permeability channel may exist along the length of the core axis at the probe guide - core boundary. The gas drive data would be influenced more by this possible anisotropy than the boiling flow (nonisothermal) data. The gas-drive data tends to indicate a low critical gas saturation (4%), which is in agreement with the Corey-Rathjens model. Unfortunately, the probe guide is required for the

boiling flow experiments unless a gamma ray or other external saturation measuring device is available.

A second possible explanation for the difference between steam and gas relative permeability curves is a difference in vapor saturation distribution.

In the case of the external gas drive, nitrogen would be expected to enter and flow through the largest pores first. As flow progresses, and the nitrogen and water vapor mixture saturation at a given cross-section increases, more of the gas enters smaller pores. As gas enters smaller pores, water would be displaced into the larger pores to flow through the core. Thus, some of the larger pores may become partially blocked with liquid water at high gas saturations.

In the case of the internal boiling drive, as the pressure is lowered, water vaporizes both in small and large pores. Vapor (steam) in the large pores, which dominates volumetric flow, represents only a part of the total vapor saturation. Although vapor may flow in smaller pores, there will be a great resistance to flow. This distribution effect could explain why the steam relative permeability is so low at low vapor saturations. However, as vaporization continues, the larger pores dominate flow and channel the vaporized water. The small, or high flow resistance, pores already have some vapor saturation (depending upon vapor pressure lowering) and evaporation may allow the transport of water molecules without significant blockage of vapor flow by liquid water. This last comment may explain the high steam relative permeabilities at high vapor saturations.

It is believed that the above explanation is a viable possibility despite the report of no difference in external and internal gas

drive relative permeabilities by Stewart et al. (1953). In many of the petroleum industry internal gas drive studies, only one of several components vaporize. Much of the original fluid remains liquid. In this boiling flow study, a single component fluid, water, was used. Thus, liquid-vapor interference in porous media may be different for a single component fluid than for a multi-component fluid.

One other difference between the isothermal and nonisothermal experiments lies in the method of determining water saturation. Water saturation in the isothermal external gas-drive experiments was obtained by material balance calculations. Water saturation for the nonisothermal boiling flow experiments was obtained with the capacitance probe. As discussed earlier in Section 6.2, when radial heat transfer dominates in the vaporization process, measured water saturations may be lower than actual average values due to the distribution of water vapor in the core cross-section normal to the axis. At high water saturations in the three nonisothermal experiments, the more radial heat gain dominated the results, the higher the steam relative permeability.

Thus, the high steam relative permeabilities should probably be graphed at higher gas saturations or lower water saturations. This would bring the results of the low flow rate runs, SW1 and SW2, into closer agreement with the high flow rate run, SW3. Correcting the nonisothermal results for these complex heat transfer effects would also help support the explanation for the difference between the isothermal and nonisothermal experimental results. Of course, a nonhomogeneous radial variation in steam saturation is not considered in the interpretation of data. The point is that the less the radial heat transfer dominates the steam saturation, the greater the difference between nonisothermal and isothermal experimental results.

This concludes the discussion of the results of this experimental study. The next section presents the conclusions drawn from the study of the capacitance saturation probe, steam-water relative permeability, and gas-drive relative permeability at elevated temperatures.

7. RESULTS AND CONCLUSIONS

The conclusions of this study concern two major studies: calibration and evaluation of the capacitance probe for liquid detection, and relative permeability determination. Thus the results of these studies will be discussed under the topics: (1) capacitance probe calibration data, (2) analysis of the steam-water flow data, (3) analysis of the nitrogen-water flow data, and (4) comparison of the internal drive steam-water flow data and the external gas-drive nitrogen-water flow data. The conclusions drawn from the relative permeability experiments apply only to the synthetic cores used in this study. However, it is believed that similar results will be obtained for natural sandstone cores.

7.1 Capacitance Probe Calibration

The capacitance probe, using the 7.5 MHz, Baker-type electronics developed by Chen (1976), is useful for measuring water saturations when a wide range of saturations is encountered ($0 < S_w < 1$).

Using a Q-meter in the kHz range, the capacitance probe is useful for measuring water saturation when only low saturations are encountered.

The apparent accuracy of water saturation measurements using t'he capacitance probe calibration curves is about ±10% pore volume.

7.2 Steam-Water Flow Data Conclusions

Axial conduction and radial heat transfer are important to the vaporization process at low flow rates for the apparatus used in this study.

Radial heat transfer may cause the measured vapor saturation at the core axis to be less than the actual cross-sectional average vapor saturation for low flow rates.

Steam-water, drainage, boiling flow relative permeability curves appear to be rate dependent for the apparatus used in this study. The rate dependence may be caused by complex heat and mass transfer phenomena. This rate effect is related to the radial heat gain which tends to dominate vaporization at low flow rates.

7.3 Nitrogen-Water Flow Data Conclusions

External gas drive, nitrogen-water, drainage relative permeabilities are not a strong function of temperature for water saturations ranging from 0.4 to 0.9 fraction of pore volume.

External gas-drive relative permeability calculations must include the elevated temperature effects of liquid vaporization on gas-mixture volume and viscosity. A new displacement theory which includes vaporization was developed in this study. Liquid vaporization may have been a factor in the gas-oil permeability ratio temperature dependence reported by Davidson (1969).

External gas-drive relative permeability calculations may require correction for liquid saturation reduction due to vaporization at high temperatures, low pressures, and at large gas injection volumes.

External gas-drive relative permeability experiments can be run using a high-pressure gas liquid separator. It was found to be easier to regulate the flow of two single-phase fluids than one two-phase fluid mixture.

7.4 Comparison of Internal and External Drive Flow Data

Gas relative permeability values at high water saturations for boiling nonisothermal flow are lower than gas relative permeabilities for the external gas-drive methods for isothermal flow. This result may be caused by the different positions occupied by gas within the porous media for the two processes.

The water relative permeability curves are higher at high water saturations for the external gas drives than for the boiling drive.

8. NOMENCLATURE

ENGLISH

A = cross-sectional area perpendicular to flow

b = Klinkenberg slip factor

C = capacitance in oscillating circuit

C_s = C measured in **100%** steam-saturated core

C_w = C measured in **100%** water-saturated core

C^* = normalized capacitance, $(C_s-C)/(C_s-C_w)$

D = core diameter

f = flowing gas **mass** fraction (gas **mass** fraction of gas-liquid mixture passing a point in unit time)

f_g = flowing gas volume fraction

f_{g1} = flowing gas volume fraction at point **1** in core

f_{g2} = flowing gas volume fraction at core outlet

f'_g = df_g/dS_g

f_r = resonant frequency in oscillating circuit

f_{rs} = f_r in **100%** steam-saturated core

f_{rw} = f_r in **100%** water-saturated core

f_r^* = normalized frequency, $(f_{rs}-f_r)/(f_{rs}-f_{rw})$

f_{w2} = flowing water volume fraction

$\overline{f}$ = gas **mass** fraction in a given section at a given time

F_s = steam permeability reduction factor (relative permeability) as used by Grant (1977)

F_w = water permeability reduction factor (relative permeability) as used by Grant (1977)

g = acceleration due to gravity

G_{inj} = cumulative gas injection into core

G_{sep} = cumulative gas production from core as measured downstream of separator

h = fluid enthalpy

h_g = gas enthalpy

h_{in} = enthalpy of injected fluid

h_ℓ = liquid enthalpy

$h_{\ell g}$ = difference in enthalpy between gas and liquid

k_ℓ = effective permeability to liquid

k_g = effective permeability to gas

k_H = Henry's Law constant

k = effective permeability to liquid

k_{rg} = gas relative permeability

k_{rg}' = gas relative permeability calculated neglecting gas valume expansion due to water vaporization

$k_{r\ell}$ = liquid relative permeability

k_{rw} = water relative permeability

k_{rw}' = water relative permeability calculated neglecting gas volume expansion due to water vaporization

k_x = effective permeability in the x direction

k_y = effective permeability in the y direction

$(k/\mu)_H$ = horizontal mobility

$(k/\mu)_V$ = vertical mobility

K = absolute permeability

L = core length

L_c = inductance in oscillating circuit

L_H = horizontal characteristic length

L_V = vertical characteristic length

m = mass of fluid in core

m_i = initial mass of fluid in core

m_s = mass of steam in core

m_w = mass of water in core

M = molecular weight

N_R = Reynolds Number

P = pressure

Pavg = arithmetic average of inlet and outlet core absolute pressures

p_{bar} = absolute barometric pressure

p_c = capillary pressure, $p_g - p_\ell$

p_g = gas pressure

p_{in} = inlet pressure

p_ℓ = liquid pressure

p_m = absolute mean pressure in gas phase

p_p = partial pressure of component

p_{vp} = vapor pressure

p_T = total pressure

P = perimeter around core, $2\pi \cdot$radius of cylindrical core

q = gas flow rate

q_H = heat flow rate

q_i = injection rate divided by cross-sectional area

q_t = total volumetric flow rate

$(q\mu/\Delta p)_b$ = product of flow rate, viscosity, and reciprocal pressure drop for single-phase flow of a "base" fluid through a core

Q_i = cumulative gas injection into core expressed in pore volumes

R = universal gas constant

R_g = effective gas permeability normalized to effective gas permeability at the residual liquid saturation

R_ℓ = effective liquid permeability normalized to the absolute liquid permeability

S_g = gas volumetric saturation, fraction pore volume

S_{gc} = critical gas saturation

S_{gi} = initial gas saturation

S_{g2} = gas saturation at outlet end of core

$\bar{S}_g$ = average gas saturation in core

S_ℓ = liquid volumetric saturation, fraction pore volume

$S_{\ell r}$ = residual liquid saturation

S_ℓ^* = normalized liquid saturation, $(S_\ell - S_{\ell r})/(1 - S_{gc} - S_{\ell r})$

S_m = extrapolated endpoint saturation when $k_{rg} = 0$

= oil saturation

S_w = water volumetric saturation, fraction pore volume

S_{wi} = irreducible water saturation

$\bar{S}_w$ = average water saturation in core

S_w^* = normalized water saturation, $(S_w - S_{wi})/(1 - S_{gc} - S_{wi})$

t = time

t_H = characteristic time to travel characteristic horizontal length

t_V = characteristic time to travel characteristic vertical length

T = temperature

T_∞ = temperature of air bath environment surrounding coreholder

u_g = gas microscopic velocity

u_H = horizontal characteristic velocity

u_ℓ = liquid microscopic velocity

u_V = vertical characteristic velocity

U = overall heat transfer coefficient for cylindrical core

$\bar{v}_g$ = gas specific volume

$\bar{v}_\ell$ = liquid specific volume

$\bar{v}_s$ = steam specific volume

$\bar{v}_w$ = water specific volume

V_{N_2} = cumulative volume of N_2 injected at core conditions

V_P = pore volume

w = total weight rate of flow

w_g = gas weight rate of flow

w_ℓ = liquid weight rate of flow

w_o = 100%liquid water flow rate taken from a graph of log wellbore discharge rate vs discharge enthalpy (Grant, 1977)

W_P = cumulative water produced from core through separator

x = horizontal distance

x_{dry} = hypothetical distance from the inlet that a dry region, caused by water vaporization, extends into the core

x_{H_2O} = mole fraction H_2O in liquid phase

x_{N_2} = mole fraction N_2 in liquid phase

x_2 = horizontal distance to core outlet

Y = vertical distance

y_{H_2O} = mole fraction H_2O in vapor phase

y_{N_2} = mole fraction N_2 in vapor phase

z = real gas compressibility factor

GREEK

A = difference

X = thermal conductivity

X_C = pore size distribution index used in Corey-type equations

λ_2^{-1} = relative reciprocal mobility at core outlet

λ^{-1} = average relative reciprocal mobility in core

μ_g = gas viscosity

$\mu_{H_2O(g)}$ = water vapor viscosity

μ_ℓ = liquid viscosity

μ_{N_2} = nitrogen viscosity

μ_o = oil viscosity

μ_s = steam viscosity

μ_w = water viscosity

ρ = fluid density

ϕ = porosity, interconnected pore volume fraction of bulk volume

Φ = saturation probe signal

Φ_s = Φ measured in 100%steam-saturated core

Φ_w = Φ measured in 100%water-saturated core

Φ^* = normalized probe signal, $(\Phi_s-\Phi)/(\Phi_s-\Phi_w)$

ARRREVIATIONS

kH_z = kilohertz, 10^3 cycles per second

MH_z = megahertz, 10^6 cycles per second

pf = picofarad, 10^{-12} farad

9. REFERENCES

Adivarahan, P.: "Heat Transfer in Consolidated Porous Media with Flowing Fluids," Ph.D. Dissertation, Northwestern University, Evanston, Illinois, 1961.

Adivarahan, P., Kunii, D., and Smith, J.M.: "Heat Transfer in Porous Rocks through which Single-phase Fluids are Flowing," Soc. Pet. Eng. J. (Sept. 1962), 290-296.

Amyx, J., Bass, D., Jr., and Whiting, R.L.: Petroleum Reservoir Engineering, Physical Properties, New York: McGraw-Hill Book Co., 1960.

Anand, J., Somerton, W.H., and Gomaa, E.: "Prediction of Thermal Properties of Formations from Other Known Properties," SPE Paper No. 4171, presented at the 43rd Annual California Regional Meeting, SPE of AIME, Bakersfield, CA, Nov. 8-10, 1972.

Anderson, A.B.C.: "A Method of Determining Soil Moisture Content Based on the Variation of the Electrical Capacitance of Soil, at a Low Frequency, with Moisture Content," Soil Science (1943), 29-41.

Arihara, N.: "A Study of Nonisothermal Single and Two-Phase Flow through Consolidated Sandstones," Ph.D. Dissertation, SGP-TR-2, Stanford University, Nov. 1974.

Arihara, N., Ramey, H.J., Jr., and Brigham, W.E.: "Nonisothermal Single- and Two-Phase Flow through Consolidated Sandstones," Soc. Pet. Eng. J. (June 1976), 137-146.

Aruna, M.: "The Effects of Temperature and Pressure on Absolute Permeability of Sandstones," Ph.D. Dissertation, SGP-TR-13, Stanford University, May 1976.

Atkinson, P.G., and Ramey, H.J., Jr.: "Problems of Heat Transfer in Porous Media," SPE Paper No. 6792, presented at the 52nd Annual Fall Meeting, SPE of AIME, Denver, Colorado, Oct. 9-12, 1977.

Atkinson, P.G.: "Numerical Simulation of Two-Phase Boiling Flow in a Linear Horizontal Porous Medium," SGP-TR-18, Stanford University, Dec. 1975.

Brownell, D.H., Jr., Garg, S.K., and Prichett, J.W.: "Governing Equations for Geothermal Reservoirs," Water Resources Research (Dec. 1977), 13, No. 6, 929-934.

Cassé, F.J., and Ramey, H.J., Jr.: "The Effect of Temperature and Confining Pressure on Single Phase Flow in Consolidated Rocks, SPE Paper No. 5877, presented at the 46th Annual California Regional Meeting, SPE of AIME, Long Beach, CA, Apr. 8-9, 1976.

Chen, H.K.: "Measurement of Water Content in Porous Media under Geothermal Fluid Flow Conditions," Ph.D. Dissertation, SGP-TR-15, Stanford University, Nov. 1976.

Chicoine, S.D., Strobel, C.J., and Ramey, H.J., Jr.: "Vapor Pressure Lowering in Two-Phase Geothermal Systems," SPE Paper No. 6767, presented at the 52nd Annual Fall Technical Conference, SPE of AIME, Denver, CO, Oct. 9-12, 1977.

Corey, A.T.: Mechanics of Heterogeneous Fluids in Porous Media, Fort Collins, Colorado: Water Resources Publications, 1977.

Corey, A.T., and Rathjens, C.H.: "Effect of Stratification on Relative Permeability," Trans., AIME (1956), 207, 358-360.

Corey, A.T., Rathjens, C.H., Henderson, J.H., and Wyllie, R.J.: "Three-Phase Relative Permeability," Trans., AIME (1956), 207, 349-351.

Corey, A.T.: "The Interrelation between Gas and Oil Relative Permeabilities," Producers Monthly, (Nov. 1954), 19, 38-41.

Craig, F.F., Sanderlin, J.L., Moore, D.W., and Geffen, T.M.: "A Laboratory Study of Gravity Segregation in Frontal Drives," Trans., AIME (1957), 210, 275-282.

Craig, F.F., Jr.: The Reservoir Engineering Aspects of Waterflooding, Monograph Series, Society of Petroleum Engineers of AIME, Dallas (1971), 3.

Crichlow, H.B.: Modern Reservoir Engineering--A Simulation Approach, Englewood Cliffs, New Jersey: Prentice-Hall, Inc., 1977.

Crookston, R.B., Culham, W.E., and Chen, W.H.: "Numerical Simulation Model for Thermal Recovery Processes," SPE Paper No. 6724, presented at the 52nd Annual Fall Meeting, SPE of AIME, Denver, CO, Oct. 9-12, 1977.

Culham, W.E., Farouq Ali, S.M., and Stahl, C.D.: "Experimental and Numerical Simulation of Two-Phase Flow with Interphase Mass Transfer in One and Two Dimensions," Soc. Pet. Eng. J. (Sept. 1969), 323-337.

Davidson, L.B .: "The Effect of Temperature on the Permeability Ratio of Different Fluid Pairs in Two-Phase Systems," J. Pet. Tech. (Aug. 1969), 1037-1046.

Donaldson, I.G.: "The Flow of Steam Water Mixtures through Permeable Beds: A Simple Simulation of a Natural Undisturbed Hydrothermal Region," N.Z .J. Sci. (1968), 11, 3.

Electrical Research Association: 1967 Steam Tables, New York: St. Martin's Press, 1967.

Evers, J.F., Preston, F.W., Sadiq, S., and Swift, G.W.: "Preparation and Testing of Low Permeability Porous Media to Meet Scaling Requirements for Gas Reservoir Modeling," Soc. Pet. Eng. J. (June 1967), 189.

Farouq Ali, S.M.: Basic Design of Thermal Recovery Projects, Department of Petroleum and Natural Gas Engineering, The Pennsylvania State University, University Park, Pennsylvania, 1968.

Farouq Ali, S.M.: Oil Recovery by Steam Injection, Bradford, Pennsylvania: Producers Publishing Company, Inc., 1970.

Faust, C.R., and Mercer, J.W.: "Mathematical Modeling of Geothermal Systems," presented at the Second United Nations Symposium on the Development and Use of Geothermal Resources, San Francisco, CA, May 19-29, 1975.

Frick, T.C. (ed.): Petroleum Production Handbook, 11, Dallas, Texas: Society of Petroleum Engineers, 1962.

Fulton, P.F.: "The Effect of Gas Slippage on Relative Permeability Measurements," Prod. Monthly (Oct. 1951), 15, No. 12, 14-19.

Garg, S.K., Pritchett, J.W., and Brownell, D.H., Jr.: "Transport of Mass and Energy in Porous Media," presented at the Second United Nations Symposium on the Development and Use of Geothermal Resources, San Francisco, CA, May 19-29, 1975.

Geffen, T.M., Owens, W.W., Parrish, D.R., and Morse, R.A.: "Experimental Investigation of Factors Affecting Laboratory Relative Permeability Measurements," Trans., AIME (1951), 192, 99-110.

Gomaa, E.E., and Somerton, W.H.: "Thermal Behavior of Multifluid-Saturated Formations, Part I: Effect of Wettability, Saturation, and Grain Structure," SPE Paper No. 4896-A, presented at the 44th California Regional Meeting, SPE of AIME, San Francisco, CA, Apr. 4-5, 1974.

Gomaa, E.E., and Somerton, W.H.: "Thermal Behavior of Multifluid-Saturated Formations, Part 11: Effect of Vapor Saturation - Heat Pipe Concept and Apparent Thermal Conductivity," SPE Paper No. 4896-B, presented at the 44th California Regional Meeting, SPE of AIME, San Francisco, CA, Apr. 4-5, 1974.

Goode, P., Shell Development Co., Houston, Texas: private communication, 1978.

Gould, T.L. : "Vertical Two-Phase Steam-Water Flow in Geothermal Wells," J. Pet. Tech. (Aug. 1974), 833-842.

Grant, M.A. : "Permeability Reduction Factors at Wairakei," AIChE-ASME Heat Transfer Conference, Salt Lake City, Utah, Aug. 15-17, 1977.

Heath, L.J.: "Variations in Permeability and Porosity of Synthetic Oil Reservoir Rock--Method of Control," Soc. Pet. Eng. J. (Dec. 1965), 329.

Herkelrath, W.N.: "The 'Heat-Pipe' Effect in Vapor-Dominated Geothermal Systems," Proc., Third Workshop on Geothermal Reservoir Engineering, P. Kruger and H.J. Ramey, Jr. (Eds.), Stanford University, Dec. 14-16, 1977.

Hill, N.E., Vaughn, W.E., Price, A.H., and Davies, M.: Theoretical Treatment of Permittivity and Loss, London: Van Nostrand Reinhold Co., 1969.

Home, R.N., and Ramey, H.J., Jr.: "Steam/Water Relative Permeabilities from Production Data," Proc., 1978 Geothermal Resources Council Annual Meeting, Hilo, HA, July 25-27, 1978.

Hsieh, C.H., and Ramey, H.J., Jr.: "An Inspection of Experimental Data on Vapor Pressure Lowering in Porous Media," Proc., 1978 Geothermal Resources Council Annual Meeting, Hilo, HA, July 25-27, 1978.

Johnson, C.E., Jr.: "A Two-Point Graphical Determination of the Constants S_{Lr} and S_m in the Corey Equation for Gas-Oil Relative Permeability Ratio, : J. Pet. Tech. (Oct. 1968), 1111-1113.

Johnson, E.F., Bossler, D.P., and Naumann, V.O.: "Calculation of Relative Permeability from Displacement Experiments," Trans., AIME (1959), 216, 370-372.

Jones, S.C., and Roszelle, W.O.: "Graphical Techniques for Determining Relative Permeability from Displacement Experiments," SPE Paper No. 6045, presented at the 51st Annual Fall Meeting, SPE of AIME, Denver, CO, Oct. 3-6, 1976.

Katz, D.L., Cornell, D., Kobayashi, R., Poettmann, F.H., Vary, J.A., Elenbaas, J.R., and Weinaug, C.F.: Handbook of Natural Gas Engineering, New York: McGraw-Hill Book Company, 1959.

Kellar, G.V., and Licastro, P.H.: "Dielectric Constant and Electrical Resistivity of Natural State Cores," U.S. Geol. Survey Bull. 1052H (1959), 257-286.

Klinkenberg, L.J.: "The Permeability of Porous Media to Liquids and Gases," API Drill. and Prod. Prac. (1941), 200-213.

Laws, V., and Sharpe, R.W.: "The Response of an H.F. Moisture Probe to Soluble Salts," Brit. J. Appl. Phys.-J. Phys. D. (1969), 2, 1293-1300.

Kruger, P., and Ramey, H.J., Jr.: "Stimulation and Reservoir Engineering of Geothermal Resources," SGP-TR-1, Stanford University, June 1974.

Kyte, J.R., and Rapoport, L.A.: "Linear Waterflood Behavior and End Effects in Water-Wet Porous Media," Trans., AIME (1958), 213, 423-426.

Lone Star Lafarge Company: "Properties and Uses of Fondu Calcium Aluminate Cement" and "Refractory Applications of Fondu Calcium Aluminate Cement," P.O. Box 448, 977 Norfolk Square, Norfolk, Virginia, 23501.

Martin, J.C.: "Analysis of Internal Steam Drive in Geothermal Reservoirs," J. Pet. Tech. (Dec. 1975), 1493-1499.

Meador, R.A., and Cox, P.T.: "Dielectric Constant Logging, A Salinity Independent Estimation of Formation Water Volume," SPE Paper No. 5504, presented at the 50th Annual Fall Meeting, SPE of AIME, Dallas, Texas, Sept. 28-Oct. 1, 1975.

Mercer, J.W., and Faust, C.R.: "Simulation of Water and Vapor Dominated Hydrothermal Reservoirs," SPE Paper No. 5520, presented at the 50th Annual Fall Meeting, SPE of AIME, Dallas, Texas, Sept. 28-Oct. 1, 1975.

Mickley, H.S., Sherwood, T.K., and Reed, C.E.: Applied Mathematics in Chemical Engineering, 2nd Edition, New York: McGraw-Hill Book Co., 1957, 54.

Miller, F.G., and Seban, R.A.: "Technical Note 319: The Conduction of Heat Incident to the Flow of Vaporizing Fluids in Porous Media," J. Pet. Tech. (Dec. 1955), 45-47.

Miller, F.G.: "Steady Flow of Two-Phase Single Component Fluids Through Porous Media," Trans., AIME (1951), 192, 205-216.

Moench, A.F., and Herkelrath, W.N.: "The Effect of Vapor-Pressure Lowering upon Pressure Drawdown and Buildup in Geothermal Steam Wells," Proc., 1978 Geothermal Resources Council Annual Meeting, Hilo, HA, July 25-27, 1978.

Moench, A.F.: "Simulation of Steam Transport in Vapor-Dominated Geothermal Reservoirs," Open File Report: 76-607, USGS, Menlo Park, CA, 1976.

Osoba, J.S., Richardson, J.G., Kerver, J.K., Hafford, J.A., and Blair, P.M.: "Laboratory Measurements of Relative Permeability," Trans., AIME (1951), 192, 47-56.

Owens, W.W., Parrish, D.R., Lamoreaux, W.E.: "An Evaluation of a Gas Drive Method for Determining Relative Permeability Relationships," Trans., AIME (1956), 207, 275-280.

Parkhomenko, E.: Dielectric Properties of Rocks, edited and translated from the Russian by G.V. Keller, New York: Plenum Press, 1967.

Poston, S.W., Ysrael, S., Hossain, A.K.J.S., Montgomery, E.F., 111, and Ramey, H.J., Jr.: "The Effect of Temperature on Irreducible Water Saturation and Relative Permeability of Unconsolidated Sands," Soc. Pet. Eng. J. (June 1970), 171-180.

Rapoport, L.A., and Leas, W.J.: "Properties of Linear Waterfloods," Trans., AIME (1953), 198, 139-148.

Rapoport, L.A.: "Scaling Laws for Use in Design and Operation of Water-Oil Flow Models," Trans., AIME (1955), *, 143-150.

Reid, R.C., Prausnitz, J.M., and Sherwood, T.K.: The Properties of Gases and Liquids, 3rd Edition, New York: McGraw-Hill Book Co., 1977.

Richardson, J.G., and Perkins, F.M., Jr.: "A Laboratory Investigation of the Effect of Rate on Recovery of Oil by Water Flooding," Trans., AIME (1957), 210, 114-121.

Rose, W.D.: "Permeability and Gas-Slippage Phenomena," API Drill. and Prod. Prac. (1948), 209-217.

Scheidegger, A.: The Physics of Flow Through Porous Media, Third Edition, Canada: University of Toronto Press, 1974.

Shinohara, K.: "Calculation and Use of Steam/Water Relative Permeabilities in Geothermal Reservoirs," M.S. Report, Stanford University, June 1978.

Sinnokrot, A.A., Ramey, H.J., Jr., and Marsden, S.S., Jr.: "Effect of Temperature Level upon Capillary Pressure Curves," Soc. Pet. Eng. J. (Mar. 1971), 13-22.

Smyth, C.P.: Dielectric Behavior and Structure, New York: McGraw-Hill Book Co., Inc., 1955.

Staggs, H.J., and Herbeck, E.F.: "Reservoir Simulation Models--An Engineering Overview," J. Pet. Tech. (Dec. 1971), 1428-1436.

Standing, M.B .: "Notes on Relative Permeability Relationships," Lecture Notes, Petroleum Engineering Department, Stanford University, CA, 1975.

Stewart, C.R., Craig, F.F., Jr., and Morse, R.A.: "Determination of Limestone Performance Characteristics by Model Flow Tests," Trans., AIME (1953), 198, 93-102.

Thomas, A.M.: "In Situ Measurement of Moisture in Soil and Similar Substances by 'Fringe' Capacitance," J. Sci. Instrum. (1966), S, 21-27.

Thomas, L.K., and Pierson, R.G.: "Three Dimensional Geothermal Reservoir Simulation," Soc. Pet. Eng. J. (Apr. 1978), 151-161.

Toronyi, R.M. : "Two-Phase, Two-Dimensional Simulation of a Geothermal Reservoir and the Wellbore System," Ph.D. Dissertation, Pennsylvania State University, Nov. 1974.

Trimble, A.E., and Menzie, D.E. : "Steam Mobility in Porous Media," SPE Paper No. 5571, presented at the 50th Annual Fall Meeting, SPE of AIME, Dallas, Texas, Sept. 28-Oct. 1, 1975.

van Beek, L.K.H. : "Dielectric Behaviour of Heterogeneous Systems," Progress in Dielectrics, 7, J.B. Birks (Ed.), Cleveland, Ohio: Rubber Co. Press, 1967.

Weinbrandt, R.M., Ramey, H.J., Jr., and Cassé, F.J.: "The Effect of Temperature on Relative Permeability of Consolidated Rocks," Soc. Pet. Eng. J. (Oct. 1975), 376.

Welge, H.J.: "A Simplified Method for Computing Oil Recovery by Gas or Water Drive," Trans., AIME (1952), 195, 91-98.

Wygal, R.J.: "Construction of Models that Simulate Oil Reservoirs," Soc. Pet. Eng. J. (Dec. 1963), 281.

APPENDIX 1: EQUIPMENT MANUFACTURERS AND SUPPLIERS

The equipment manufacturers and/or suppliers are listed below. Much of the equipment used in this study was modified by or designed and constructed with the help of Peter Gordon, Jon Grim, and Paul Petit. The Hassler-type coreholder was constructed from a design furnished by S.C. Jones, of the Marathon Oil Company.

1. Air Bath - NAPCO, Model 430
   Van Waters & Rogers
   Redwood City, CA (369-5561)

2. Tubular Furnace - Model 1027
   Varian
   Palo Alto, CA (493-4000)

3. Pump - Model R121A
   Milton Roy
   San Mateo, CA (341-8796)

4. Accumulator - Greerolator Model 20-15TMR-S-1/2WS
   Hydraulic Controls Inc.
   Emeryville, CA (658-8300)

5. Temperature Recorder - Model Speedomax W Multi-Point Recorder
   Leeds & Northrup Co.
   San Mateo, CA (349-6656)

6. Pressure Recorder - Model EU-20W
   Heathkit Electronic
   Redwood City, CA (365-8155)

7. Flowrator
   Fischer & Porter Co.
   Walnut Creek, CA (933-8880)

8. Temperature Controller - Model 61329-054
   Van Water & Rogers
   Redwood City, CA (369-5561)

9. Pressure Transducer - Model KP15, Celesco Industries
   GADO Instrument Sales
   Mountain View, CA (961-2222)

10. Pressure Indicator - Model CD25, Celesco Industries
    GADO Instrument Sales
    Mountain View, CA (961-2222)

11. Pressure Gage - AMETEK, Model P1536, Helicoid, Model KMonel 460
Jensen Instrument Co.
So. San Francisco, CA (589-9720)

12. Pressure Regulator, Model 2-580
Matheson Gas Products
Newark, CA (793-2559)

13. Sheathed Thermocouple, Thermocouple Wire
Claud S. Gordon Co.
San Carlos, CA (591-7070)

14. Valve, Fitting, Filter - Swagelok, NUPRO, WHITEY
Van Dyke Valve & Fitting
Sunnyvale, CA (734-3145)
Conax Instrument Laboratory
Palo Alto, CA (328-1040)

15. Pipe, Tubing
Tubesales
San Francisco, CA (922-2240)

16. 0-Ring
McDowell & Co.
Hayward, CA (785-7744)

17. Viton Core Sleeve - Viton A Tubing
West American Rubber Co.
Orange, CA (714- 532-3355)

18. Core - Berea Sandstone Core
The Cleveland Quarries Co.
Amherst, Ohio (216- 986-4501)

19. Digital Multimeter - Fluke 8000A
Fluke Western Technical Center
Santa Clara, CA (244-1505)

20. Stainless Steel - Pyrex Tubular Seals
Larson Electronic Glass
Redwood City, CA (369-6734)

21. Fondu Calcium Aluminate Cement
San Francisco Materials Co.
San Francisco, CA (282-0133)

22. Silicone Rubber Core Sleeve
Alasco Rubber and Plastic Corp.
Burlingame, CA (697-1420)

23. Ottowa Silica Sand
Smith Industrial Supply Co.
San Francisco, CA (822-3600)

24. Teflon Tubing - Zero Gage, Thin-Walled
Cadillac Plastic and Chemical Co.
So. San Francisco, CA (589-1833)

25. Q-Meter - Model 4342-A
    Continental Rentals
    Santa Clara, CA (735-8300)

26. 20-30 Grade Silica Sand - Unisil - 50 lb net
    Unisil Corp.
    Gopher State Silica Div.
    Le Soeur, Minn. 56058

27. Wet Test Meter
    Precision Scientific Co.
    VWR Scientific
    San Francisco, CA (469-0100)

APPENDIX 2: CAPACITANCE PROBE DETAILS

Figures A2-1 through A2-5 present details of capacitance probe equipment similar to that used in this study. The figures were taken from Arihara (1974) and Chen (1976), and additional details are found in their reports. The original design of the probe and the detection circuits were furnished by Dr. Paul Baker through the courtesy of the Chevron Oil Field Research Company, La Habra, California.

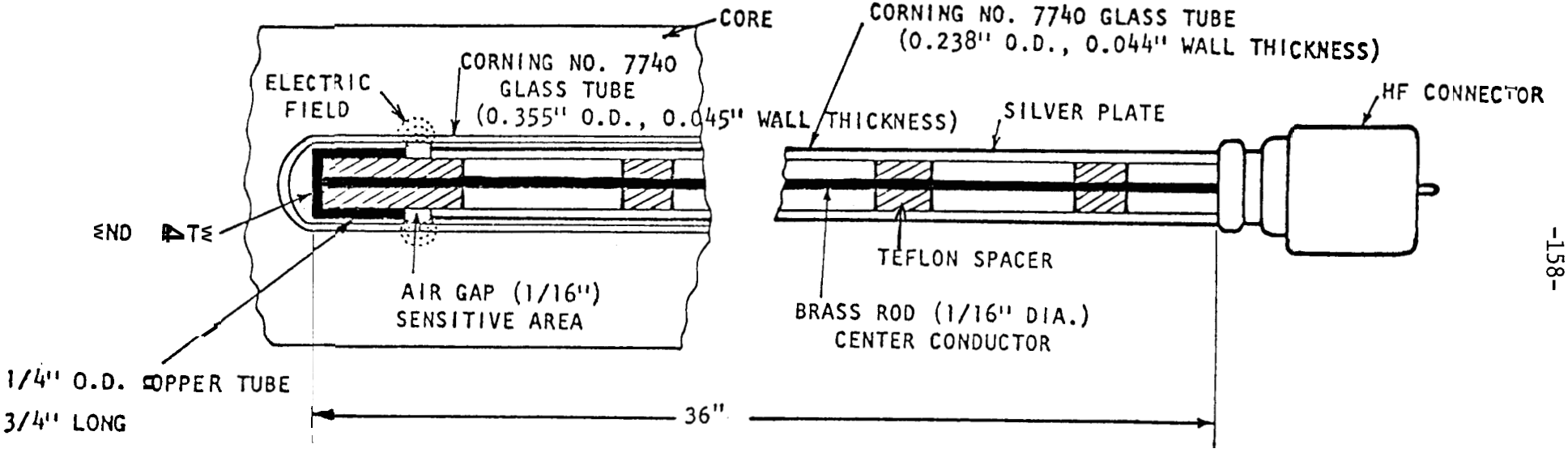

F . A2-1: CAPACITANCE PROBE USED TO MEASURE WATER SATURATION (ARIHARA, 1974)

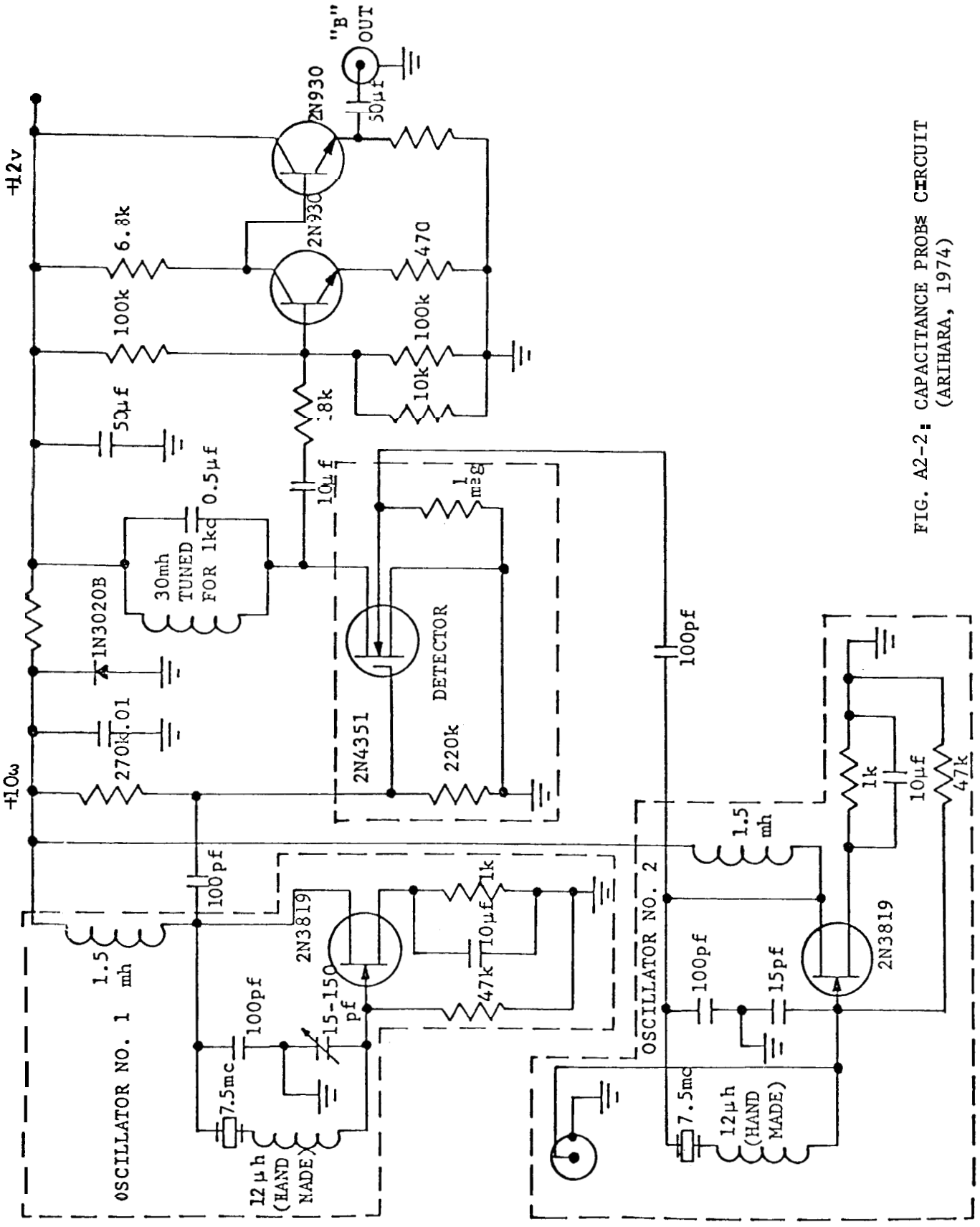

FIG. A2-2: CAPACITANCE PROBE CIRCUIT (ARIHARA, 1974)

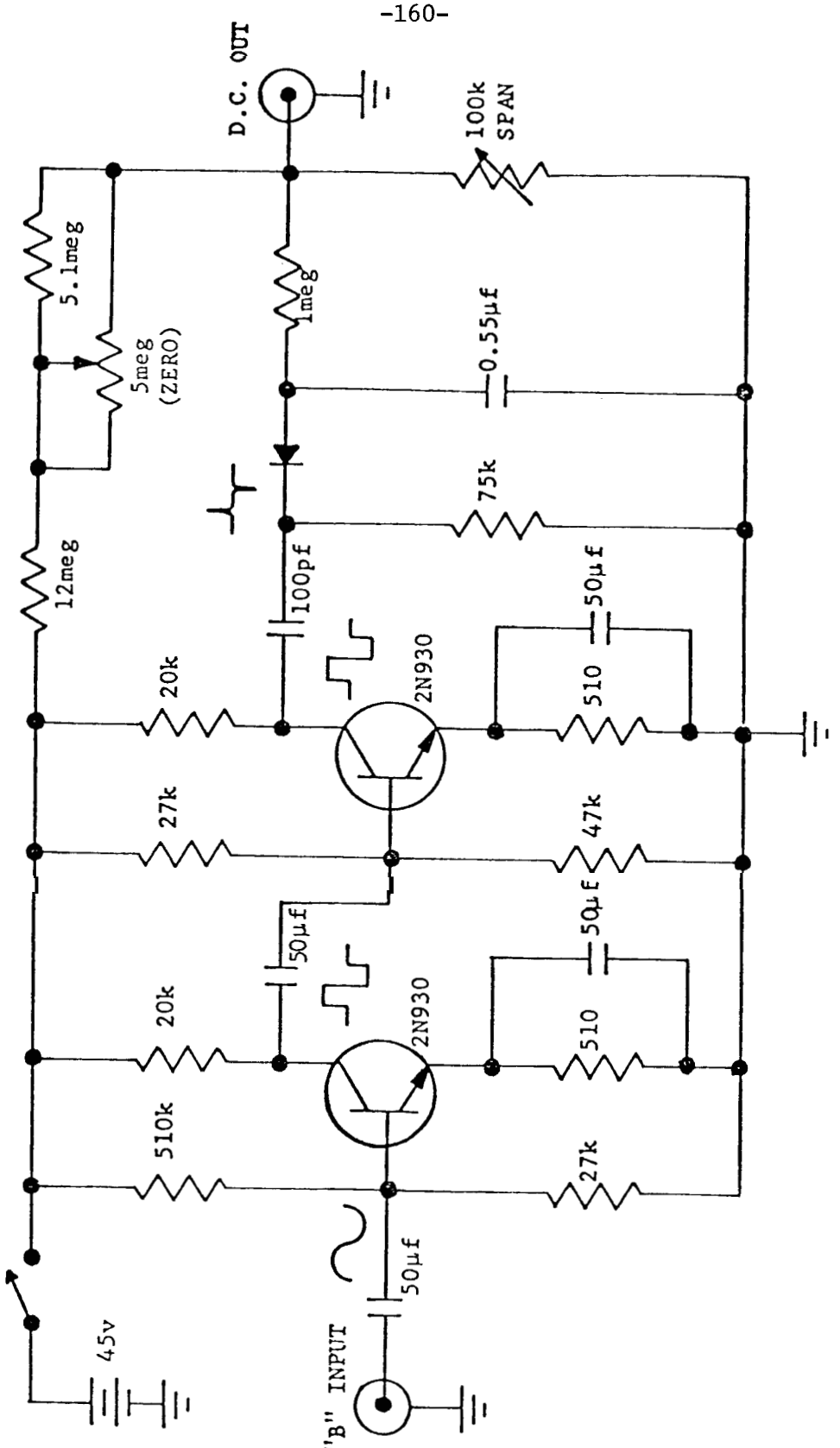

FIG. A2-3: DIGITAL TO ANALOG CONVERTER CIRCUIT USED TO RECORD FREQUENCY (ARIHARA, 1974)

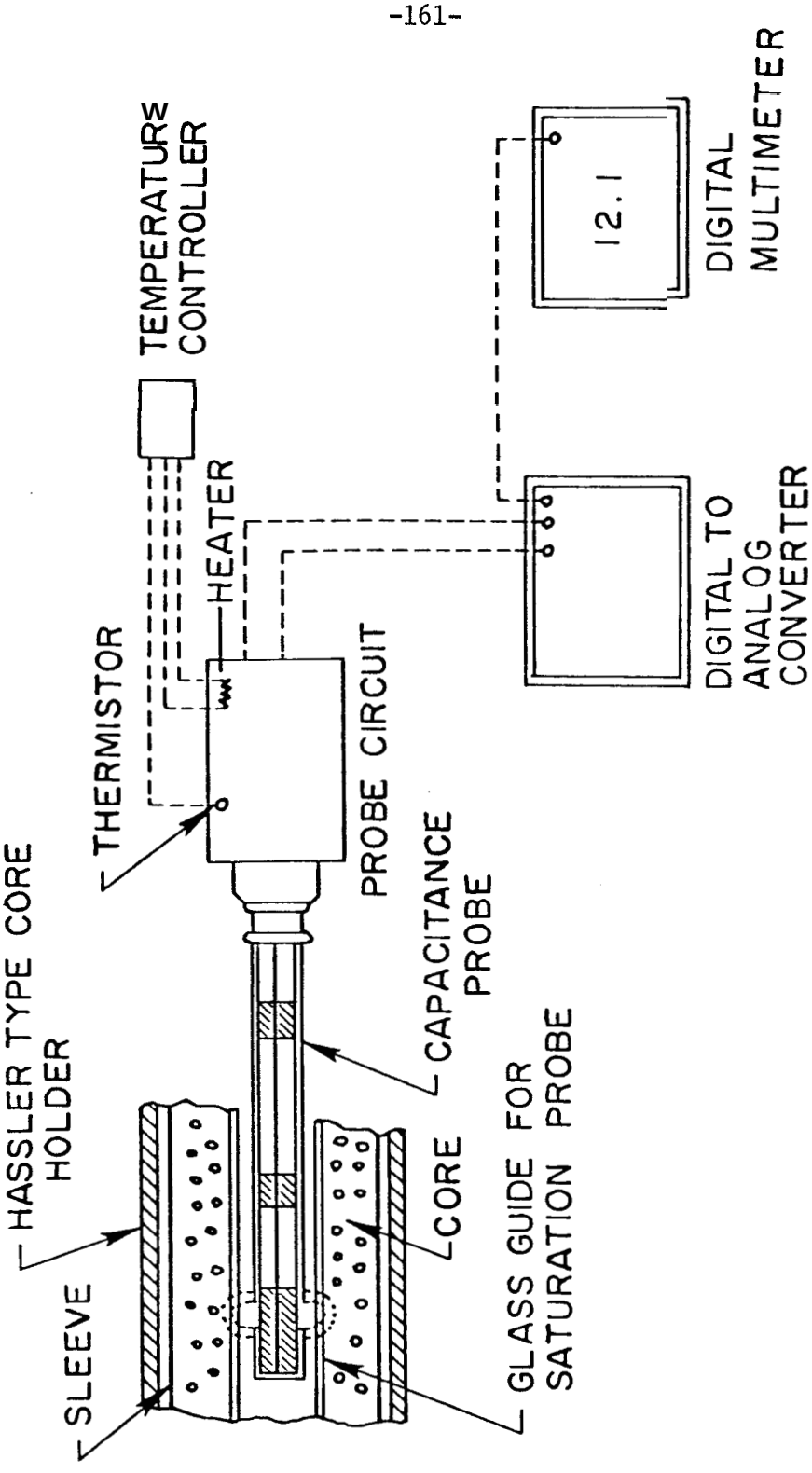

FIG. A2-4: SCHEMATIC DIAGRAM FOR IN-SITU MEASUREMENT OF WATER SATURATION IN STEAM-WATER FLOW IN SYNTHETIC CONSOLIDATED SANDSTONE CORE (CHEN, 1976)

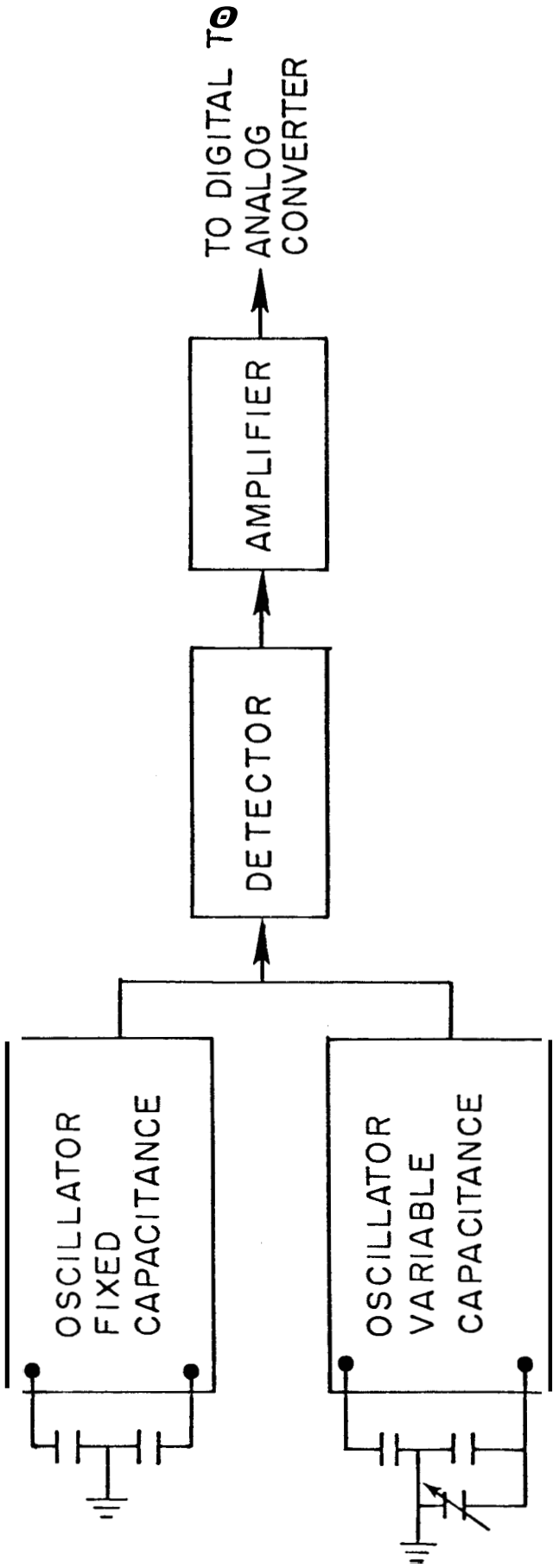

FIG. A2-5: SCHEMATIC DIAGRAM OF THE PROBE CIRCUIT (CHEN, 1976)

APPENDIX 3: TABULATED EXPERIMENTAL DATA AND CALCULATIONS

This appendix contains the experimental data and calculations discussed in Section 6. Appendix A3.1 presents the capacitance probe calibration data. Appendix A3.2 presents the data for the nonisothermal, steady, steam–water flow experiments. Appendix A3.3 contains the data and calculations for the isothermal, unsteady, nitrogen–water flow experiments.

A3.1 Capacitance Probe Calibration

This appendix contains the experimental data and calculations discussed in Section 6.1. Tables A3.1–1 and A3.1–2 present data obtained using the Baker–type electronics before it was repaired. Tables A3.1–3 through A3.1–9 present data obtained at different frequencies using the Q–meter. Tables A3.1–10 through A3.1–13 present the final calibration data obtained with two different Baker–type electronics packages.

A3.2 Nonisothermal, Steady, Steam–Water Flow

This appendix contains the experimental data discussed in Section 6.2. Tables A3.2–1 through A3.2–3 present the core temperatures and normalized probe signal profiles for Runs SW1, SW2, and SW3.

A3.3 Isothermal, Unsteady, Nitrogen–Water Flow

This appendix contains the experimental data and calculations discussed in Section 6.3. Tables A3.3–1 through A3.3–3 present the data for Run NW1. Tables A3.3–4 through A3.3–6 present the data for Run NW2. Tables A3.3–7 through A3.3–9 present the data for Run NW3. The isothermal

gas drive data are contained in Tables A3.3-1, A3.3-4, and A3.3-7. The calculated values used in the graphical analysis are presented in Tables A3.3-2, A3.3-5, and A3.3-8. The results of the graphical analysis and the relative permeability calculations are contained in Tables A3.3-3, A3.3-6, and A3.3-9. The results presented in Appendix A3.3 are summarized graphically in Fig. 6-18.

TABLE A3.1-1: CAPACITANCE PROBE CALIBRATION DATA: BAKER-TYPE ELECTRONICS BEFORE REPAIR (350°F); 9/16-22/76; 18-20 MESH SAND

Grams H_2O in Core:	790.9	754.6	724.9	694.9	644.9	584.9	524.9	464.9	404.9	344.9	284.9	224.9	164.1	6.2	0
								Φ (-mV)							
Distance from Inlet End, in.	Φ_ω	Φ	Φ	Φ	Φ	Φ	Φ	Φ	Φ	Φ	Φ	Φ	Φ	Φ	Φ_s
1.25	117.3	115.5	115.1	114.8	114.4	114.3	113.3	112.6	112.8	112.8	111.3	108.2	106.5	90.8	90.0
1.75	117.9	115.5	115.1	115.0	114.5	114.2	113.1	112.4	112.5	111.7	110.3	107.3	105.9	90.8	90.0
2.75	117.3	114.9	114.8	114.7	114.5	114.1	113.4	112.8	112.7	110.4	110.2	107.2	105.4	90.9	89.9
3.75	116.8	113.6	113.5	113.5	113.3	112.9	112.6	112.0	111.9	109.8	108.4	106.6	105.1	90.8	89.8
4.75	116.4	112.9	112.8	112.6	112.3	111.8	111.4	111.2	111.3	109.4	108.0	106.5	105.0	90.8	89.9
5.75	115.8	112.8	112.7	112.6	112.0	111.5	110.9	110.9	110.9	109.4	108.0	106.6	105.3	90.8	89.8
6.75	115.2	112.9	112.8	112.8	112.1	111.5	110.7	110.3	110.2	109.2	107.8	106.4	105.0	90.7	89.8
7.75	115.0	112.7	112.6	112.5	112.1	111.5	110.7	110.1	109.9	108.8	107.5	106.3	104.9	90.7	89.8
8.75	114.9	112.6	112.3	112.3	112.0	111.2	110.3	109.7	109.5	108.3	107.2	106.2	105.0	90.6	89.8
9.75	114.8	113.1	112.8	112.8	112.4	111.5	110.7	109.8	109.5	108.1	107.2	105.8	104.9	90.6	89.8
10.75	114.9	113.3	112.9	112.9	112.7	111.7	110.8	109.9	109.5	108.0	107.1	106.1	104.9	90.5	89.8
11.75	115.0	113.6	113.1	113.0	112.8	111.7	110.8	109.9	109.2	107.6	106.8	106.0	104.5	90.5	89.9
12.75	115.0	113.5	113.1	113.0	113.1	112.0	111.1	109.9	108.8	107.5	106.4	105.6	104.2	90.5	89.8
13.75	114.6	113.1	112.7	112.5	112.8	111.6	110.7	109.4	108.3	106.8	105.9	105.0	103.8	90.5	89.8
14.75	114.2	113.0	112.7	112.6	112.7	111.7	110.9	109.6	108.2	106.9	105.7	104.8	103.4	90.5	89.7
15.75	114.5	112.8	112.4	112.2	112.5	111.7	110.8	109.7	108.3	107.0	106.0	105.2	103.6	90.4	89.4
16.75	114.4	112.8	112.4	112.3	112.5	111.8	110.8	109.4	108.3	107.1	106.1	105.3	103.9	90.4	89.5
17.75	114.1	113.6	112.8	112.7	112.9	112.3	111.0	109.6	108.6	107.5	106.3	105.6	104.1	90.4	89.5
18.75	113.7	113.6	112.8	112.6	113.0	112.3	111.4	109.8	108.7	107.6	106.3	105.6	103.8	90.3	89.4
19.75	113.4	113.5	112.9	112.6	112.6	112.2	111.9	110.1	108.8	107.8	106.4	105.7	103.8	90.2	89.3
20.75	113.2	113.2	112.5	111.9	112.1	111.5	111.5	110.6	108.9	107.9	106.2	105.8	103.4	90.1	89.2
21.75	112.7	112.7	112.2	111.7	111.9	111.1	111.1	110.3	108.8	107.8	106.0	105.6	103.1	90.0	89.1

TABLE A3.1-2: CAPACITANCE PROBE CALIBRATION DATA: BAKER-TYPE ELECTRONICS BEFORE REPAIR (300°F); 10/29/76-11/2/76; 18-20 MESH SAND

Grams H_2O in Core:	891.6	699.4	584.3	455.4	359.8	307.8	238.3	174.4	106.5	44.2	0
Distance from Inlet End, in	Φ_w	Φ	Φ	Φ	Φ	Φ, (-mV) Φ	Φ	Φ	Φ	Φ	Φ_s
2	105 1	10Z 4	100 0	99 0	97 2	95.9	93.9	89 1	84 ⅃	83 7	79.9
4	103.8	102.4	99.6	98.4	97.6	96.3	94.1	92.3	84.7	83.7	79.7
8	101 8	102.9	100 Z	99 3	97 0	95 8	94 6	93 3	∃1 1	85 1	79 7
12	102.5	103.6	99.6	99.1	96.7	95.6	94.4	93.3	91.4	88.8	79.7
16	102.5	100 8	104.0	100 1	97 5	9 ∃	95 3	94	9Z 4	∃8 ⊏	79 9
ZO	10Z 4	10∃ 4	10∃.6	100 0	97 5	96 7	95 3	94.9	9⊏.6	89 4	79 6

TABLE A3.1-3: CAPACITANCE PROBE CALIBRATION DATA: Q-METER (7.5 MHz);

11/22-23/77 310°F, 7.5 MHz, C_1=170 pf 20-30 MESH SAND

Gram H_2O in Core	726.5	610.6	414.6	207.3	0
Room Temp. °F	75.0	68.0	72.5	74.2	71.0
			ΔC, pf		
Distance from Inlet End, in	ΔC_w	ΔC	ΔC	AC	AC_s
3	-2.61	-2.64	-1.56	-0.22	+0.79
5	-2.22	-2.19	-1.08	+0.03	+0. 86
7	-2.25	-2.00	-.98	0.00	+0.89
9	-2.32	-2.30	-1.32	-0.32	+0. 79
11	-2.31	-2.51	-1.46	-0.28	+0. 79
13	-2.39	-2.43	-1.68	-0.39	+0.78
15	-2.50	-2.61	-1.76	-0.25	+0.81
17	-2.82	-2.78	-1.95	-0.19	+0.83
19	-2.58	-2.78	-1.92	-0.20	+0. 81
21	-2.78	-2.81	-1.72	-0.08	+0.91
23	-1.78	-1.74	-.91	-0.26	+0. 56

Note: temperature correction = *-0.04* pf/°F

TABLE A3.1-4: CAPACITANCE PROBE CALIBRATION DATA: Q-METER (40 kHz)

11/24-25/77 310°F, C_1 = 194 pf 20-30 MESH SAND

Gram H_2O in Core	724.1	509.9	343.3	124.3	0
			ΔC, pf		
Distance from Inlet End, in	ΔC_w	AC	AC	AC	ΔC_s
2	-3.52	-3.41	-3.19	-3.19	+2.13
4	-2.21	-2.41	-2.13	-2.06	+2.19
6	-2.24	-2.52	-2.21	-2.19	+2.16
8	-2.49	-2.52	-2.32	-2.41	+2.15
10	-2.74	-2.90	-2.94	-2.69	+2.05
12	-2.48	-2.60	-2.52	-2.45	+2.13
14	-2.89	-2.88	-2.81	-2.72	+2.11
16	-2.79	-3.06	-2.81	-2.71	+2.06
18	-3.18	-3.39	-3.04	-3.00	t 2I21
20	-3.29	-3.44	-3.10	-3.05	+2.20
22	-3.42	-3.31	-3.00	-3.05	+2.31

Note: The 47 mH coil used at 40 kHz did not demonstrate a well-defined temperature sensitivity.

TABLE A3.1-5: CAPACITANCE PROBE CALIBRATION DATA: Q-METER (750 kHz)

11/26-27/77 310°F, C_1 = 182 pf 20-30 MESH SAND

Grams H_2O in Core	723.7	534.7	347.4	140.5	0
Room Temp. °F	76.7	77.5	73.3	71.0	68.0
			ΔC, pf		
Distance from Inlet End, in	ΔC_w	AC	AC	AC	ΔC_s
2	-4.41	-3.29	-2.21	-0.80	+0.19
4	-3.41	-2.59	-1.55	-0.81	+0. 24
6	-3.61	-2.81	-1.61	-0.91	+0.22
8	-3.65	-3.30	-1.81	-0.79	+0.29
10	-3.81	-3.22	-2.06	-0.81	+0. 28
12	-3.65	-2.93	-2.00	-0.82	+0.29
14	-3.88	-3.05	-2.20	-0.65	+0.22
16	-3.75	-3.28	-2.33	-0.60	+0.30
18	-4.15	-3.59	-2.34	-0.58	+0.33
20	-4.21	-3.54	-2.42	-0.55	+0.39
22	-4.37	-3.19	-1.82	-0.72	+0.48

Note: temperature correction = -0.04 pf/°F

TABLE A3.1-6: **CAPACITANCE PROBE CALIBRATION** DATA: **Q-METER** (100 kHz)

12/1/77 310°F, $C_{\perp}$ = 100 **pf** 20–30 MESH **SAND**

Grams H_2O in Core	727.1	576.0	405.1	145.3	0
Room Temp. °F	68.8	74.0	77.7	72.8	71.8
			ΔC, pf		
Distance from Inlet End, in		**AC**	**ΔC**	**AC**	
2	−4.38	−4.11	−3.60	−3.10	+129
4	−3.05	−2.92	−2.72	−2.15	+130
6	−3.61	−3.16	−2.75	−2.31	+131
8	−3.42	−3.25	−2.79	−2.37	+130
10	−3.71	−3.55	−3.06	−2.64	+131
12	−3.30	−3.09	−2.72	−2.52	+131
14	−3.69	−3.50	−3.04	−2.55	+1.41
16	−3.61	−3.40	−3.02	−2.42	+140
18	−4.03	−3.89	−3.48	−2.55	+139
20	−4.09	−4.02	−3.62	−2.71	+1.41
22	−4.21	−3.99	−3.56	−2.75	+141

Note: temperature correction = −0.03 pf/°F

TABLE A3.1-7: CAPACITANCE PROBE CALIBRATION DATA: Q-METER (180 kHz)

12/5/77 305°F, C_1 = 55 pf 20-30 MESH SAND

Grams H_2O in Core	727.1	557.8	367.7	237.4	0
Room Temp. °F	76.9	78.6	81.1	78.3	75.9
			ΔC, pf		
Distance from Inlet End. in		ΔC	AC	AC	AC_5
2	-3.38	-3.46	-2.69	-1.52	+178
4	-3.19	-2.94	-2.13	-1.12	+1.81
6	-3.28	-3.20	-2.27	-1.32	+182
8	-3.09	-2.69	-2.11	-1.31	+182
10	-3.39	-3.00	-2.41	-1.60	+186
12	-2.86	-2.62	-2.24	-1.61	+186
14	-2.97	-2.70	-2.37	-1.62	+1.91
16	-2.92	-2.76	-2.39	-1.70	+1.95
18	-3.26	-3.03	-2.53	-1.81	+1.97
20	-3.48	-3.22	-2.74	-1.93	+1.95
22	-3.49	-3.25	-2.59	-1.78	+198

Note: temperature correction = 0-.05 pf/°F

TABLE A3.1-8: CAPACITANCE PROBE CALIBRATION DATA: Q-METER (14 MHz)

12/6/77 | 310°F, C_1 = 35 pf | 20-30 MESH SAND

Grams H_2O in Core	725.5	559.9	390.0	185.5	0
Room Temp. °F	74.1	76.8	80.2	81.6	77.5
			ΔC, pf		
Distance from Inlet End, in	ΔC_w	AC	AC	AC	ΔC_s
2	-4.29	-2.97	-0.81	+2.21	+4.08
4	-3.71	-2.02	+0.03	+2.59	+4.18
6	-3.86	-2.53	0.00	+2.52	+4.02
8	-3.39	-2.21	-0.26	+2.38	+4.03
10	-3.46	-2.29	-0.53	+2.19	+4.11
12	-3.31	-2.05	-0.32	+2.41	+4.10
14	-3.32	-2.30	-0.43	+2.25	+4.18
16	-3.28	-2.26	-0.50	+2.30	+4.28
18	-3.33	-2.41	-0.61	+2.41	+4.29
20	-3.41	-2.75	-0.75	+2.32	+4.32
22	-3.79	-2.51	+0.04	+2.79	+4.38

Note: unstable response prevented temperature calibration

TABLE A3.1-9: CAPACITANCE PROBE CALIBRATION DATA: Q-METER (7.5 MHz)

12/8-10/77 — 305°F, C_1 = 170 pf — 20-30 MESH SAND

Grams H_2O in Core	725 7	633 3	573 3	517 0	456.5	397.0	339.5	260 0	197 1	125 4	63 4	0
Room Temp. °F	81.2	82.0	81.5	78.8	71.4	73.0	75.8	80.7	78.5	75.7	74.1	77.5

μC, μf

Distance from Inlet End, in	ΔC_w	ΔC	ΔC	μC	ΔC	ΔC	ΔC	ΔC	ΔC	ΔC	ΔC	ΔC_s
2	-3.08	-2.85	-2.82	-2.90	-2.56	-1.98	-1.40	-0.79	-0.62	-0.35	-0.13	+0.39
4	-2.89	-2.79	-2.41	-2.21	-2.61	-1.72	-1.39	-0.69	-0.42	-0.29	-0.05	+0.48
6	-2.81	-2.72	-2.78	-2.56	-2.19	-1.75	-1.28	-0.62	-0.41	-0.30	-0.09	+0.45
8	-2.69	-2.68	-2.32	-2.31	-2.29	-1.80	-1.42	-0.76	-0.50	-0.36	-0.10	+0.38
10	-2.80	-2.76	-2.42	-2.30	-2.28	-1.90	-1.61	-0.80	-0.58	-0.41	-0.18	+0.37
12	-2.63	-2.58	-2.08	-2.05	-2.12	-1.89	-1.50	-0.87	-0.52	-0.28	-0.08	+0.45
14	-2.69	-2.72	-2.34	-2.30	-2.39	-2.02	-1.65	-0.88	-0.52	-0.24	-0.06	+0.45
16	-2.71	-2.50	-2.42	-2.32	-2.19	-2.00	-1.61	-0.92	-0.32	-0.22	-0.06	+0.48
18	-2.79	-2.39	-2.22	-2.09	-2.13	-1.91	-1.49	-0.80	-0.30	-0.14	-0.02	+0.53
20	-2.80	-2.22	-2.19	-2.12	-2.20	-1.90	-1.60	-1.00	-0.35	-0.15	+0.06	+0.50
22	-3.02	-2.65	-2.25	-2.02	-1.91	-1.60	-1.21	-0.67	-0.22	-0.03	+0.18	+0.55

Note: temperature correction = -0 04 μf/°F

TABLE A3.1-10: **CAPACITANCE PROBE CALIBRATION DATA: BAKER-TYPE ELECTRONICS** *(80-170* MESH, **UNIT NO. 1)**

2/9-10/78 *305°F* *80-170* **MESH SAND**

Gram H_2O in Core	*849.2*	*692.2*	*488.2*	*367.3*	*227.2*	0
			Φ, (-mV)			
Distance from Inlet End, in	Φ_w	Φ	Φ	Φ	Φ	Φ_5
4	*85.3*	*83.2*	*69.4*	*67.2*	*63.6*	*57.1*
6	*85.8*	*84.6*	*71.4*	*69.2*	*65.3*	*57.1*
8	*84.9*	*84.0*	*70.2*	*67.8*	*64.3*	*57.0*
10	*84.2*	*81.4*	*70.3*	*67.8*	*66.5*	*56.6*
12	*85.2*	*85.2*	*74.6*	*73.9*	*71.3*	*56.4*
14	*86.1*	*85.6*	*74.7*	*73.3*	*70.8*	*56.3*
16	*86.1*	*85.3*	*73.1*	*71.7*	*68.7*	*56.2*
18	*85.9*	*85.5*	*74.2*	*73.3*	*69.8*	*56.1*
20	*85.7*	*83.3*	*70.5*	*68.8*	*65.8*	*56.1*

TABLE A3 1-11: CAPACITANCE PROBE CALIBRATION DATA: BAKER-TYPE ELECTRONICS (20-30 MESH SAND, UNIT NO. 1)

2/15-16/78 | 302°F | 20-30 MESH SAND

Gram H_2O in Core	705 7	61⊟ 7	523 6	442.3	370.2	296.4	225.2	16⊏.7	83 8	0
					Φ, (-mV)					
Distance f om Inlet End, in	Φ_w	Φ	Φ	Φ	Φ	Φ	Φ	Φ	Φ	s
1.25	73.0	73.8	71.1	67.5	64.6	63.6	62.2	61.9	60.7	59.5
2	73.3	73.2	70.6	66.6	64.8	62.3	61.1	60.3	59.1	57.4
3	73.2	72.8	71.7	69.9	66.7	64.3	62.5	61.3	59.9	57.6
4	73·9	72.6	70.3	68.1	65.2	63.3	62.2	60.9	59.8	57.6
5	73·8	72.2	70.0	67.8	64.9	63.2	62.1	60.8	59.9	57.8
6	73·4	72.8	69.8	67.6	64.5	62.9	61.9	60.7	59.9	57.8
7	73·7	72.2	71.2	69.4	66.1	63.7	62.4	61.1	60.0	57.8
8	73·1	71.8	70.4	68.7	65.2	63.2	62.1	60.8	60.2	57.6
9	73.1	71.9	70.3	68.0	64.4	62.8	61.9	60.6	59.6	57.6
10	72.8	71.7	70.8	69.1	65.7	63.6	62.3	60.9	59.8	57.6
11	72.7	71.4	70.1	69.2	66.2	63.9	62.5	60.9	60.0	57.6
12	73·0	71.5	70.2	68.9	66.3	63.8	62.5	60.9	59.7	57.6
13	72·3	71.8	70.4	68.6	66.1	63.6	62.4	60.9	59.6	57.6
14	72·6	72.0	70.3	68.1	65.3	63.1	62.0	60.8	59.6	57.6
15	72·0	71.7	70.3	68.0	65.3	63.1	61.9	60.6	59.5	57.5
16	71·8	71.6	70.0	68.0	65.2	63.0	61.7	60.5	59.4	57.5
17	72.0	71.6	70.1	68.2	65.8	63.4	61.9	60.5	59.2	57.4
18	71.5	70.7	69.4	67.2	64.9	63.0	61.4	60.1	59.0	57.1
19	71.3	70.2	69.0	66.7	64.7	62.8	61.2	59.9	58.8	57.0
20	71.5	70.6	69.8	67.0	64.9	63.2	61.3	59.8	58.7	56.9
21	71 2	70.4	69.7	67.9	66.2	64.3	61.7	59.9	58.7	56.8
22	71 2	70.1	69.4	68.1	66.1	64.1	61.9	59.9	58.5	56.6

TABLE A3.1-12: CAPACITANCE PROBE CALIBRATION DATA: BAKER-TYPE ELECTRONICS (20-30 MESH SAND, UNIT NO. 2)

2/17-19/78 303°F 20-30 MESH SAND

Gram H_2O in Core	700 ±	628 2	552 1	471.0	392.6	319.2	242.8	161.9	83.4	0
					Φ, (-mV)					
Distance from Inlet End, in	Φ_w	Φ	Φ	Φ	Φ	Φ	Φ	Φ	Φ	Φ_s
1.25	71.9	72.1	71.1	67.2	64.9	63.7	62.6	61.9	60.7	58.2
2	72.6	72.1	71.3	66.9	64.4	62.8	61.5	60.2	59.1	56.7
3	72.5	72.2	72.2	65.9	67.6	65.3	63.1	61.4	59.8	56.9
4	72.9	72.8	71.8	69.6	66.1	64.1	62.6	61.0	59.7	57.0
5	73.0	72.9	72.3	69.7	66.0	63.7	62.2	61.1	59.8	57.3
6	73.0	71.6	72.0	68.7	65.4	63.3	62.1	61.0	59.7	57.2
7	72.3	72.2	72.0	70.0	67.1	64.4	62.6	61.3	59.9	57.3
8	71.9	71.8	71.2	69.2	66.5	64.0	62.2	61.0	59.6	57.0
9	71.8	71.6	70.0	67.9	65.2	63.3	61.9	60.9	59.4	57.0
10	71.7	71.4	70.3	68.8	66.1	64.4	62.5	61.0	59.6	57.1
11	71.3	71.2	71.1	69.8	67.0	65.0	62.9	61.1	59.7	57.0
12	71.5	71.5	71.2	69.4	67.0	65.1	63.0	61.2	59.7	57.0
13	71.7	71.7	71.3	69.6	66.9	64.7	62.7	61.0	59.6	57.0
14	72.0	71.7	71.3	69.8	66.0	63.9	62.1	60.8	59.5	57.2
15	71.6	71.2	70.6	69.2	66.1	64.7	62.0	60.7	59.3	57.0
16	71.2	71.1	69.9	68.3	66.0	63.4	61.8	60.5	59.2	57.0
17	71.2	71.1	69.1	68.0	66.1	63.8	62.0	60.6	59.2	56.9
18	70.9	69.8	68.6	67.1	65.3	63.2	61.6	60.2	59.0	56.7
19	70.7	69.6	68.7	66.9	65.1	63.0	61.4	60.1	58.8	56.5
20	70.7	69.8	69.1	67.2	65.4	63.3	61.6	60.2	58.9	56.4
21	70.6	69.6	69.1	68.0	66.7	64.6	62.4	60.7	59.0	56.4
22	70.5	69.5	69 1	68.5	67.0	65.0	62.6	60.4	58.8	56.2
23	75.6	74.5	74 5	74.3	74.0	73.1	73.0	73.0	72.8	70.3

TABLE A3.1-13: CAPACITANCE PROBE CALIBRATION DATA; BAKER-TYPE ELECTRONICS (20-30 MESH SAND, UNIT NO. 2)

2/23-24/78 | 305°F | 20-30 MESH SAND

Gram H_2O in Core	701 7	627 6	≤⊂6 ⊂	462.7	360.8	257 3	166 2	74 1	0
					Φ, (-mV)				
Distance from Inlet End, in	Φ_w	Φ	Φ	Φ	Φ	Φ	Φ	Φ	Φ_s
1.25	71.7	70.3	70.3	66.7	62.7	61.1	59.9	60.6	58.7
2	71.2	71.0	70.0	66.1	63.0	61.1	59.9	58.9	56.8
3	70.9	70.9	70.4	68.9	65.3	62.5	60.8	59.1	57.2
4	71.4	71.3	70.7	67.4	64.1	61.8	60.5	59.2	57.3
5	71.7	71.5	70.6	67.9	63.8	61.6	60.4	59.4	57.5
6	71.6	71.4	70.4	67.2	63.6	61.3	60.2	59.5	57.3
7	71.0	70.9	70.2	68.1	64.7	61.8	60.5	59.7	57.4
8	70.6	70.5	70.3	67.1	64.0	61.6	60.3	59.4	57.3
9	70.3	70.3	69.5	67.3	63.5	61.2	60.2	59.3	57.2
10	70.1	70.0	69.5	66.8	64.3	61.8	60.4	59.4	57.2
11	70.0	70.0	69.4	67.9	65.1	62.1	60.6	59.4	57.2
12	70.0	70.0	69.4	67.3	64.9	62.0	60.6	59.3	57.1
13	70.2	70.1	69.3	66.5	64.2	61.8	60.3	59.2	57.1
14	70.3	71.4	68.8	66.3	63.9	61.4	60.1	59.1	57.1
15	70.0	70.8	68.0	67.3	63.8	61.3	60.2	59.0	56.9
16	70.9	69.9	68.2	67.1	64.0	61.4	60.0	58.9	56.8
17	70.9	69.8	68.2	66.9	64.4	61.6	60.1	59.1	56.8
18	70.5	69.0	67.3	65.9	63.6	61.1	59.9	58.9	56.5
19	70.2	69.4	67.0	65.8	63.4	61.1	59.8	58.8	56.3
20	70.2	69.9	67.7	66.1	63.6	61.5	60.0	58.8	56.1
21	70.3	69.0	68.2	67.7	64.9	61.6	60.6	58.9	56.0
22	70 3	68.9	68.3	67.7	65.1	61.5	60.4	58.7	55.9
22.5	69 7	68.9	67.8	67.2	65.0	61.2	60.0	58.8	56.7

TABLE A3.2-1: **NONISOTHERMAL, STEADY, STEAM-WATER FLOW DATA, RUN SW1**

RUN SW1 (5/26/78)

Absolute Permeability to Water, K = 26 **md**

Inlet Pressure = ? **(calibration lost)**

Outlet Pressure = 34 **psig**

Confining Pressure = 470 **psig**

Mass Flow **Rate =** 1.60 **gm/min**

Inlet Temperature = 302°F

Airbath Temperature = 302°F

Core Length = 23 1/4 **in**

Core Cross-Sectional Area = 3.14 **in**^{2}

x Distance from Inlet End, in	T_{core} °F	Φ (-mV)	Φ_s @ 302°F (-mV)	Φ_w @ 294°F (-mV)	$\Phi^* = \frac{\Phi_5 - \Phi}{\Phi_s - \Phi_w}$
1	302	87.4	75.2	88.8	0.95
1.5		88.4	69.6	89.1	0.96
2	301	88.6	69.6	89.0	0.98
2.5		88.5	69.5	89.0	0.97
3		88.8	69.7	89.0	0.99
3.5		88.7	70.0	89.2	0.97
4	300	88.5	69.9	88.7	0.99
4.5		88.1	70.1	88.6	0.97
5	299	87.6	70.2	88.4	0.96
5.5		87.4	70.1	88.2	0.96
6	298	87.4	70.3	88.1	0.96
6.5		87.6	70.0	88.6	0.95
7	297	87.4	70.0	88.5	0.94
7.5		87.7	70.0	88.9	0.94
8	296	87.8	69.9	89.0	0.94
8.5		87.9	69.6	88.9	0.95
9	295	87.8	69.6	89.3	0.92
9.5		87.9	69.8	89.3	0.93
10	294	87.8	69.4	89.3	0.92
10.5		87.9	69.4	89.2	0.93
11	292	87.8	69.2	89.4	0.92
11.5		87.7	69.1	89.1	0.93
12	291	87.5	69.0	89.0	0.93
12.5		87.4	69.0	89.1	0.92
13	286	86.5	68.8	88.4	0.90
13.5	284	86.6	68.7	88.4	0.91
14	283	87.5	68.9	88.9	0.93
14.5	282	87.6	68.9	89.1	0.93
15	279	87.4	68.6	88.5	0.94

Continued

TABLE A3.2–1, **CONTINUED**

x Distance from Inlet End, in	T_{core} °F	Φ (-mV)	Φ_s @ 302°F (-mV)	Φ_w @ 294°F (-mV)	$\Phi^* = \frac{\Phi_s - \Phi}{\Phi_s - \Phi_w}$
15.5	279	86.9	68.4	88.5	0.92
16	279	87.3	68.5	88.5	0.94
16.5	278	87.0	68.4	88.2	0.94
17	278	86.4	68.3	87.7	0.93
17.5	276	86.3	68.4	88.0	0.91
18	275	86.4	68.3	88.1	0.91
18.5	273	86.5	68.3	88.0	0.92
19	272	86.6	68.3	87.7	0.94
19.5	270	86.2	68.3	88.4	0.89
20	268	86.3	68.4	88.4	0.90
20.5	265	86.3	68.4	88.4	0.90
21	263	86.1	68.2	88.0	0.90
21.5	259	85.9	68.1	87.8	0.90
22	255	85.9	68.0	87.9	0.90
22.5		81.4	70.5	82.7	0.89

TABLE A3.2-2: NONISOTHERMAL, STEADY, STEAM-WATER FLOW DATA, RUN SW2

RUN SW2 (6/5/78)
Absolute Permeability to Water, K = 34 md
Inlet Pressure = 57.0 psig
Outlet Pressure = 4.0 psig
Core Cross-Sectional Area = 3.14 in^2
Confining Pressure = 352 psi
Mass Flow Rate = 0.80 gm/min
Inlet Temperature = 302°F
Airbath Temperature = 315°F
Core Length = 23-3/16 in

x Distance From Inlet End, in	T_{core} °F	Φ (-mV)	Φ_s @ 316°F (-mV)	Φ_w @ 303°F (-mV)	$\Phi^* = \frac{\Phi_s - \Phi}{\Phi_s - \Phi_w}$
1	302	89.3	77.2	94.0	0.72
1.5	302	90.5	77.2	95.6	0.72
2	302	91.8	77.2	96.7	0.75
2.5	301	93.3	77.3	97.6	0.79
3	301	94.9	77.6	97.8	0.86
3.5	301	95.6	77.7	97.9	0.89
4	301	95.5	77.5	97.8	0.89
4.5	300	95.5	77.5	97.5	0.90
5	299	95.6	77.5	97.2	0.92
5.5	299	95.4	77.1	97.0	0.92
6	298	95.2	77.0	96.9	0.91
6.5	298	95.1	76.9	96.8	0.91
7	297	95.3	76.8	96.9	0.92
7.5	296	94.8	76.4	96.8	0.90
8	296	94.7	76.3	96.7	0.90
8.5	295	94.6	76.5	96.8	0.89
9	294	94.6	76.6	96.7	0.90
9.5	293	94.8	77.0	96.6	0.91
10	292	95.1	77.1	96.5	0.93
10.5	291	95.0	76.8	96.4	0.93
11	289	94.9	76.6	96.4	0.92
11.5	288	94.9	76.4	96.3	0.93
12	287	93.5	76.4	95.8	0.88
12.5	286	93.6	76.3	94.9	0.93
13	286	93.5	76.2	94.7	0.94
13.5	285	94.5	76.0	94.6	0.99
14	284	93.6	76.0	95.0	0.93
14.5	283	93.4	75.9	94.4	0.95
15	280	92.7	76.0	95.1	0.87

Continued

TABLE A3.2-2, **CONTINUED**

Inlet End, in	T_{core} °F	Φ (-mV)	Φ @ 316°F (-mV)	Φ_W @ 303°F (-mV)	$\Phi^* = \frac{\Phi_S - \Phi}{\Phi_S - \Phi_W}$
15.5	279	92.9	76.4	94.4	0.92
16	278	92.7	76.0	94.2	0.92
16.5	277	92.8	76.0	92.7	1.01
17	275	90.9	75.7	91.1	0.99
17.5	273	88.9	75.7	90.7	0.88
18	271	88.6	75.6	91.4	0.82
18.5	268	88.7	75.7	92.8	0.76
19	266	89.4	76.0	92.7	0.80
19.5	263	88.7	75.8	93.5	0.73
20	259	87.6	75.8	92.2	0.71
20.5	257	86.3	75.6	92.8	0.62
21	254	83.8	75.4	92.8	0.48
21.5	258	79.7	75.4	93.0	0.24
22	269	76.5	74.9	92.3	0.09
22.5	280	76.6	76.6	84.4	0.00
23	289				

TABLE A3.2-3: **NONISOTHERMAL, STEADY, STEAM-WATER FLOW DATA, RUN** *SW3*

RUN *SW3* (7/1/78, 6:10 **pm)**

Absolute Permeability to Water, K = *35.8* **md**

Inlet Pressure = *137.0* **psig**

Outlet Pressure = *36.0* **psig**

Confining Pressure = *372* psig

Mass *Flow* **Rate** = *1.85* **gm/min**

Inlet Temperature = 350°F

Airbath Temperature = *344°F*

Core Length = *23.1* **in**

Core Cross-Sectional Area = *3.14* **in**^{2}

x Distance from Inlet End, in	T_{core} °F	Φ (-mV)	Φ_s @ 346°F (-mV)	Φ_w @ 348°F (-mV)	$\Phi^* = \frac{\Phi_5 - \Phi}{\Phi_s - \Phi_w}$
1 13/16	349	86.0	71.6	86.8	0.95
2	349	85.0	69.6	88.2	0.83
2.5		86.6	69.9	88.8	0.88
3	347	88.7	70.1.	89.1	0.98
3.5		87.8	70.2.	88.8	0.95
4	345	88.9	70.4	89.1	0.99
4.5		87.9	70.7	88.9	0.95
5	344	87.8	70.6	89.0	0.93
5.5		87.8	70.3	89.0	0.94
6	343	88.6	70.1.	89.0	0.98
6.5		88.4	69.9	89.0	0.97
7	342	87.2	69.6	89.0	0.91
7.5		86.6	69.4	89.0	0.88
8	341	87.0	69.3	88.6	0.92
8.5		86.6	69.2	88.7	0.89
9	338	86.6	69.3	88.8	0.89
9.5		86.8	69.6	88.9	0.89
10	336	87.0	69.7	89.0	0.90
10.5		86.8	69.6	89.0	0.89
11	335	85.8	69.6	89.0	0.84
11.5		86.2	69.4	90.2	0.81
12	334	85.8	69.3	89.8	0.80
12.5		84.8	69.3	89.5	0.77
13	333	85.5	69.2	88.1	0.86
13.5	332	86.3	69.2	87.2	0.95
14	331	85.8	69.0	87.7	0.90
14.5	330	86.0	69.0	88.0	0.89
15	328	85.7	69.0	87.8	0.89

Continued

TABLE A3.2-3, **CONTINUED**

x Distance from Inlet End, in	T_{core} °F	Φ (-mV)	Φ_s @ 346°F (-mV)	Φ_w @ 348°F (-mV)	$\Phi^* = \frac{\Phi_s - \Phi}{\Phi_s - \Phi_w}$
15.5	327	85.3	69.1	87.7	0.87
16	326	84.9	69.0	87.1	0.88
16.5	326	85.0	68.9	87.1	0.88
17	325	84.9	68.8	87.2	0.88
17.5	323	84.6	68.7	87.2	0.86
18	321	84.3	68.6	87.2	0.84
18.5	319	84.3	68.6	87.4	0.84
19	316	83.7	68.5	87.0	0.82
19.5	312	83.4	68.5	86.6	0.82
20	309	83.1	68.7	86.6	0.80
20.5	306	83.5	68.8	86.7	0.82
21	301	83.9	68.7	86.7	0.84
21.5	296	83.6	68.3	86.4	0.85
22	291	83.7	68.3	86.5	0.85
22.5	286	83.6	68.2	86.7	0.83
23	271	81.4	67.6	83.9	0.85
23.5	239	79.3			

TABLE A3.3-1: ISOTHERMAL GAS-DRIVE DATA, RUN NW1

RUN NW1 (11/18/78)

V_P = 495 mℓ
L = 23.1 in
D = 2 in
ϕ = 0.34
K = 36 md
S_{gi} = 0

T_{core} = 78°F
T_{room} = 78°F
p_{bar} = 14.82 psia

At sec	W_P @ T_{room} mℓ	G_{sep} @ T_{room}, p_{bar} ℓ	p_{in} psig	Δp psi
92	6	0	147.6	70.9
160	9	0	147.6	70.9
220	20	0	147.6	71.8
350	43	0.02	145.1	72.6
435	54	0.13	145.1	72.6
495	64	0.22	145.1	72.6
570	72	0.33	145.1	72.6
690	78	0.64	144.6	71.8
785	83	0.87	144.6	71.1
920	90	1.25	144.6	71.1
1,165	99	2.08	144.6	71.1
1,415	109	2.99	144.6	71.1
1,730	115	4.26	144.6	71.1
2,120	124	6.10	144.6	71.1
2,615	133	8.62	144.6	71.1
3,080	141	11.21	144.6	71.1
4,520	157	20.28	144.6	71.1
5,630	166	28.25	144.6	71.1
6,610	172	35.83	144.6	71.1
7,800	178	45.61	144.6	71.1
8,545	181	52.00	144.6	71.1
9,400	184	59.50	144.6	71.1
10,500	188	69.65	145.6	71.1
12,110	194	84.95	145.6	71.1
13,830	198	102.01	145.6	71.1
15,640	203	120.73	145.6	71.1
16,450	205	129.60	145.6	71.1
18,220	209	147.35	145.6	71.1
20,000	212	168.00	145.6	71.1

TABLE A3.3-2: **ISOTHERMAL GAS DRIVE CALCULATIONS FOR GRAPHICAL ANALYSIS, RUN** NW1

RUN NW1 (11/18/78)

T_{core} = 78°F; p_{avg} = 123 **psia**

$$\left[\frac{q\mu}{\Delta p}\right]_b = \frac{(K,md)(in^2)}{1.607(L,in)} = 3.04\ \frac{(m\ell/hr)cp}{psi}$$

Q_i pV	$\bar{S}_g$ pV	Time Step Average Qi pV	Time Step Average $\overline{\chi^{-1}}$ cp
0.0154	0.0154		
		0.019	1.36
0.0231	0.0231		
		0.037	0.327
0.0513	0.0513		
		0.084	0.310
0.116	0.110		
		0.147	0.215
0.178	0.138		
		0.205	0.177
0.232	0.164		
		0.259	0.216
0.286	0.185		
		0.342	0.170
0.398	0.200		
		0.440	0.176
0.482	0.213		
		0.549	0.154
0.616	0.231		
		0.756	0.135
0.895	0.254		
		1.05	0.126
1.20	0.280		
		1.40	0.119
1.61	0.295		
		1.90	0.102
2.20	0.318		
		2.60	0.0954
3.00	0.341		
		3.40	0.0875
3.81	0.362		
		5.23	0.0782
6.65	0.403		
		7.89	0.0690
9.13	0.426		
		10.3	0.0642

Continued

TABLE A3.3-2: CONTINUED

		Time Step Average	
Q_i pV	$\bar{S}_g$ pV	Q_i pV	$\overline{\lambda^{-1}}$ cp
11.5	*0.441*		
		13.0	*0.0605*
14.5	*0.456*		
		15.5	*0.0581*
16.5	*0.464*		
		17.6	*0.0568*
18.8	*0.472*		
		20.4	*0.0542*
21.9	*0.482*		
		24.3	*0.0529*
26.6	*0.497*		
		29.2	*0.0507*
31.8	*0.508*		
		34.7	*0.0486*
37.6	*0.521*		
		38.9	*0.0459*
40.3	*0.526*		
		43.0	*0.0502*
45.7	*0.536*		
		48.9	*0.0434*
52.0	*0.544*		

TABLE A3 3-3: ISOTHERMAL GAS DRIVE RELATIVE PERMEABILITY CALCULATIONS, RUN NW1

RUN NW1 (11/18/78)

T_{core} = 78°F
p_{avg} = 123 psia
y_{H_2O} = 0.00386
y_{N_2} = 0.996

$\mu_{H_2O(v)}$ = 0.00983 cp
μ_{N_2} = 0.0178 cp
μ_g = 0.0178 cp
μ_w = 0.884 cp

Q_i pV	$\bar{S}_g$ pV	f_{w2} $(\bar{S}_g - S_{g2})/Q_i$	f_{g2} $1-f_{w2}$	S_{g2} pV	λ_2^{-1} cp	k_{rg} $(f_{g2}\mu_g)/\lambda_2^{-1}$	k_{rw} $(f_{w2}\mu_w)/\lambda_2^{-1}$
0.166	0.151	0.201	0.799	0.118	0.272	0.0523	0.653
1.33	0.289	0.0560	0.944	0.214	0.137	0.123	0.362
5.32	0.385	0.0158	0.984	0.301	0.103	0.170	0.135
10.6	0.437	0.00569	0.994	0.377	0.0783	0.226	0.0642
42.6	0.530	0.00166	0.998	0.459	0.0600	0.296	0.0245

TABLE A3.3-4: ISOTHERMAL GAS DRIVE DATA, RUN NW2

RUN NW2 (11/22/78)

V_P = 495 mℓ
L = 23.1 in
D = 2 in
ϕ = 0.34
K = 36 md
S_{gi} = 0

T_{core} = 198°F
T_{room} = 73°F
p_{bar} = 14.71 psia

At sec	W_P @ T_{room} mℓ	G_{sep} @ T_{room}, p_{bar} ℓ	p_{in} psig	Δp psi
64	9	0	199.1	66.1
120	19	0	199.1	66.0
225	42	0	199.1	66.0
300	57	0	199.1	63.5
385	71	0.06	199.1	66.5
485	96	0.14	199.1	65.1
570	103	0.31	198.1	65.1
825	124	0.96	198.1	65.1
950	130	1.40	198.1	65.1
1,170	138	2.21	198.1	65.1
1,385	145	3.10	198.1	65.1
1,710	153	4.63	198.1	65.1
1,910	157	5.19	198.1	65.1
2,360	165	8.03	198.1	65.1
2,885	172	11.14	198.1	65.1
3,435	179	14.60	198.1	65.1
4,750	191	23.80	196.6	65.1
6,695	204	38.95	196.6	65.1
7,590	209	46.38	196.6	65.1
8,400	213	53.29	196.6	65.1
9,740	219	65.42	196.6	65.1
10,960	223	76.80	196.6	65.1
12,910	228	95.78	196.6	65.1
15,170	235	119.00	196.6	65.1
17,140	240	139.90	196.6	65.1
19,860	246	170.25	196.6	65.1
21,990	250	195.00	196.6	65.1
24,430	255	224.20	196.6	65.1
26,330	258	247.60	195.1	64.0

TABLE A3.3-5: **ISOTHERMAL GAS DRIVE CALCULATIONS** FOR **GRAPHICAL ANALYSIS,** RUN *NW2*

RUN NW2 (11/22/78)

T_{core} = *198°F*

p_{avg} = *179* **psia**

$$\left[\frac{q\mu}{\Delta p}\right]_b = \frac{(K,md)(A,in^2)}{1.607(L,in)} = 3.04\ \frac{(m\ell/hr)cp}{psi}$$

		Time Step Average	
Q_i pV	$\bar{S}_g$ pV	Q_i pV	$\overline{\lambda^{-1}}$ cp
0.0239	*0.0239*		
		0.0372	*0.302*
0.0504	*0.0504*		
		0.0809	*0.246*
0.112	*0.112*		
		0.131	*0.264*
0.151	**0.151**		
		0.178	*0.223*
0.205	*0.188*		
		0.249	*0.161*
0.293	*0.255*		
		0.326	*0.184*
0.358	*0.273*		
		0.476	*0.153*
0.593	*0.329*		
		0.662	*0.128*
0.730	*0.345*		
		0.852	*0.127*
0.974	*0.366*		
		1.11	*0.115*
1.24	*0.385*		
		1.46	*0.104*
1.68	*0.406*		
		1.76	*0.171*
1.85	*0.417*		
		2.25	*0.0790*
2.65	*0.438*		
		3.09	*0.0846*
3.52	*0.456*		
		4.01	*0.0798*
4.50	*0.475*		
		5.78	*0.0719*
7.07	*0.507*		
		9.20	*0.0646*

Continued

TABLE *A3.3-5:* CONTINUED

Q_i pV	$\overline{S}_g$ pV	Time Step Average Q_i pV	Time Step Average $\overline{\lambda-1}$ cp
11.3	*0.541*		
		12.4	*0.0607*
13.4	*0.555*		
		14.4	*0.0591*
15.3	*0.565*		
		17.0	*0.0558*
18.7	*0.581*		
		20.3	*0.0542*
21.9	*0.592*		
		24.5	*0.0520*
27.2	*0.605*		
		30.4	*0.0492*
33.6	*0.624*		
		36.6	*0.0477*
39.5	*0.637*		
		43.7	*0.0454*
47.9	*0.653*		
		51.4	*0.0436*
54.8	*0.664*		
		58.9	*0,0423*
62.9	*,0677*		
		66.2	*0.0406*
69.5	*0.685*		

TABLE A3 B-6: ISOTHERMAL GAS DRIVE RELATIVE PERMEABILITY CALCULATIONS, RUN NW2

RUN NW2

T_{core} = 198°F
p_{avg} = 179 psia
y_{H_2O} = 0.0620
y_{N_2} = 0.938

$\mu_{H_2O(v)}$ = 0.0123 cp
μ_{N_2} = 0.0207 cp
μ_g = 0.0203 cp
μ_w = 0.308 cp

Q_i pV	$\bar{S}_g$ pV	f_{w2} $(\bar{S}_g - S_{g2})/Q_i$	f_{g2} $1-f_{w2}$	S_{g2} pV	λ_2^{-1} cp	k_{rg} $(f_{g2}\mu_g)/\lambda_2^{-1}$	k_{rw} $(f_{w2}\mu_w)/\lambda_2^{-1}$
0.255	0.249	0.238	0.762	0.185	0.179	0.0863	0.403
1.02	0.372	0.103	0.897	0.268	0.170	0.107	0.183
4.08	0.464	0.0194	0.984	0.397	0.0986	0.202	0.0505
8.15	0.518	0.0102	0.990	0.434	0.0832	0.242	0.0373
16.3	0.570	0.00397	0.996	0.505	0.0684	0.296	0.0176
65.2	0.597	0.00143	0.999	0.589	0.0571	0.355	0.00760

TABLE A3.3-7: **ISOTHERMAL** GAS DRIVE DATA, RUN NW3

RUN NW3 (11/29/78)

V_P = 495 mℓ
L = 23.1 in
D = 2 in
ϕ = 0.34
K = 36 **md**
S_{gi} = 0

T_{core} = 294°F
T_{room} = 75°F
p_{var} = 14.89 psig

At sec	W_P @ T_{room} mℓ	G_{sep} @ T_{room}, p_{bar} ℓ	p_{in} psig	Δp psi
115	23	0	196.6	52.4
160	30	0	196.6	52.4
220	43	0	196.6	52.4
290	57	0	196.6	52.4
340	69	0	196.6	52.4
545	104	0.20	196.6	52.4
660	114	0.33	196.6	52.4
770	128	0.40	195.6	52.4
880	133	0.57	195.6	52.4
980	137	0.74	195.6	52.4
1,150	143	1.10	195.6	52.4
1,480	153	1.86	195.6	52.4
1,620	155	2.20	195.6	52.4
1,960	163	3.08	195.6	52.4
2,450	170	4.46	195.6	52.4
2,720	174	5.30	195.6	52.4
3,260	182	6.99	195.6	52.4
3,570	186	8.04	195.6	52.4
3,920	189	9.25	195.6	52.4
4,340	193	10.78	195.6	52.4
4,930	198	13.00	195.6	52.4
6,470	211	19.24	195.6	52.4
7,810	219	25.10	197.1	52.4
9,150	225	31.35	197.1	52.4
11,360	236	42.75	197.1	52.4
12,680	243	49.92	197.1	52.4
15,540	255	66.85	197.1	52.4
18,528	268	86.25	197.1	52.4
20,110	274	97.35	197.1	52.4

TABLE A3.3-8: ISOTHERMAL GAS DRIVE CALCULATIONS FOR GRAPHICAL ANALYSIS, RUN NW3

RUN NW3 (11/29/78)

T_{core} = 294°F
p_{avg} = 184 psia

$$\left[\frac{q\mu}{\Delta p}\right]_b = \frac{(K,md)(A,in^2)}{1.607(L,in)} = 3.04\ \frac{(m\ell/hr)cp}{psi}$$

Q_i pV	$\bar{S}_g$ pV	Time Step Average Q_i pV	Time Step Average $\overline{\lambda^{-1}}$ cp
0.0639	0.0639		
		0.0736	0.263
0.0833	0.0833		
		0.101	0.189
0.119	0.119		
		0.139	0.204
0.158	0.158		
		0.175	0.170
0.192	0.192		
		0.284	0.126
0.376	0.289		
		0.418	0.155
0.460	0.317		
		0.494	0.180
0.529	0.355		
		0.573	0.141
0.618	0.369		
		0.660	0.133
0.703	0.380		
		0.790	**0.111**
0.877	0.397		
		1.06	0.104
1.24	0.425		
		1.31	0.103
1.39	0.430		
		1.59	0.0948
1.80	0.453		
		2.11	0.0893
2.42	0.472		
		2.61	0.0810
2.80	0.483		
		3.18	0.0805

Continued

TABLE A3.3-8: CONTINUED

		Time Step Average	
Q_i pV	$\overline{S}_g$ pV	Q_i pV	$\overline{\lambda^{-1}}$ cp
3.56	0.505		
4.03	0.517	3.79	0.0748
4.57	0.525	4.30	0.0739
5.25	0.536	4.91	0.0701
6.23	0.550	5.74	0.0680
8.99	0.586	7.61	0.0632
11.5	0.608	10.3	0.0596
14.2	0.625	12.9	0.0564
19.2	0.655	16.7	0.0506
22.3	0.675	20.7	0.0481
29.7	0.708	26.0	0.0442
38.1	0.744	33.9	0.0403
42.9	0.761	40.5	0.0373

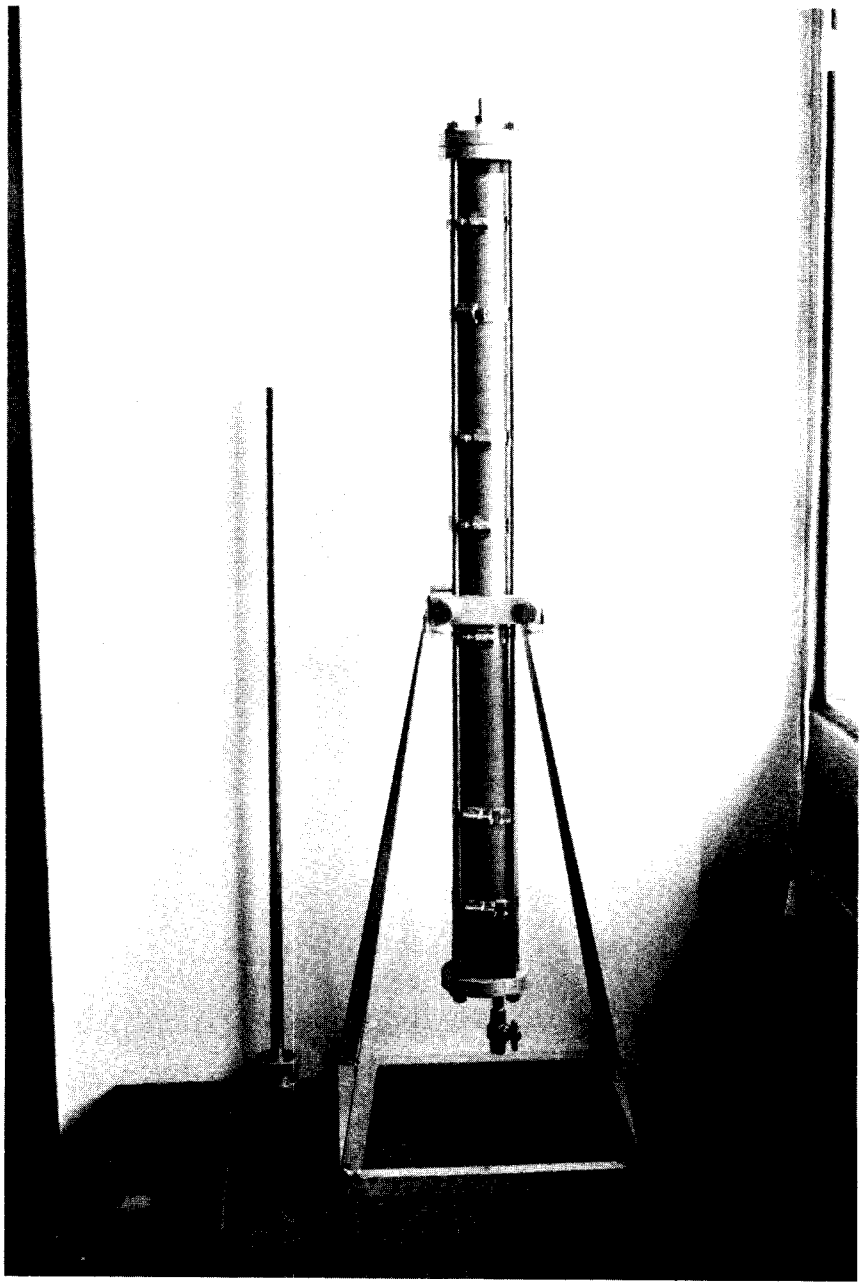

Fig. 4-7: CORE MOLD APPARATUS [DEVELOPED BY ARIHARA (1974) AND CHEN (1975)] USED TO FABRICATE SYNTHETIC CONSOLIDATED CORES

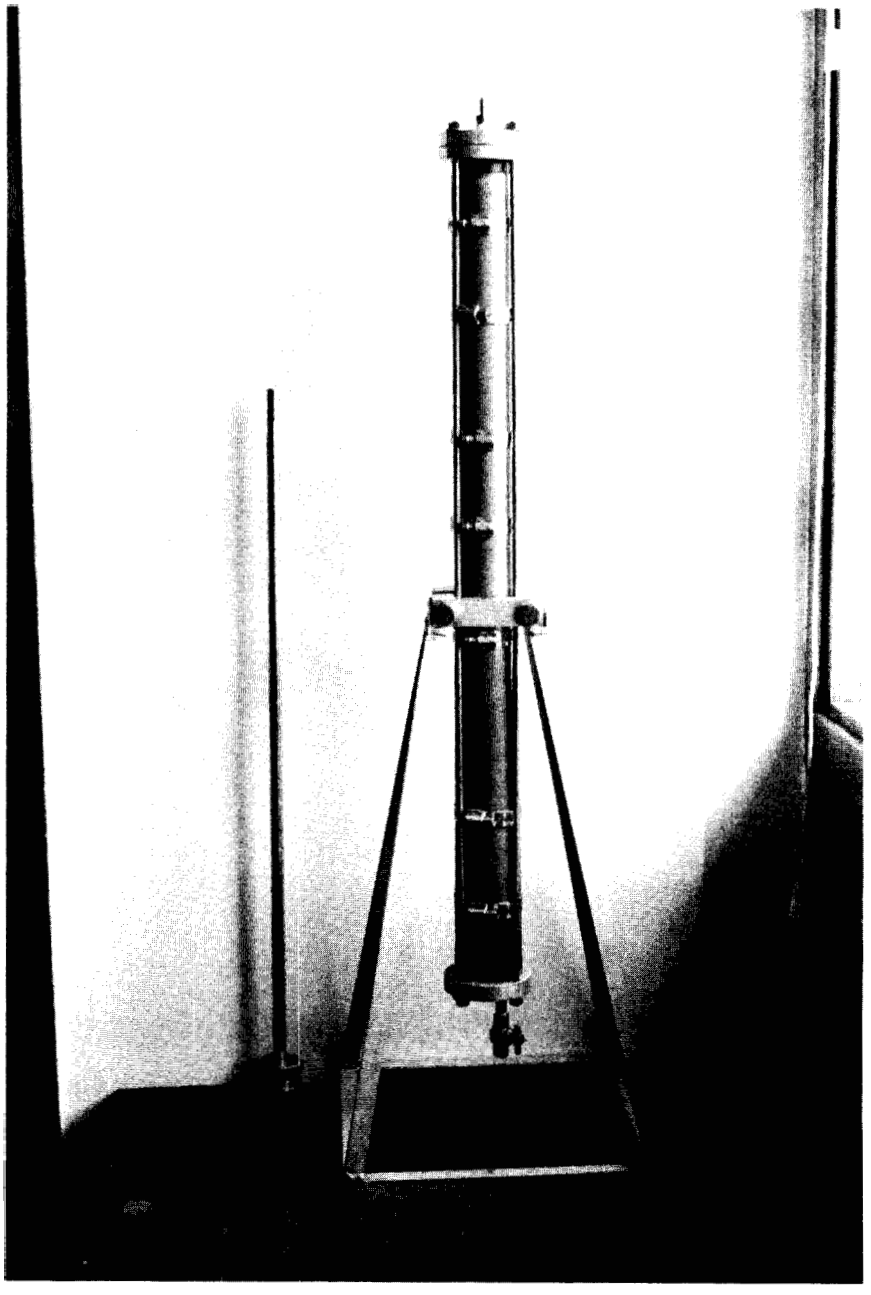

Fig. 4-7: CORE MOLD APPARATUS [DEVELOPED BY ARIHARA (1974) AND CHEN (1975)] USED TO FABRICATE SYNTHETIC CONSOLIDATED CORES

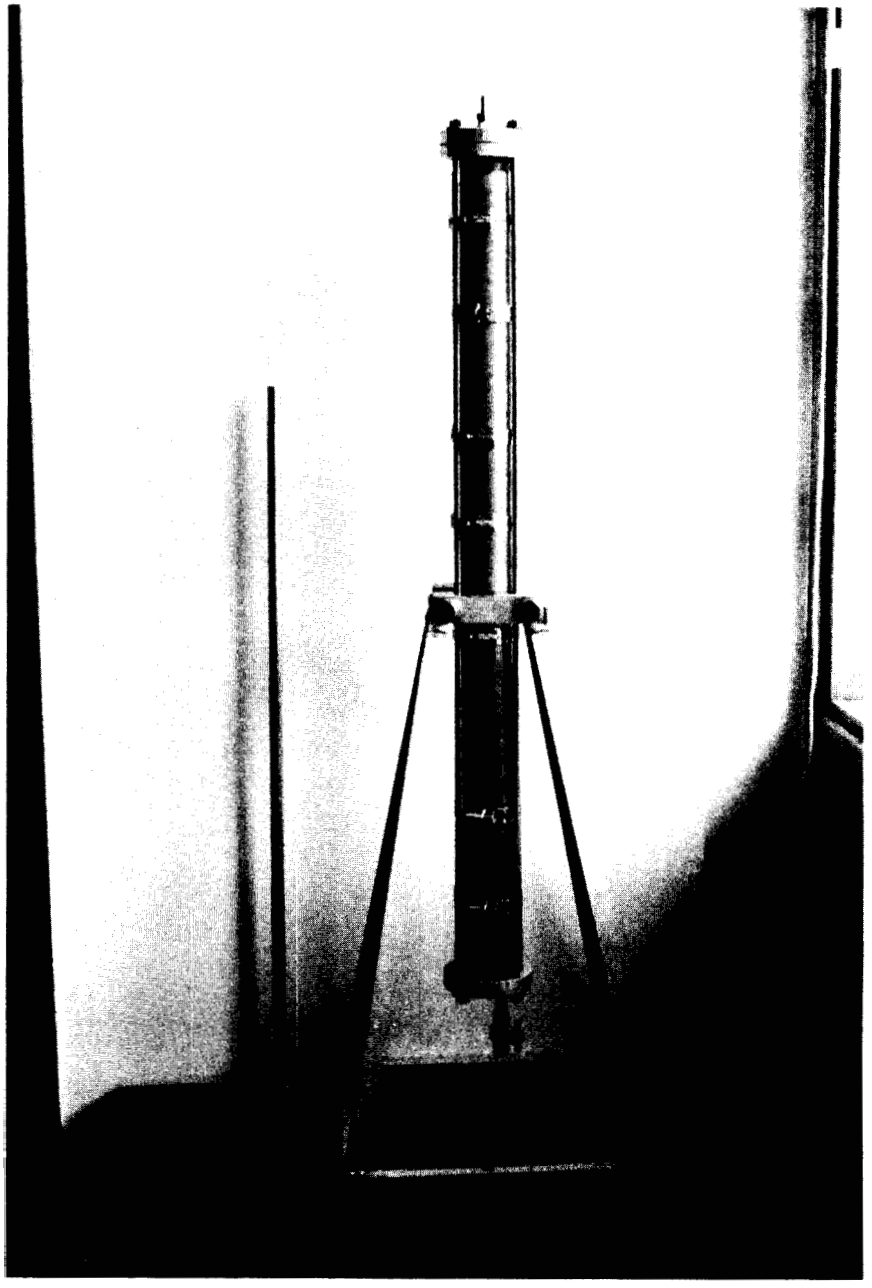

Fig. 4-7: CORE MOLD APPARATUS [DEVELOPED BY ARIHARA (1974) AND CHEN (1975)] USED TO FABRICATE SYNTHETIC CONSOLIDATED CORES

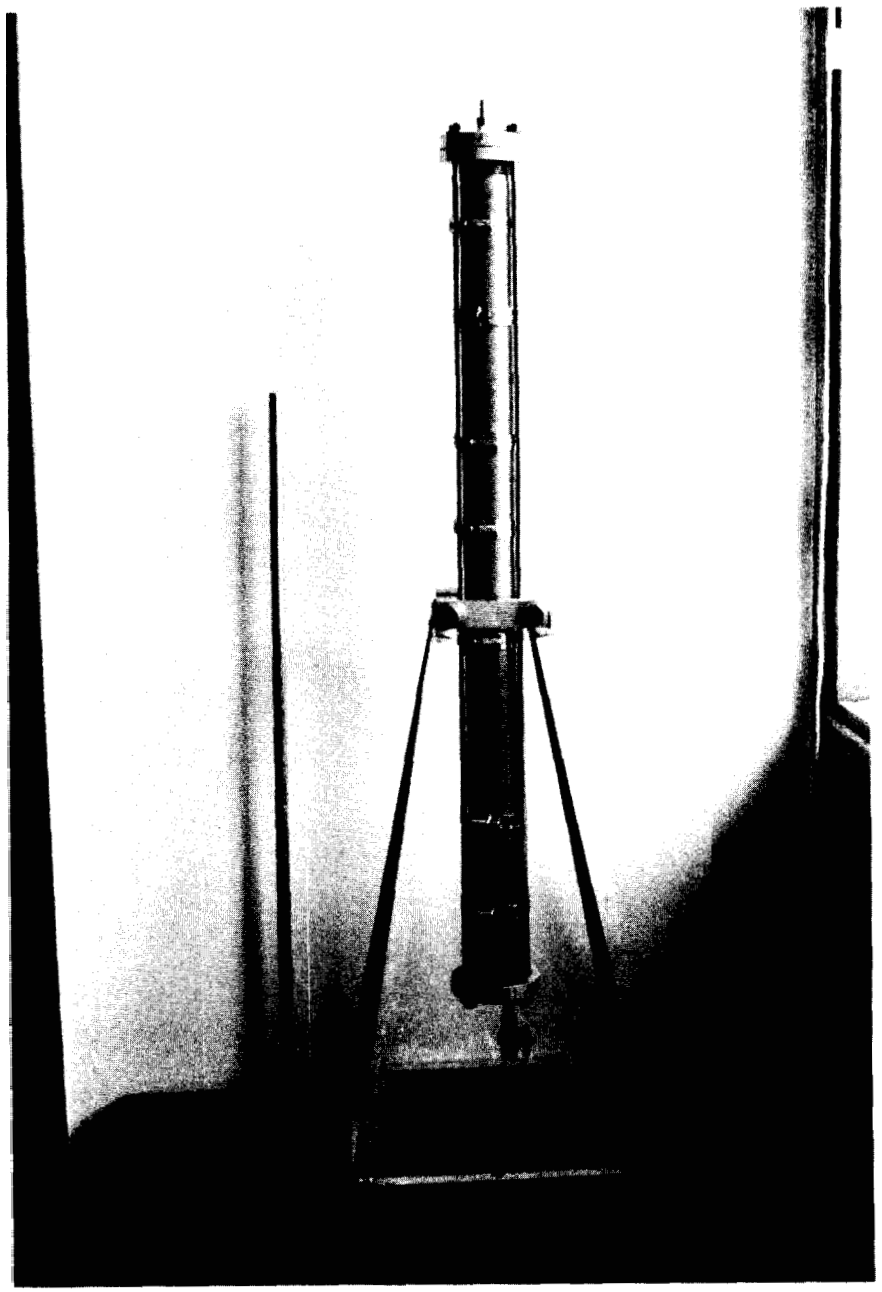

Fig. 4-7: CORE MOLD APPARATUS [DEVELOPED BY ARIHARA (1974) AND CHEN (1975)] USED TO FABRICATE SYNTHETIC CONSOLIDATED CORES

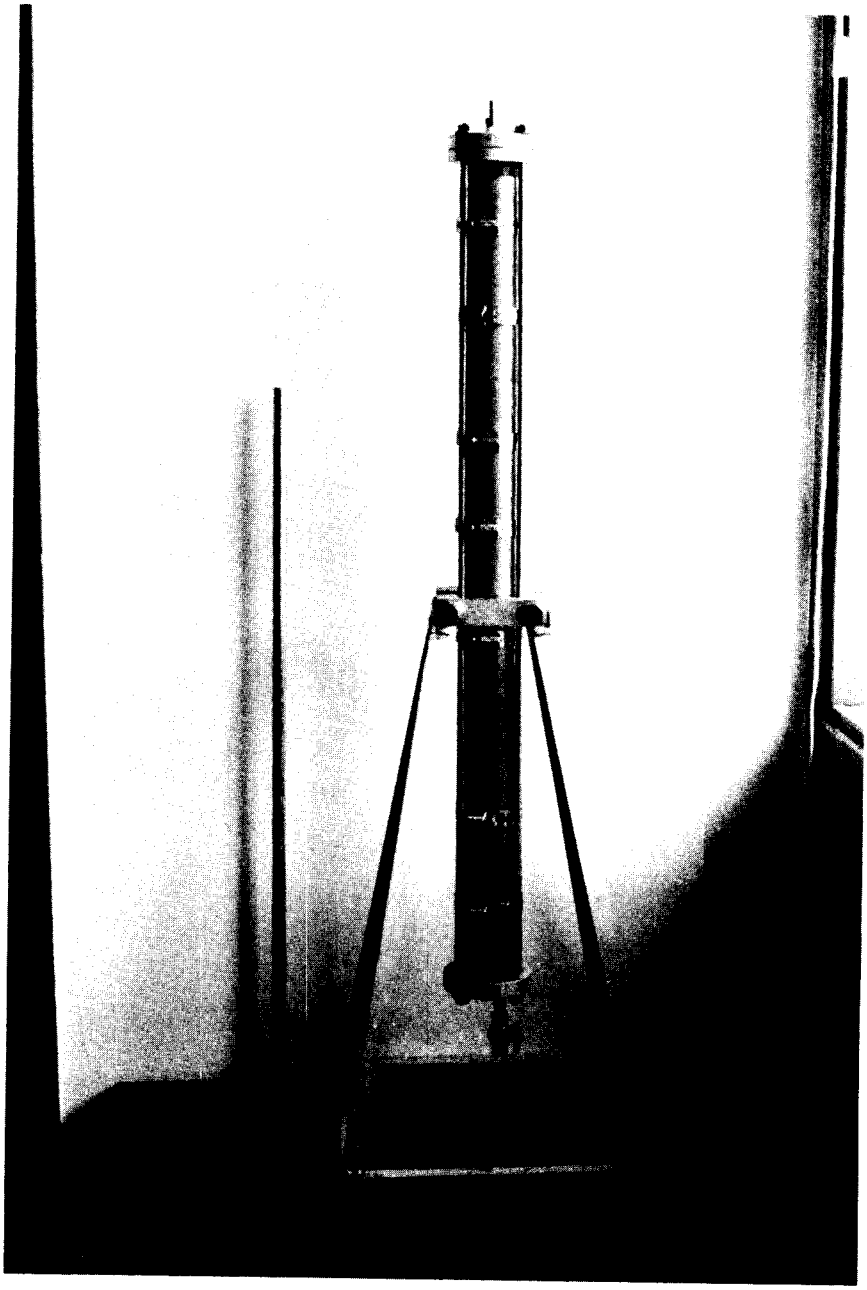

Fig. 4-7: CORE MOLD APPARATUS [DEVELOPED BY ARIHARA (1974) AND CHEN (1975)] USED TO FABRICATE SYNTHETIC CONSOLIDATED CORES

TABLE A3.3-8: CONTINUED

		Time Step Average	
Q_i pV	$\overline{S}_g$ pV	Q_i pV	$\overline{\lambda^{-1}}$ cp
3.56	0.505		
4.03	0.517	3.79	0.0748
4.57	0.525	4.30	0.0739
5.25	0.536	4.91	0.0701
6.23	0.550	5.74	0.0680
8.99	0.586	7.61	0.0632
11.5	0.608	10.3	0.0596
14.2	0.625	12.9	0.0564
19.2	0.655	16.7	0.0506
22.3	0.675	20.7	0.0481
29.7	0.708	26.0	0.0442
38.1	0.744	33.9	0.0403
42.9	0.761	40.5	0.0373

$$u'_H \qquad \frac{}{\left(\frac{k}{\mu}\right)_H \frac{dp}{dx}} \qquad {}_H \Delta p$$

$$\text{when } \left(\frac{k}{\mu}\right)_H = \left(\frac{k}{\mu}\right)_V \text{ and } \frac{dp}{dx} = \frac{\Delta p}{L_H} \tag{2-29}$$

In this case, L_V can be the radius and L_H the length of a horizontal, cylindrical core. The larger t_V/t_H, the less likely gravity segregation will influence the results.

The next section presents important aspects of the heat transfer involved in nonisothermal flow through porous media.

As noted by Chen (1976), early calibration curves for the capacitance probe were found to be nearly independent of temperature.

Because the dielectric constant of water decreases with increasing temperature, the capacitance also decreases and the resonant frequency ($\varepsilon = [2\pi\sqrt{LC}]^{-1}$) increases. The normalized signal, or frequency $(\varepsilon_s - f)/(\varepsilon_s - \varepsilon_w)$, discussed by Chen would therefore be expected to decrease with increasing temperature because $\varepsilon_s > f$.

However, a second temperature effect also exists. At higher temperatures, the brass rod within the probe expands more with temperature increase than does the silver-plated glass tubing. For a parallel plate capacitor, capacitance is indirectly proportional to the distance between the plates. As the gap in the probe capacitor increases with increasing temperature, capacitance is expected to decrease, resonant frequency (or probe signal) increase, and normalized frequency (or normalized probe signal) decrease. Apparently, the parallel plate capacitor model is inadequate because Chen observed a decrease in probe signal with increasing temperature when the probe was immersed in air. Similar tests recently completed have verified this result. For instance, a probe that was partially removed from a hot, steam-saturated core for 3 minutes, provided a signal that was 0.6 mv larger than the signal from the probe when fully inserted into the core. As Chen concluded, the effect of temperature on the probe geometry compensates, in some as-yet-undefined way, for the effect of temperature on the dielectric constant of water.

Although the normalized probe signal appears to be independent of temperature, the use of the calibration curve requires some care. The main use of the probe is in nonisothermal, two-phase flow experiments.

The above results indicate that: (1) if no vaporization occurs, $x_{dry} = 0$ and the results reduce to the usual displacement equations, (2) using the intercept value, the correct f_{w2} and f_{g2} values will be calculated whether or not vaporization occurs ($x_{dry} \geq 0$), and (3) relative permeability will be graphed as a function of incorrect saturations if the intercept value is assumed to be the outlet face saturation, S_{g2}, when vaporization occurs ($x_{dry} > 0$).

Table 6-9 shows that only small gas saturation corrections are required at large injection volumes. In general, the required correction is small except for very large cumulative injection volumes at high temperatures and low pressures. The experiments in this study were terminated before the vaporization of liquid from the core affected the results appreciably.

It is interesting that inlet end water saturation reduction due to vaporization requires a correction in the outlet end water saturation.

The assumption that all water evaporation occurs at the core inlet is not strictly correct because, due to the flowing pressure gradient, some vaporization occurs along the entire length of the core. The region of unit gas saturation, x_{dry} in length, could perhaps be more appropriately considered a region of $(1-S_{wi})$ gas saturation of length $x_{dry}\left[\frac{1}{1-S_{wi}}\right]$, where S_{wi} is the irreducible water saturation. But a similar analysis would again indicate small corrections to the outflow liquid saturation.

Now, all that remains is to correct the relative reciprocal mobility terms, $\overline{\lambda^{-1}}$ and λ_2^{-1}, to consider the inlet region of lowered water saturation. This decreased water saturation should cause an increased

TABLE A3.3-9: ISOTHERMAL GAS DRIVE RELATIVE PERMEABILITY CALCULATIONS, RUN NW3

RUN NW3

T_{core} = 294°F
p_{avg} = 184 psia
y_{H_2O} = 0.333
y_{N_2} = 0.667
$\mu_{steam(g)}$ = 0.0143 cp
μ_{N_2} = 0.0228 cp
μ_g = 0.0206 cp
μ_w = 0.187 cp

Q_1 pV	$\bar{S}_g$ pV	f_{w2} $(\bar{S}_g - S_{g2})/Q_1$	f_{g2} $1-f_{w2}$	S_{g2} pV	$\bar{\lambda}_2^{-1}$ cp	k_{rg} $(f_{g2}\mu_g)/\lambda_2^{-1}$	k_{rw} $(f_{w2}\mu_w)/\lambda_2^{-1}$
0.426	0.316	0.266	0.734	0.203	0.171	0.0876	0.290
0.851	0.397	0.126	0.874	0.290	0.160	0.111	0.147
3.40	0.497	0.0250	0.975	0.412	0.0923	0.216	0.0507
13.6	0.621	0.00683	0.993	0.528	0.0706	0.287	0.0181
39.5	0.749	0.00382	0.996	0.598	0.0546	0.372	0.0131